Technische Universität München
TUM School of Engineering and Design

A novel ring model for tire dynamics and its application to uncertainty quantification

Zhe Liu

Vollständiger Abdruck der von der TUM School of Engineering and Design der Technischen Universität München zur Erlangung des akademischen Grades einer

Doktorin der Ingenieurwissenschaften (Dr.-Ing.)

genehmigten Dissertation.

Vorsitz: Prof. Dr.-Ing. Markus Lienkamp

Prüfer*innen der Dissertation: 1. Prof. Dr.-Ing. Steffen Marburg
2. Prof. Zhichao Hou, Ph.D.

Die Dissertation wurde am 08.11.2022 bei der Technischen Universität München eingereicht und durch die TUM School of Engineering and Design am 11.04.2023 angenommen.

Abstract

The dynamic response of tires directly affects the vibration and dynamics of a vehicle, and in turn, determines the handling stability and ride comfort of a vehicle, and driver perception. Modeling and simulation of tire dynamics typically require a reasonable computational cost while ensuring proper accuracy, which remains a challenging topic in the research field of vehicle dynamics simulation. Especially, when tire uniformity, i.e., the defects originating in the components of tires during manufacturing process, need to be considered in the analysis of transient and steady-state responses, the prediction of the associated dynamic behavior will be affected by these uncertainties. Hence, it becomes a much more complex problem.

For tire modeling, simplifying a tire to a ring-shaped structure is a promising way to balance accuracy and computational costs. Moreover, a ring model has the ability to be combined with other theories, which allows it to be continuously improved and applied to different scenarios. Due to this fact, it poses a new challenge: how to make the developed ring model as complete as possible in characterizing the tire dynamics with reasonable computational efficiency? For example, the model should be able to implement a concise and accurate description of the out-of-plane vibration of the tire, involve the real geometric defects instead of using an oversimplified assumption, and assess the distribution of the responses due to uncertain parameters.

This thesis focuses on the modeling of tire dynamics and vibration, as well as its application to uncertainty quantification of dynamic behavior and uniformity caused by tire defects. Consequently, based on the theory of the tire ring model, a novel theoretical model is presented to describe the in-plane and out-of-plane vibrations and the steady-state response. Then, a novel theoretical model, the coupled rigid-flexible ring model, is presented to analyze the characteristics of the in-plane dynamic responses of tires on uneven road surfaces by simplifying the proposed three-dimensional ring model to a two-dimensional flexible ring. The established new method consists of three primary sub-models: an elastic contact algorithm featured by a flexible ring model, rolling/vibration dynamics represented by a rigid ring model, and an internal-force transmission algorithm linking the rigid and flexible ring models. In this way, the new model has the merits of both high accuracy up to 150Hz and low computing cost. In addition, it is extended to the analysis of the low-speed uniformity of tires with geometric defects and is validated experimentally.

Moreover, the deterministic model has been applied to evaluate the influence of uncertainties in structural and geometric parameters on natural frequencies and dynamic responses under an uncertain excitation. Specifically, the generalized polynomial chaos (gPC) expansion method is combined with the proposed deterministic models to evaluate the influence of uncertainties.

To obtain the unknown coefficients of gPC expansions, a non-intrusive probabilistic collocation method (PCM) is adopted to evaluate the coefficients, and the selection of collocation points is also illustrated. This framework of stochastic analysis is applied to investigate the impacts of elastic, geometric, and structural uncertainties on the natural frequencies and low-speed uniformity of tires. Moreover, the discussions of the distribution of dynamic responses caused by each parameter and different variance levels are given. At last, the validity of the model is demonstrated by comparing it with a large number of measurements.

The major contribution of this thesis is to propose effective and novel algorithms to address these problems from tire dynamics modeling to the stochastic analysis and evaluation of parameter uncertainty. The main contents were published at international conferences or in journals.

Kurzfassung

Das dynamische Verhalten der Reifen eines Fahrzeugs beeinflusst unmittelbar das Schwingungsverhalten sowie die Dynamik eines Fahrzeugs. Dies wirkt sich wiederum auf die Fahrstabilität, den Fahrkomfort und die Wahrnehmung des Fahrers aus. Die Modellierung und Simulation der Reifendynamik erfordert sowohl einen angemessenen Rechenaufwand als auch die Gewährleistung einer ausreichenden Genauigkeit, was nach wie vor eine Herausforderung für die Fahrdynamiksimulation darstellt. Die Vorhersage des dynamischen Verhaltens gestaltet sich wesentlich komplexer, sobald Unsicherheiten im Auslegungsprozess berücksichtigt werden. Bei der Analyse des transienten und stationären Verhaltens von Reifen müssen insbesondere Unsicherheiten bzgl. der Reifengleichförmigkeit berücksichtigt werden. Diese Defekte entstehen v.a. während des Herstellungsprozesses.

Die Analyse der vereinfachten Modellierung eines Reifens als ringförmige Struktur (Ringmodell) stellt einen vielversprechenden Kompromiss zwischen Genauigkeit und Rechenkosten dar. Ein solches Ringmodell kann zudem mit anderen Theorien kombiniert werden, wodurch es kontinuierlich verbessert und auf verschiedene Szenarien angewendet werden kann. Hieraus folgt jedoch eine neue Herausforderung: wie kann das verbesserte Ringmodell die Reifendynamik möglichst vollständig aber mit angemessenem Rechenaufwand beschreiben? Das Modell sollte unter anderem eine prägnante und genaue Beschreibung der Schwingungen des Reifens aus der Rotationsebene heraus zulassen, reale geometrische Defekte anstatt stark vereinfachender Annahmen berücksichtigen und eine Bewertung der unsicherheitsbehafteten Strukturantwort aufgrund der unsicheren Parameter ermöglichen.

Diese Arbeit konzentriert sich sowohl auf die Modellierung der Reifendynamik und -schwingung als auch deren Anwendung zur Unsicherheitsquantifizierung des dynamischen Verhaltens und der durch Reifendefekte entstandenen Gleichförmigkeit. Basierend auf der Ringmodelltheorie von Reifen wird ein neuartiges theoretisches Modell zur Beschreibung der Schwingungen innerhalb und außerhalb der Rotationsebene und des stationären Verhaltens vorgestellt. Durch die Vereinfachung des vorgeschlagenen dreidimensionalen Ringmodells zu einem zweidimensionalen flexiblen Ring wird ein neuartiges theoretisches Modell, das gekoppelte starr-flexible Ringmodell, vorgestellt. Dieses dient der effizienten Analyse des dynamischen Verhaltens von Reifen in der Rotationsebene für den Lastfall einer unebenen Straßenoberfläche. Die vorgeschlagene neue Methode besteht primär aus drei Teilmodellen: einem durch ein flexibles Ringmodell modellierten elastischen Kontaktalgorithmus, einer durch ein starres Ringmodell modellierten Roll-/Schwingungsdynamik, und einem Algorithmus zur internen Kraftübertragung, der das starre und das flexible Ringmodell miteinander verbindet. Auf diese Weise hat die vorgeschlagene Methode sowohl eine hohe Genauigkeit bis zu

150 Hz als auch geringe Rechenkosten. Darüber hinaus wird dieses Modell auf die Analyse der Reifengleichförmigkeit bei niedrigen Geschwindigkeiten mit geometrischen Defekten erweitert und experimentell validiert.

Darüber hinaus wurde dieses deterministische Modell zur Bewertung des Einflusses von strukturellen und geometrischen Parameterunsicherheiten auf die Eigenfrequenzen und das dynamischen Verhalten bei unsicheren Erregungen erweitert. Insbesondere wird die Methode der verallgemeinerten polynomialen Chaoserweiterung (gPC) zur Unsicherheitsquantifizierung mit den vorgeschlagenen deterministischen Modellen kombiniert. Zur Berechnung der unbekannten Koeffizienten der gPC-Erweiterungen wird eine nicht-intrusive, probabilistische Kollokationsmethode (PCM) angewandt, wobei die Selektion der Kollokationspunkte detailliert geschildert wird. Diese stochastische Methodik wird zur Untersuchung der Auswirkungen der elastischen, geometrischen und strukturellen Unsicherheiten auf die Eigenfrequenzen und die Reifengleichförmigkeit bei niedrigen Geschwindigkeiten angewandt. Abschließend wird die Gültigkeit des Modells durch den Vergleich mit einer großen Anzahl von Messungen nachgewiesen.

Der Hauptbeitrag dieser Arbeit liegt in den effektiven und neuartigen Algorithmen zur Problemlösung und Modellierung der Reifendynamik, der stochastischen Analyse und der Bewertung der Parameterunsicherheiten. Die wichtigsten Inhalte wurden auf internationalen Konferenzen oder in Fachzeitschriften veröffentlicht.

Acknowledgment

It seems that only when I started writing these words, I could luxuriate in expressing my heartfelt gratitude without following the rules of "scientific writing". But when my emotion overcomes reason, so many words instantly came to my mind and overwhelmed me, that I do not know where to start.

First of all, I would like to express my deepest and sincerest gratitude to my supervisor, Prof. Dr.-Ing. Steffen Marburg. As “Doktorvater” is the term used for a doctoral supervisor in German, he gave me the maximum degree of patience and freedom to promote me to mature during my doctoral studies. I significantly benefited from his experience in scientific research. His serious and scrupulous work attitude deeply influenced me. It was his concern for me and his respect for my choices that carried me through many challenging moments in my research and in my life. Steffen, ich bin dir zu tiefstem Dank verpflichtet!

I am very thankful to the supervisor of my master’s study, Prof. Yintao Wei. I still cannot imagine that our first meeting eight years ago determined my research path until now. He provided me with academic guidance for my research and the chance to cooperate with the tire industry. Because of our in-depth scientific discussions, I was able to successfully complete my current project. I am so lucky to have met such a good supervisor.

I am greatly grateful to Prof. Zhichao Hou. On the one hand for taking over the second examiner, and on the other hand for his refreshing insights on this dissertation given in a responsible manner.

I would like to express my special gratitude to Prof. Dr.-Ing. Markus Lienkamp for organizing the defense as the chairman.

I am grateful to the engineers of Shandong Linglong Tire Co., Ltd. They are Zhixing Cai, Bo Lu, Shibin Zhu, and Lijie Zhang. Also, the engineer of Double Coin Tire Company, Jianming Zhao. They are the ones who provided me with a large amount of measurement data, which allowed me to validate my work. They gave me an opportunity to continuously iterate and optimize the algorithms and models.

Ich möchte meinen Kollegen danken. Sie sind Martin Eser, Christopher Jelich, Karl-Alexander Hoppe, Johannes Schmid, Jonas Schmid, Felix Kronowetter, Dr.-Ing. Suhaib Koji Baydoun, Sourav Chandra und Dr.-Ing. Marcus Mäder (in keiner bestimmten Reihenfolge). Sie gaben mir das Gefühl, mit der Gemeinschaft in diesem fremden Land verbunden zu sein. Die COVID-Epidemie war für alle anstrengend, deshalb war ich dankbar für unser jedes Mittagessen und unsere jede Kaffeepause, die wir in dieser Zeit im Konferenzraum verbrachten. Mein besonderer Dank gilt meinen drei

süßen Kolleginnen, Simone Preuss, Bettina Chocholaty und Magdalena Scholz. Ich werde weder vergessen, wie wir uns unterhielten und unser Leben miteinander teilten, noch wie sie mir halfen und mich unterstützten, als ich eine Arbeitsstelle suchte. Sie haben mir unzählige Male Freude, Trost und Unterstützung gegeben. Ein ganz besonderer Dank geht an Martin für seine schöne geduldige Unterstützung bei der Verbesserung der deutschen Kurzfassung. Ich wünsche ihnen alles Gute für ihre Zukunft.

I definitely owe my family and friends appreciation, who gave me their pure and unreserved love. I would like to thank my best friend, Yunya Liu, for her support and companionship. No matter how long we have not seen, we know well to each other as if we were family. I would like to express thanks to my fiancé, Yongpeng Zhao. He is the gentlest, warmest, and most perfect soul mate I could ever imagine. He was there by my side in many of my emotional breakdowns and in my innermost depression. I would like to give my greatest thanks to my parents, for their unconditional love for me. They have given me the largest allowance of freedom and tolerance. But also, it was them who stood behind me, gave me trust and love, and allowed me to move forward without any fear. I am so proud that I am their daughter.

Finally, I hope to express my gratitude and memory to my grandfather, who led the ignorant little girl into the door of mathematics and engineering. At this moment, I wish he could know this good news in another world.

List of Acronyms

FEM	Finite Element Method
NVH	Noise, Vibration, and Harshness
REF	Ring on Elastic Foundation
DOF	Degree of Freedom
GA	Genetic Algorithm
PDF	Probability Density Function
LHS	Latin Hypercube Sampling
MCS	Monte Carlo Simulation
PCE	Polynomial Chaos Expansion
gPC	Generalized Polynomial Chaos
PCM	Probabilistic Collocation Method
RFV	Radial Force Variation
RFV1H	First Harmonic of Radial Force Variation
RRo	Radial Run-outs
LSU	Low-speed Uniformity
HSU	High-speed Uniformity

List of Figures

List of Tables

Contents

Chapter 1

Introduction

1.1 Motivation & background

Tires play an essential role in the noise, vibration, and harshness (NVH) analysis of vehicles. With the emphasis on driving speed, safety, comfort, and handling performance, there is a great need for a refined analysis of tire dynamics [1]. Tire models not only have an essential influence on the whole vehicle dynamics analysis but also play an important role in the simulation of automotive electronic control systems such as anti-lock braking systems (ABS) and electronic stability programs (ESP).

This section illustrates the motivation for this study in terms of tire modeling and the uncertainty quantification of tire dynamics and uniformity. Specifically, the motivations are explained in two aspects.

1.1.1 Why tire modeling

Tires are the only component of the vehicle that contact with the road surface. It makes that the dynamic response and the transmission characteristics of tires are of crucial importance to the dynamic behavior and the NVH performance of the whole vehicle. Establishing an accurate and fast algorithm for tire dynamics can not only provide a theoretical basis for the traditional NVH assessment but also promote the electrification and intelligent control of the tire and chassis development. In the research field of intelligent tires, which has been widely discussed in recent years, a dynamic model of the tire can be used to construct relationships between the sensor measurement signals and the tire structural parameters. An accurate and high-precision tire model can use to achieve a quantitative description of the relationship between the measurement signals and tire responses.

However, due to the complex structure and material composition of a tire, there is still a lack of analytical explanations for the mechanism of its deformation and transmission characteristics. Since the 1960s, scholars have been concentrating on the modeling of tire dynamics and the analysis of tire vibration characteristics. The automotive industry also began to recognize that the vibration characteristics of tires, such as modal data and natural frequencies, are very closely related to the handling performance, NVH, and riding comfort of the whole vehicle. Considering the complexity of the structure and the material distribution, large deformations, high-speed rolling conditions, etc., it has become a key point in vehicle dynamics research to establish a tire model that ensures computational efficiency without losing accuracy.

1.1.2 Why uncertainty quantification of tire dynamics and uniformity

From the viewpoint of engineering design, a tire is ideally expected to be a perfect circle, and its interior stiffness, dimensions, mass distribution, and other characteristics are uniform around the circumference of the structure. However, the typical tire construction and manufacturing processes make the mass production of such ideal tires to be unrealistic. The complicated production process introduces uncertain variables into the structure of tires. Defects in geometry and material distribution, such as radial geometric deflection, unbalanced mass distribution, non-uniform sidewall stiffness, and bias in steel belts, inevitably occur during the tire manufacturing process [2]. These imperfections, i.e., the tire non-uniformities [3], lead to variations in the forces acting on the spindle even in the case of steady-state rolling at a constant speed. The additional excitation will be transmitted to the occupants through the different vehicle subsystems and body structures. This part of the irregular vibration caused by the tire non-uniformities sometimes is the underlying cause of steering wheel shake, vehicle body vibration, and the generation of interior noise. These abnormal dynamic responses often affect the riding comfort and driving quality of the vehicle and also cause disturbance to the occupants [4]. The analysis of characteristics of the dynamic response due to tire imperfections is referred to as tire uniformity analysis.

However, in the case of tires, the internal defects or non-uniformities are uncertain, i.e., each parameter or variable has a corresponding distribution instead of a deterministic value. Consequently, it is necessary to evaluate the uniformity of tires by consideration of the theory of stochastic analysis. In this context, an accurate assessment of the stochastic dynamic behavior is of practical importance in manufacturing. The quantitative results can be used for quality optimization of the mass production of tires. More importantly, the uncertainty quantification of vehicle dynamics has constantly received attention in the past years [5, 6]. Whereas, the implementation of tire uncertainty quantification will provide a theoretical basis for the analysis of the whole vehicle system. Hence, it

is of theoretical significance and extensive application to discuss the effects resulting from the tire uniformity parameters and their uncertainty quantification.

1.2 Literature review

1.2.1 Modeling of tire vibration and dynamics

Since the 1960s, a large number of researchers discussed the research of tire models, the knowledge of tire dynamics is thoroughly developed. A variety of tire dynamics models were developed, which can be divided into the following categories, including simple physical models [7–10], empirical and semi-empirical models [11, 12], and advanced models based on ring or shell theory [13–19].

The modeling approach of converting a pneumatic radial tire into a ring-shape structure has a long history and occupies a significant place in the analysis of vehicle dynamics. Several important tire dynamic models, such as SWIFT [13–15] and FTire [16, 17], which are integrated into vehicle multi-body dynamics software have been developed based on the ring model theory. A ring model of a tire can provide a concise approach to realize the analysis of tire vibrations and dynamics. This simplified method of transforming a pneumatic tire into a ring on an elastic foundation can date back to the 1960s [20, 21]. The earliest research started with the analysis of the free vibration of tires. Since the 1960s, Clark [20], Tielking [21], and Böhm [22] have analyzed the dynamic properties of tires using equivalent rings. There were many studies on the theoretical model based on a ring on an elastic foundation (REF) which has been already widely used. Böhm [22] simplified a tire into an equivalent structure with a set of radial springs (sidewall) and a circular ring (belt). The two-dimensional (2D) deformation and free vibration characteristics were calculated, and then the standing wave phenomenon due to the angular velocity was studied. On this basis, Pacejka [12] considered the tangential and radial stiffness of the sidewall for the first time and took into account the inflation effect of the tire. The results of the free vibration and the standing wave analysis were compared with the simulation of Böhm [22]. In the 1980s, Kung *et al.* [23, 24] presented a simplified method to analyze the free vibration based on an REF model and compared it with a finite element (FE) model.

Furthermore, academics have paid attention to the forced responses of tire vibration. However, establishing a proper tire-road contact model is a challenging task for such studies. Potts *et al.* [25] first expanded the forces in the contact area by Fourier series under the assumption of a thin-wall flexible ring. The contact pressure was assumed to be a parabolic distribution which achieved an approximation of the contact area. Soedel and Prasad [26] subsequently focused on the effect of the

tire-road contact model on the dynamic responses. They conducted an experimental modal analysis of a rim-tire assembly without contact with the ground to identify the parameters in the forced dynamic equations. The natural frequencies and mode shapes of the loaded tire were obtained afterward. Takayama [27] proposed a 5-degrees-of-freedom (DOF) mass-spring system, in which the belt and tread were considered as a rigid ring, and the sidewall and the contact effect were treated as linear springs. The radial and tangential axial forces generated when the tire was rolling over a cleat were calculated. Huang *et al.* [28] further developed the model proposed in the literature [26] by simplifying the road contact kinematically using radial and tangential displacement constraints. The equations for in-plane vibration were derived using the equivalent ring structure, and the forced solution was obtained.

Considering the deformation modes of tires, the previous works of the ring model have summarized the vibrations of tires in the condition of in-plane vibration [21, 28–31] and out-of-plane vibration [32, 33]. The in-plane vibration includes circumferential and radial bending. The breathing mode which has a close relationship with noise generation can be evaluated. The out-of-plane vibration includes transverse bending and out-of-plane torsion. It is closely related to the cornering performance and transmission characteristics of tires. As the theoretical basis, there has already been a great deal of research on rings [34–37], however, the literature dealing with the out-of-plane vibration is still very scanty. The study of the out-of-plane vibration of the ring can be traced back to the research proposed by Bert and Chen [38]. They first studied the out-of-plane vibration of a rotating ring at high speed. They adopted an assumption by considering the effect of a centrifugal force as an algebraic term. In the 1980s, Irie *et al.*[39, 40] presented a series of studies on the in-plane and out-of-plane vibrations and steady-state responses of rings. Using the Hamilton principle, Bickford and Maganty [41] derived the out-of-plane natural frequency of thick circular rings. He has also given the relative contributions caused by the centrifugal and Coriolis acceleration to the natural frequency. Eley *et al.*[42] introduced the effects of anisotropy into the vibration of a circular ring made from crystalline silicon. The calculation of the out-of-plane flexural modes has been shown. Recently, Doria *et al.*[43] studied modal analysis tests of out-of-plane modes of some motorcycle tires using impulsive analysis. The lateral natural frequencies and damping were identified. For predicting the lateral vibration of tires, Matsubara *et al.*[33] set out an approach to analyzing the vibration of an elastic ring by using the Lagrangian method with the assumption of in-extensional deformation. Liu *et al.*[32] derived an analytical solution for both, the in-plane and out-of-plane natural frequencies based on a ring model. The accuracy has been validated by a practical radial tire. However, the analysis of the out-of-plane vibration is still incomplete, and many factors such as rotation, damping, and shear deformation, were not fully considered in the published works.

In the 1990s, the rigid ring model was developed rapidly and comprehensively. Gong [44] performed a detailed analysis and calculation of the in-plane vibration using the flexible ring model. The rim was introduced into the tire model for the consideration of the dynamic response of the coupled structure. In addition, the transfer characteristics under different vertical loads were discussed. Zegelaar [14] promoted the application of the rigid ring and flexible ring models, respectively. In particular, the rigid ring model was employed to calculate the dynamic response of the vehicle during braking and the flexible ring model was applied for modal analysis. Moreover, the study of ring models was expanded to the investigation of structural uniformity analysis. Allaei *et al.* [45] performed the estimation of natural frequencies and modes of non-axisymmetric tires and those tires with concentrated mass or non-uniform stiffness. Stutts *et al.* [46] addressed the issue of the dynamic responses of the vertical and longitudinal axial forces due to the unbalanced mass based on the rigid ring model. Later, they [47] went further to analyze the effect of the non-uniform stiffness distribution of the sidewall.

Research into the ring model, the theory of which is still being improved, has not stopped in recent years. Wei *et al.* [48] extended a 2D flexible ring model to the computation of the general forced response by adopting the theory of Meirovitch modal analysis and first-order matrix perturbation. The impacts of damping and rolling speed on the responses were discussed. Popov and Geng [49] studied the damping characteristics of tires. Non-proportional viscous damping and complex modal analysis techniques were adopted to analyze the measurement, identification, and modeling of damping of heavy vehicle load tires. Wei *et al.* [29] derived the general forced solutions for undamped vibration based on a 2D REF model by adopting the modal expansion technique and the Meirovitch modal analysis method. The closed-form transient response under the stationary concentrated load was obtained. Kozhevnikov [50] discussed the free and forced vibration of tires and then estimated a tire rolling at a constant speed. Graham [51] concluded that the vibration of the tire sidewall plays an important role in the tire vibration responses, and therefore, the undamped vibration of the sidewall, which was equivalent to a fiber-reinforced membrane structure in the shape of a circle connected to a fixed rim. The belt was also studied. The ring models are not only used for theoretical analysis, but Lee *et al.* [52] also considered wave propagation in a rotating tire and applied a flexible ring model to the improvement the complex modal testing technique of tires. Vu *et al.* [53] established a nonlinear flexible ring model based on the Timoshenko beam theory, which also reflected the large deformation due to the rotation effect. But they did not extend their model to the application of the contact algorithm. Matsubara *et al.* [33] developed a flexible ring model to analyze the three-dimensional vibration of tires. However, the bending strain and stress of the ring were not completely described in their model. It resulted in the problem that higher-order bending modes cannot be predicted. Later, Liu *et al.* [32] proposed a three-dimensional

ring model of the tire without the limitation of the inextensible assumption. The out-of-plane bending and torsional deformation modes were shown first. The established model was applied to a truck tire, and compared with the FE model and the experimental results. Yu *et al.* [31] developed new displacement function for tire radial and lateral vibrations. They also studied the high-order bending vibration of tires. Yang *et al.* [54] introduced the concept of modal assurance criterion into the tire ring model and predicted the in-plane vibration of the non-rotating and rotating tires. Liu *et al.* [55] investigated the planar vibration of large-section-ratio radial tires used for heavy-load vehicles using theoretical modeling and experimental modal analysis. The deformation of the belt structure was combined into the flexible ring model by the multi-stiffness function of the sidewall. Subsequently, they [56] developed a 2D analytical model for the sidewall stiffness of heavy-load tires based on a flexible ring model coupled with a nonlinear 2D sidewall element. The tire-road contact model and the static stiffness properties were investigated. In the research field of intelligent tires, the flexible ring model [57–60] was also applied to represent the tire characteristics and further estimate the dimensionless numbers of the tire model using intelligent tire sensor signals.

In the literature review, it is obvious that although research on the tire modeling of vibration and dynamics has been conducted for many years, scholars and engineers are still continuously exploring the application of tire models in different areas. From the traditional prediction of the natural frequencies to the application in the field of intelligent tires over the past few years, it is always essential to carry out the modeling of tire dynamic responses. The theory of tire modeling has also evolved from its initial application under only a single simulation condition to a well-integrated algorithm that combines with the whole vehicle dynamics model, and it can meet the challenges of different complex application scenarios.

1.2.2 Tire uniformity

The production quantities of tires are often enormous. Defects in geometry and material distribution, such as radial geometric deflection, unbalanced mass distribution, non-uniform sidewall stiffness, and bias in steel belts, will inevitably occur during the tire manufacturing process [2]. These imperfections, i.e., the uniformity parameters of tires, can lead to variations in the forces acting on the spindle even in the case of steady-state rolling at a constant speed. However, few studies were conducted to implement a stochastic analysis of the distribution of the corresponding response while considering the uncertainty in the uniformity parameters resulting from tire production. Most tire companies aspire to be able to foresee the uniformity of each production batch of tires before they are ready for the market, thereby enabling improvements to the process flow. Traditionally, the measurement of tire non-uniformity forces and moments has been realized in one of two ways,

including on low-speed factory machines or on high-speed research machines [3]. The factory-type machine is operated at 60 or 120rpm. Generally, the radial, tangential, and lateral force variations (RFV, TFV, and LFV) are measured at the axle of the drum, and sometimes also the geometric deflection, e.g., radial run-outs (RRo), can be collected. The rolling speed of the drum is very low so that the resonance of the tire is not aroused during the measurement, and the result obtained is the force variations occurring at the contact area. This type of low-speed uniformity machine is also known in the industry as the “LSU machine". During the typical tire manufacturing process, factory floor measurements of tire uniformity are performed on LSU machines, which are used to monitor the quality of the tire production process and may guide or incorporate corrective measures such as grinding to improve the balance and uniformity of a tire [61–63]. Only those tires that qualify for the uniformity criteria are shipped to customers (or sent to the next step of the tire evaluation process) [62]. In contrast, another type of test machine is the high-speed uniformity (HSU) machine. They can operate at realistic driving speeds and undertake experimental measurements including the effects of tire resonances. Unfortunately, it is difficult and costly to directly measure high-speed force variations on tires. They are consequently often found in research laboratories rather than in manufacturing plants [61–63]. Due to the complexity of the measurements, the tested tires are normally not available for sale due to wear and tear.

It is because tire uniformity is unavoidable in production but crucial in practical applications, how to improve structural imperfections has always been a core issue for tire manufacturers. Since the 1970s some tire companies have been carrying out relevant research. Dunlop Ltd. [64] initiated a study on the variation of the first harmonic of tires under different speeds and presented the phase and amplitude relationship between the longitudinal and radial force variations with speed. In 1989, Firestone Tire and Rubber Co. [65] described the probabilistic distributions of the first harmonic and the uniformity parameters by normal probability density functions and later predicted the mean value and the standard deviation of the offset. After a company merger with Firestone Tire Company, Bridgestone Inc. [66] further investigated the relationship between the angular velocity deviation and the longitudinal force on account of the uniformity parameters, which would be a valuable supplement to the existing measurements of estimating tire non-uniformities. Hyundai Motor Co. [67] also studied the shimmy phenomena in the steering system induced by the unbalanced mass distribution and the structural imperfections of tires. Goodyear Tire & Rubber Co. [68] conducted measurements on a high-speed uniformity machine to obtain the first harmonic of the tangential force variation (TFV) and the radial force variation (RFV). In turn, the influence of tire uniformity on the vibration modes and the quality of riding comfort has been discussed. Shanghai Tyre & Rubber (Group) Co. [69] adopted finite element analysis to estimate the RFV by considering the geometric and material defects. In 2005, Hankook Tire Co. [70–72] presented a series of studies

on the transmission mechanism of the steering wheel vibration and the dynamic force variations resulting from tire imperfections. The influence of tire resonances on the force amplitudes has been demonstrated and compared with the measured data and the simulation results of the FTire model. As mentioned above, most of the studies from the tire companies are based on statistical analysis with a large number of test samples and measurements which is not only costly but also difficult to achieve from uniformity tests to tire structure optimization, production process control, and dynamic performance improvement.

Considering the cost of experiments, the necessity of virtual development from component design to complete vehicle analysis has been felt over the years. As a consequence, for assessing the effects of tire uniformity, many researchers attempted to develop theoretical physical models to properly understand the complex deformation and its interaction with the pavement. Based on substantial experimental data, Gillespie [73] originally simplified a tire as a spring-mass system to explain the influence of non-uniformities in tire-wheel assemblies on the driving quality of heavy trucks. However, this physical model cannot provide a good description of the practical non-uniformities on account of the oversimplified assumptions adopted for the tire structure. Under the assumption of a rigid ring, Stutts *et al.* [46, 47] explained the phenomenon that the longitudinal force grows faster than the vertical force on the spindle as the speed increases. The mechanism by which the additional concentrated stiffness of the sidewall leads to the generation of RFVs has been further discussed. Dorfi [72] also used a rigid ring model to investigate the impacts of the non-uniform mass distribution, the eccentricity of the belt, and the thickness variation of the tread rubber. The analytical results were subsequently compared with the simulation results estimated by a widely-used and promising physical tire model, i.e. FTire. On the foundation of the work by Stutts *et al.*, Dillinger *et al.* [74] combined a viscoelastic model of the sidewall [75] and a longitudinal force relaxation model [13] to calculate the tangential and radial forces by involving mass, stiffness, and geometric defects in the analysis. Pottinger [76] summarized the impact of the mass imbalance on the transfer properties of a tire-wheel assembly and proposed a method for improving the response of the spindle forces due to the installed assembly uniformity.

While uniformity is an essential factor in the structural design of tires and the dynamic analysis of the whole vehicle, most of the published studies concentrated on the rigid ring models on account of the complexity of the tire structure and materials. Because the limitations of deformation are assumed by the rigid rings, only over-simplified models can be applied to characterize the uniformity parameters, such as using an overall eccentricity or a simple function to represent the geometric offsets. The inherent restrictions of these assumptions make the existing physical models only capable of a simple qualitative discussion of various types of uniformity parameters or statistical

analysis from large amounts of experimental data.

1.2.3 Uncertainty quantification of tires

Due to the defects of tires being uncertain parameters or variables, it is unavoidable to evaluate the uniformity of tires by consideration of the theory of stochastic analysis. Since the 1970s, some tire companies were carried out relevant research [64, 66, 68, 69]. Most uniformity analysis techniques rely on deterministic models [70–72, 77], and these models generally assume that the structural and uniformity parameters of the tire are deterministic. However, the parameters of tires and their response are uncertain under conditions of mass production.

Some researchers attempted to investigate the probabilistic characteristics of tire uniformity through statistical methods from a large number of measurements. In 1989, Schuring [65] described the probabilistic distributions of the first harmonic and the uniformity parameters by normal probability density functions and later predicted the mean value and the standard deviation of the offset. Gillespie [73] originally simplified a tire as a spring-mass system to explain the influence of non-uniformities in tire-wheel assemblies on the driving quality of heavy trucks. Pottinger [76] summarized the impact of the mass imbalance on the transfer properties of a tire-wheel assembly and proposed a method for improving the response of the spindle forces due to the installed assembly uniformity. However, the inherent restrictions of these theories make the existing models only capable of a simple qualitative discussion of various types of uniformity parameters or statistical analysis from large amounts of experimental data. Nowadays, little research has explicitly addressed the challenge of the stochastic modeling of the dynamic responses and meanwhile takes into account the parametric uncertainties of tire uniformity.

Fortunately, the theory of stochastic structural dynamics analysis has been continuously developed, which provides a possible approach for the stochastic prediction of tire uniformity. Several approaches [78, 79], e.g., probabilistic methods, interval mathematics, fuzzy set theory, etc., are utilized to evaluate the output responses influenced by uncertainties. The study of stochastic structural dynamics had initiated in the mid-1960s, mostly based on the Monte Carlo simulation (MCS) [80–82], the perturbation method [83, 84] and the spectral methods [85]. The traditional method for assessing the probability density function (PDF) of the output responses of a system is the Monte Carlo method [86, 87], which has the most extensive application in stochastic dynamics. The method generally requires a large amount of test data to obtain reasonable results, which leads to high computational costs. Although structured sampling techniques such as Latin hypercube sampling (LHS) can be deployed to improve computational efficiency [88], the gains for complex

problems may not be significant [89–91]. Due to the slow convergence and the high computational costs, MCS is often used to verify the feasibility of other methods for stochastic dynamics analysis.

The spectral methods, in contrast, based on the homogeneous chaos theory [92] are used to overcome the drawbacks of the MCS. More recently proposed stochastic analysis approaches comprise generalized polynomial chaos (gPC) methods based on Wiener's polynomial chaos expansion (PCE) [85, 93] and stochastic response surface methods [94, 95]. They are considered to have better performance in terms of computational efficiency. In the field of structural dynamics, Ghanem and Spanos[85] developed the spectral stochastic finite element method where Hermite polynomial chaos is used to represent uncertain parameters. On this foundation, the generalized polynomial chaos expansion method was developed by Xiu and Karniadakis [93, 96]. The basic idea is to approximately represent uncertain parameters by using the sum of the orthogonal polynomials of independent random variables. Once the function expansion of the random variable is performed, the statistical quantities of the random variable are easily obtained. Because this method avoids the extensive sampling in MCSs and in turn improves computational efficiency, it has been widely used and improved in recent years.

The gPC expansion method was successfully applied to a variety of dynamics analysis [97–101], including the vehicle dynamics prediction [102–107]. In the research field of structural vibration and dynamics, Sinou and Jacquelin [100] presented a procedure to determine the steady-state response of a rotor system with uncertain stiffness, in which a polynomial chaos expansion is performed to evaluate the mean and standard deviation of the response. The influences of uncertain material parameters, random fiber orientation, and damping parameters on the vibration of fiber-reinforced composite structures were investigated by Sepahvand *et al.*[108, 109]. Wu *et al.*[101] assumed the random geometry and material properties in the structure as random variables and expanded them with polynomial chaos. Afterward, they solved the dynamic equations of a rigid-flexible multibody system and achieved the prediction of the uncertain dynamic response. Polynomial chaos expansions were also implemented in the uncertainty quantification issues of vibration and dynamic response of civil structures and gained good performance [110]. Wan *et al.*[98] improved the existing gPC theory and proposed an arbitrary polynomial chaos expansion (aPCE) -based method to perform uncertainty quantification of the natural frequencies of a truss structure, and applied it to a long-span steel arch bridge. Yuan *et al.*[111] employed the PCE to realize the sensitivity analysis of turbine blades equipped with dampers and to quantify the impact of contact parameters on the variation in the nonlinear dynamic response.

In the analysis of vehicle dynamics,Wu *et al.*[106] analyzed the deformation of the suspension to realize the roll plan model by combining the Chebyshev inclusion function theory with the

gPC theory. Kwon *et al.*[107] proposed a model of military vehicles to evaluate driving comfort and firing stability by combining the polynomial chaos theory with the analysis of variance. Wang *et al.*[112] used the polynomial chaos expansion to improve the vertical vibration issues of a modified electric vehicle. The reliability-based design optimization with uncertain excitation parameters was conducted on a half-car model with nonlinear suspension parameters. Polynomial chaos theory has also been utilized for parameter estimation of vehicle models. Ma *et al.*[113] predicted the inertia parameters of a vehicle. Shimp [114] developed an adaptive polynomial chaos approach to estimate sprung mass parameters of a simplified quarter-vehicle model. Price [115] performed the computation of the lateral and longitudinal center of gravity of a vehicle based on measurement data as well as assessed the uncertainties by conducting a PCE model.

In addition, the gPC expansion method has also been promoted in acoustics analysis. Sepahvand *et al.*[116] proposed a framework for analyzing the uncertainty in natural frequencies and radiated sound power of a composite plate. Yin *et al.*[117] combined the evidence theory and the arbitrary polynomial chaos expansion to establish a hybrid stochastic analysis method, which was applied to address the structural acoustics problem with uncertain parameters. A recent study by Kuhn *et al.*[118] was carried out to investigate the effects of uncertain parameters on the aeroacoustic feedback of cavity flows.

Although many researchers applied the gPC expansion method to analyze the stochastic dynamic response of various structures, it has not been introduced to the prediction of the production quality of tires. In this thesis, these methods based on the polynomial chaos theory are illustrated and their applicability to the analysis of low-speed uniformity of tires is investigated.

1.3 Objectives & scope

While several types of tire models were developed to evaluate the vibrations and dynamic responses, few theoretical models are available for the modeling and the uncertainty quantification of the three-dimensional (3D) vibration, transmission properties, and uniformity of tires. In addition, these two aspects of tires, which are the deterministic modeling and the stochastic analysis, are treated as isolated problems in most of the literature, and their underlying relations have not been discussed in detail. From the literature review, it is evident that there is a substantial need for modeling the vibration and the dynamic responses of tires. The new proposed model should be able to be expanded to as many scenarios as possible with a wide range of applications.

Therefore, the objective of this work is to develop a new theoretical model to evaluate the characteristics of the 3D vibration and the dynamic responses of tires, which is also used to analyze

the transmission mechanism of the radial force at the spindle caused by the structural defects in tires and road unevenness. Furthermore, this developed model should be suitable to estimate the stochastic distributions of the vibration and the dynamic responses of tires caused by structural and geometric uncertainties.

To achieve this objective, a 3D flexible ring model is first developed to describe the in-plane and out-of-plane vibrations, and the steady-state response of tires. A coupled rigid-flexible ring model is presented based on the tire ring model. Its emphasis is placed on the description of the dynamic properties and the practical application to the simulation of tire and vehicle dynamics. The contact algorithm is established by the simplification of the 2D flexible ring, which provides a more accurate pressure distribution on the tire-road contact patch and the length of the footprint under different vertical loads than the traditional rigid ring model. In contrast, the rigid ring model has a better performance on computational efficiency. Combining the advantages of these two types of ring models, it is expected that the dynamic responses can be solved efficiently and accurately. Further, the identification of model parameters and the optimization approach based on the test data are given, which should be easy to implement and robust. Ultimately, the generalizability of the developed model in different simulation conditions is verified by the analysis of the low-speed uniformity of tires with geometric defects and the corresponding measurements.

And then, the gPC theory and the probabilistic collocation method are introduced, in order to evaluate the influence of uncertainties in the structural parameters on the natural frequencies, steady-state responses, and uniformity. The uncertain parameters and the desired responses are approximated by using the truncated gPC expansions having a random orthogonal basis. The probabilistic collocation method is employed in order to obtain the unknown coefficients of the expansions. It is applied to investigate the influences of elastic and structural uncertainties on the natural frequencies of the tire.

The last objective of this research is to implement a stochastic prediction of low-speed uniformity, which is applied for the optimization of manufacturing processes and quality evaluation before the mass production and marketing process. The results of the stochastic analysis of the low-speed uniformity of tires are first given. For the prediction of the production quality for a massive number of tires, the influences of the uncertainties in different factors on the radial force variations and their harmonics are thoroughly discussed, such as the radial run-out and vertical test load. However, the computational cost is often a critical factor in whether this kind of stochastic analysis can be implemented and in its algorithm performance. Hence, the computational efficiencies of Monte Carlo simulations (MCSs) and different probabilistic collocation methods are compared. Finally, a large amount of measured data need to be adopted to demonstrate that the proposed technique can

be employed to achieve an effective prediction for the low-speed uniformity of the mass of tires.

1.4 Outline of the thesis

The topic of this thesis mainly consists of two parts, the modeling of tire dynamics and its extension in uncertainty quantification. The outline of this study is shown in Fig. 1.1. The problems of tire dynamics and uniformity analysis are first introduced and the deterministic models based on the simplification of a tire to a ring structure are derived. The proposed deterministic models include the 3D flexible ring model and the coupled rigid-flexible ring model, which are subsequently applied to analyze the vibration, steady-state response, dynamics, and uniformity simulation. Afterward, these tire models are extended to the stochastic analysis by combining them with the theory of generalized polynomial chaos expansion. The impacts of the uncertain structural, geometric, and material parameters of tires are discussed to predict the probabilistic distributions of the natural frequencies, steady-state responses, and the responses in low-speed uniformity analysis. The accuracy of the models and the algorithms are validated by a number of measurements. The main research framework of this thesis is shown in Fig. 1.2.

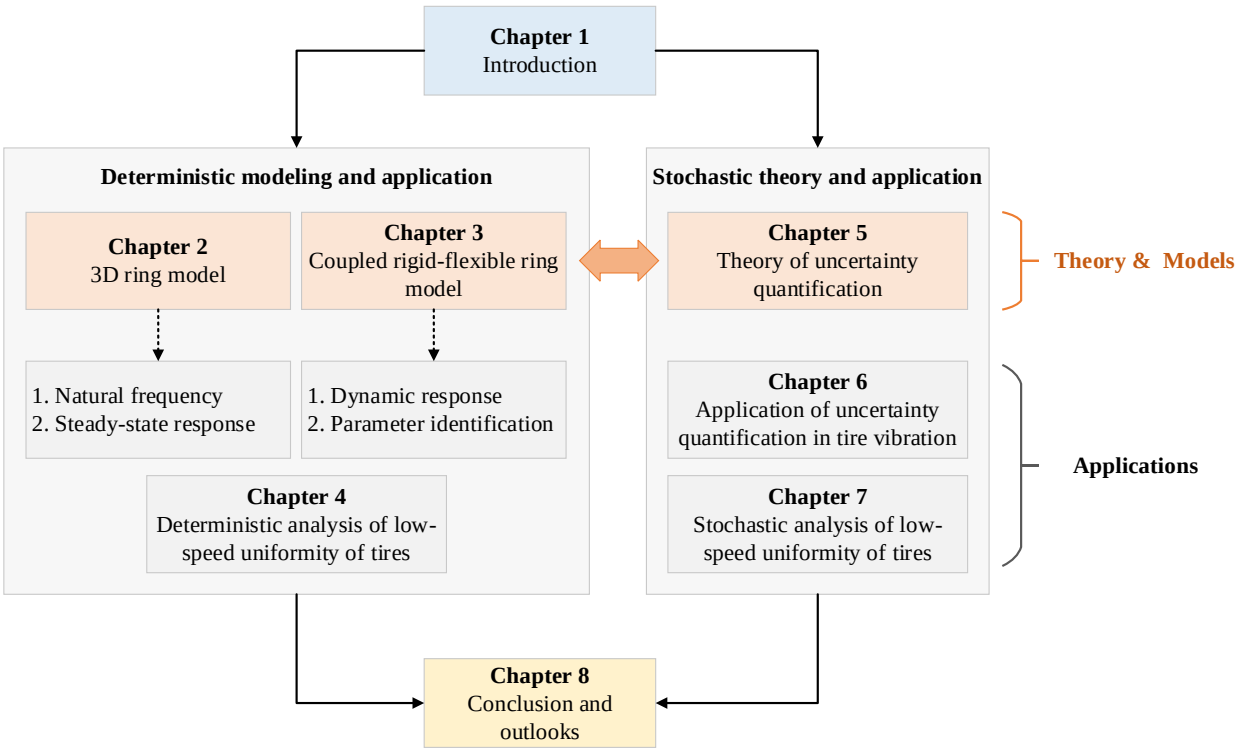

Figure 1.1: Thesis structure.

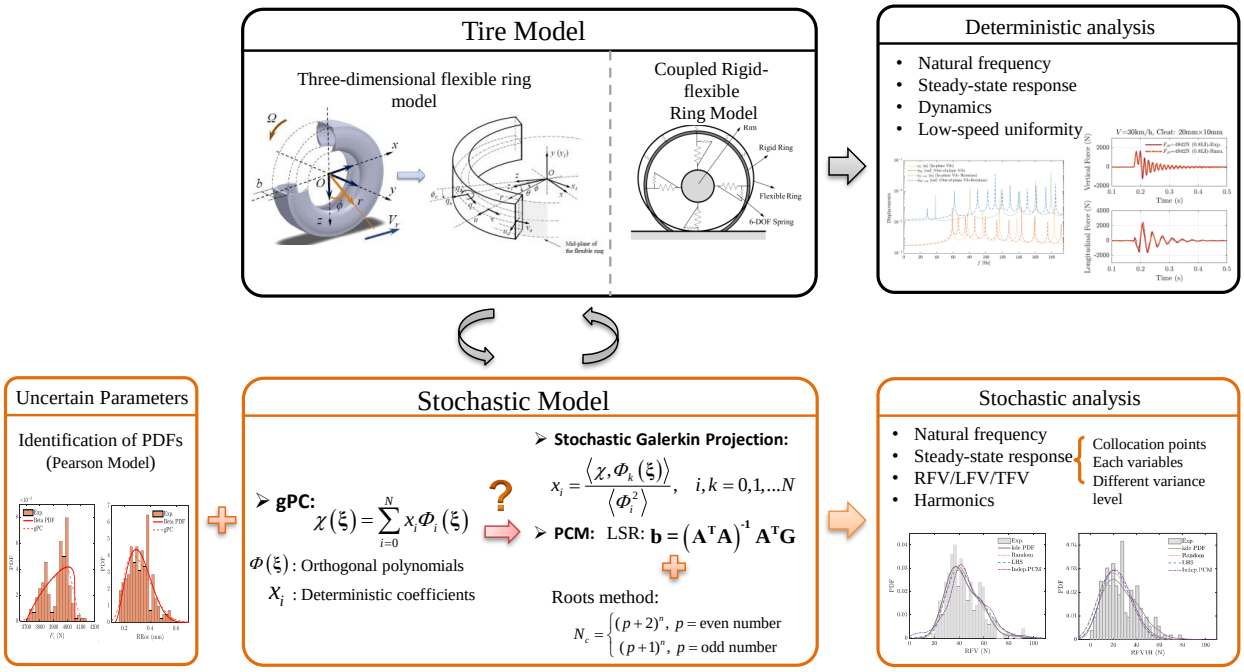

Figure 1.2: The main research framework of this thesis.

This thesis is organized as follows.

- In Chapter 2, a 3D flexible ring model of tires is developed. According to the simplification of tire ring models, a practical tire is equivalent to a 3D deformable circular ring supported on an elastic foundation. A novel theoretical ring-based model is established to describe the in-plane and out-of-plane vibrations and the steady-state response of tires. The Hamilton principle is adopted to derive the equations of motion. A simplified scale, the equivalent radiated sound power is utilized to describe the overall steady deformation characteristics of the tire in this chapter. Afterward, the accuracy of this developed model for the deterministic prediction of the natural frequencies and the steady-state response of a tire is validated.

- In Chapter 3, the three-dimensional ring model is simplified into a two-dimensional model to estimate the in-plane dynamics of the tire. Herein, a coupled rigid-flexible ring model is presented to evaluate the characteristics of the dynamic responses of tires, which is also used to analyze the transmission mechanism of the radial force at the spindle due to road unevenness and structural defects in tires. A contact algorithm based on the 2D flexible ring provides a pressure distribution on the tire-road contact patch and the length of the footprint under different vertical loads. The dynamic responses are then represented by combining the rigid ring model with the flexible ring model. Further, the identification of model parameters based on the test data is given. The accuracy of the contact algorithm and the transient

responses are validated against experimental radial stiffness and over-cleat tests, respectively.

- In Chapter 4, the analysis of the low-speed uniformity of tires with geometric defects is performed by the established model. Moreover, the optimization approach of the model parameters by using a genetic algorithm is given. By comparing with measurements, it indicates that the proposed coupled rigid-flexible ring model yields a reasonable prediction of the low-speed uniformity analysis and offers many application scenarios and extension possibilities.
- In Chapter 5, to evaluate the uncertainties in the structure, geometry, and material distribution of tires, the theory of generalized polynomial chaos expansion is introduced in this work. The probabilistic collocation method (PCM) is employed in order to obtain the unknown coefficients of the expansions. Subsequently, three different methods of the selection of the collocation points are discussed. Based on the concept of linear independence of vectors, the number of selected collocation points is effectively reduced. This yields an efficient simulation for the stochastic dynamic analysis of tires.
- In Chapter 6, considering the uncertain parameters induced by the manufacturing process of tires, the 3D ring model developed in Chapter 2 is combined with the gPC expansion method to estimate the impacts of parameter uncertainties on the natural frequencies and the steady-state response. It is first applied to investigate the influences of elastic and structural uncertainties on the natural frequencies of the tire. Secondly, the rest of this chapter describes the distributions of the sound power owing to the forced vibrations under the uncertainty in the external force terms. The numerical results are in good agreement with the MCSs.
- Furthermore, in Chapter 7, this study implemented a stochastic prediction of low-speed uniformity of tires, which is applied for the optimization of manufacturing processes and quality evaluation before the mass production and the marketing process. The stochastic analysis of the tire low-speed uniformity is given. The influence of the uncertainties in geometric defects on the RFV and its first harmonic (RFV1H) is thoroughly discussed. The computational efficiencies of the MCS, probabilistic collocation method, and 200 sets of measurement data are compared. The results are then shown for the individual effects of each parameter. Finally, the distributions of the responses under different variances of the uncertain inputs are given. Through the validation by using extensive experimental data, it is evident that the proposed technique can be employed to achieve an effective prediction for the low-speed uniformity of the mass of tires.
- Finally, the most essential conclusions of this thesis are given in Chapter 8. The discussion of the current work and the possible improvements of the model are stated here. In addition,

some recommendations for further research are listed as well.

Chapter 2

Three-dimensional Ring Model of Tires

This chapter is to present a novel theoretical three-dimensional (3D) ring model to describe the in-plane and out-of-plane vibrations, natural frequencies, and the steady-state response of tires. In order to obtain the analytical solution of the natural frequencies and steady-state response, the Hamilton principle is adopted to derive the governing equations. The results are compared with the solution given in the previous literature. In the sound radiation analysis, the three-dimensional vibration under a set of harmonic unit forces and moments is considered to be the source of noise generation. Here, a simplified scale, the equivalent radiated sound power, is adopted to describe the overall steady deformation characteristics of the tire.

2.1 Three-dimensional ring model

Dynamic characteristics of tires affect the whole vehicle's performance. Considering the complex structure and excitation, it is essential to establish a proper model for dynamic analysis. Herein, a three-dimensional ring model is established to describe the dynamic response and properties. The steel belt is treated as an elastic ring. It is assumed as an Euler-Bernoulli beam that can bend in two directions, i.e., in-plane and out-of-plane. The sidewall is equivalent to an elastic foundation with damping, and the rim is rigid. Fig. 2.1 shows the schematic of a three-dimensional ring model, a ring with a rectangular cross-section on an elastic foundation rotating at a constant speed. The elastic properties of the foundation are modeled by a set of distributed springs in radial, circumferential, and axial directions (k_u, k_v, k_w), respectively. Damping existing in the foundation can be described by introducing the coefficients (c_u, c_v, c_w) into this model.

In-plane vibration and out-of-plane vibration of the elastic ring are considered in this chapter.

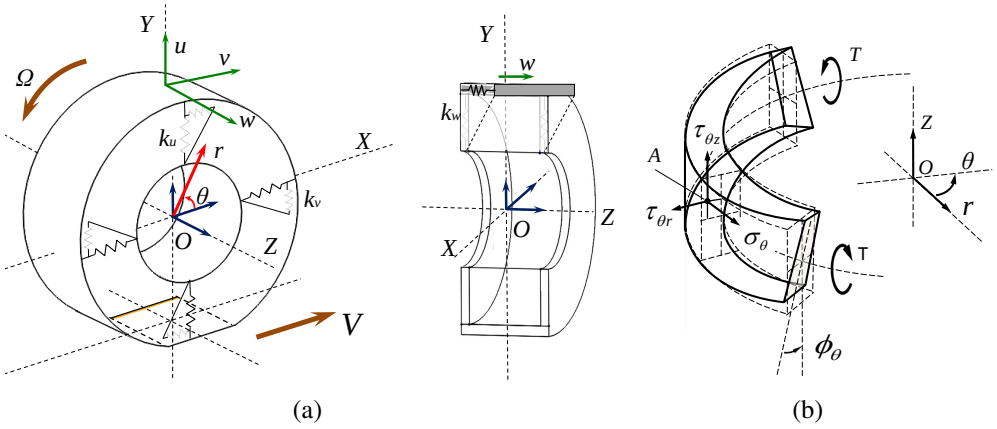

Figure 2.1: Coordinate systems and deformation of a ring on an elastic foundation. (a) Radial, circumferential and axial displacements and (b) torsional angle of the ring.

The in-plane vibration includes circumferential and radial bending, and the out-of-plane vibration includes transverse bending and torsion. In this research, the radial, circumferential, and axial displacements and the torsional angle of the ring are considered to describe the three-dimensional vibration. In particular, in order to obtain the breathing mode (0^{th}-order radial mode) of the ring, the in-extensibility assumption, which restricts the circumference of the middle line is constant during the deformation, is relaxed here.

2.2 Equations of in-plane and out-of-plane motions

Considering the condition of a ring at a constant rotational speed, rotating and non-rotating coordinations are defined. The origins of these two coordinate systems are at the center of the ring. The location of any point on the ring can be described by cylindrical coordinates in the non-rotating coordinate system (r, ϕ, Z), or in the rotating coordinate system (r, θ, Z). It can also be expressed in the Cartesian coordinate system (X, Y, Z). The X-axis is positive in the direction of the forward velocity, and the Y-axis is positive in the upward direction. The Z-axis forms the right-handed coordinate with the other two axes. As shown in Fig. 2.1, the angular coordinate originates from the horizontal direction, i.e., the X-axis, through the ring center, and is taken positive in the counter-clockwise direction.

In this chapter, it is assumed that the equivalent ring is fixed in space but can rotate at a constant speed Ω. Meanwhile, the road surface constantly moves backward. The radial, circumferential, and axial displacements (u_a, v_a, w_a), which can be expressed by the mid-plane displacement (u, v, w),

and the torsional angle ϕ_θ, are applied to describe the motion of the ring. The torsional angle ϕ_θ is the out-of-plane rotational angle around the θ-axis. The displacements of any point on the ring are given as

$$u_a = u + \phi_\theta z_{\text{op}}, \tag{2.1}$$

$$v_a = v - (R-r)\frac{v-u'}{R} - \frac{w'}{R} z_{\text{op}}, \tag{2.2}$$

$$w_a = w + \phi_\theta (R-r), \tag{2.3}$$

where R represents the mean radius, and z_{op} is the Z-axis coordinate. Here the prime designates differentiation with respect to θ. Based on the expressions of the in-plane and out-of-plane displacements, the flexural strain and stress of the ring are written as

$$\varepsilon_\theta = \frac{v'+u}{R} + \frac{1}{2}\left(\frac{v'+u}{R}\right)^2 + \frac{1}{2}\left(\frac{v-u'}{R}\right)^2 - \frac{(R-r)}{R^2}\left(v'-u''\right) - \frac{w''}{R^2} z_{op} + \frac{\phi_\theta}{R} z_{op}, \tag{2.4}$$

$$\sigma_\theta = E\varepsilon_\theta, \tag{2.5}$$

where E represents the elastic modulus of the ring. According to the geometrical assumption, the shear strain and shear stress are obtained as

$$\varepsilon_{r\theta} = \left(\frac{\phi'_\theta}{R} + \frac{w'}{R^2}\right) z_{op}, \tag{2.6}$$

$$\varepsilon_{\theta z} = \left(\frac{\phi'}{R} + \frac{w'}{R^2}\right)(R-r), \tag{2.7}$$

$$\sigma_{r\theta} = G\varepsilon_{r\theta}, \tag{2.8}$$

$$\sigma_{\theta z} = G\varepsilon_{\theta z}, \tag{2.9}$$

where G represents the shear modulus of the ring. Considering the initial stress and the non-linear bending strain [32], the Hamilton principle is used to derive the equations of motion, i.e.,

$$\delta \int_{t_1}^{t_2} (U - T - W)\,\mathrm{d}t = 0, \tag{2.10}$$

where U represents the potential energy, T is the kinetic energy, and W shows the external force energy (including the internal pressure). With the uniform pressure acting on the inner wall of the ring, the initial stress σ_θ^0 is given as

$$\sigma_\theta^0 A = \frac{1}{2}\int_0^\pi \left(\rho A \Omega^2 R + p_0 b\right)\sin\theta R \mathrm{d}\theta = p_0 b R + \rho A R^2 \Omega^2, \tag{2.11}$$

where A is the area of the ring section, ρ denotes the density, Ω means the rotation speed, b represents the effective width, and p_0 is the internal pressure. All energy terms are expressed as

$$U = \frac{b}{2}\int_0^{2\pi}\int_{R-\frac{h}{2}}^{R+\frac{h}{2}} \left(\sigma_\theta\varepsilon_\theta + \sigma_{r\theta}\varepsilon_{r\theta} + \sigma_{\theta z}\varepsilon_{\theta z} + 2\sigma_\theta^0\varepsilon_\theta\right) r\mathrm{d}r\mathrm{d}\theta + \frac{1}{2}\int_0^{2\pi}\left[k_w w^2 + k_v v^2 + k_u u^2 + k_u\left(\phi_\theta\frac{b_{op}}{2}\right)^2\right] R\mathrm{d}\theta, \tag{2.12}$$

$$T = \int_0^{2\pi}\iint_A \frac{\rho}{2}\left\{(\dot{u}_a - v_a\Omega)^2 + \left[\dot{v}_a + (r+u_a)\,\Omega\right]^2 + \dot{w}_a^2\right\} r\mathrm{d}A\mathrm{d}\theta, \tag{2.13}$$

$$W = bp_0R\int_0^{2\pi}\left[u + \frac{1}{2R}\left(v^2 - vu' + v'u + u^2\right)\right]\mathrm{d}\theta + \int_0^{2\pi}\left[q_u u + q_v v + q_w w + q_{Mx}\phi_\theta + q_\beta\frac{v-u'}{R} + q_{Mz}\left(-\frac{w'}{R}\right)\right] R\mathrm{d}\theta, \tag{2.14}$$

in which h is the effective thickness of the ring. The definitions of the variables are given in Sections 2.1 and 2.2. As a matter of fact, damping exists in the tread and the sidewall of tires. It is essential to explain some aspects of tire dynamic properties. Only considering the damping in the sidewall, the dissipation energy term D is given as

$$D = \frac{1}{2}\int_0^{2\pi}\left[c_u\dot{u}^2 + c_v\dot{v}^2 + c_w\dot{w}^2 + c_u\left(\dot{\phi}_\theta\frac{b_{op}}{2}\right)^2\right] R\mathrm{d}\theta. \tag{2.15}$$

When the external forces (q_u, q_v, q_w) and moments (q_β, q_{Mx}, q_{Mz}) act on the middle-line of the ring, both the internal pressure and the external loads will contribute to the overall displacement. The equations of in-plane and out-of-plane motions are represented as follows

$$\frac{EA}{R^2}\left(u+v'\right) + \frac{EI_z}{R^4}\left(u^{(4)} - v'''\right) + \frac{\sigma_\theta^0 A}{R^2}\left(u + 2v' - u''\right) + \rho A\left(\ddot{u} - 2\Omega\dot{v} - \Omega^2 u\right) - \frac{bp_0}{R}\left(u+v'\right) + k_u u + c_u\dot{u} = q_u + \frac{1}{R}q'_\beta, \tag{2.16}$$

$$-\frac{EA}{R^2}\left(u'+v''\right) + \frac{EI_z}{R^4}\left(u''' - v''\right) + \frac{\sigma_\theta^0 A}{R^2}\left(v - 2u' - v''\right) + \rho A\left(\ddot{v} + 2\Omega\dot{u} - \Omega^2 v\right) + \frac{bp_0}{R}\left(u' - v\right) + k_v v + c_v\dot{v} = q_v + \frac{1}{R}q_\beta, \tag{2.17}$$

in which σ_θ^0 denotes the initial stress, A represents the area of the ring section, ρ is the density, b is the effective width, and p_0 is the internal pressure on the inner surface. The in-plane bending and the membrane stiffnesses of the ring are given as EI_z and EA, respectively. Similarly, the

out-of-plane equations are given as

$$\frac{EI_r}{R^3}\left(\frac{w^{(4)}}{R}-\phi_\theta''\right)-\frac{GI_\rho}{R^3}\left(\frac{w''}{R}+\phi_\theta''\right)+\rho A\ddot{w} \\ -\frac{\rho I_z}{R}\ddot{\phi}_\theta+\Omega\frac{\rho I_r}{R}\dot{\phi}_\theta'+k_w w+c_w\dot{w}=q_w+\frac{1}{R}q_{Mz}', \tag{2.18}$$

$$\frac{EI_r}{R^2}\left(\phi_\theta-\frac{w''}{R}\right)-\frac{GI_\rho}{R^2}\left(\phi_\theta''+\frac{w''}{R}\right)+\rho I_\rho\ddot{\phi}_\theta \\ -\frac{\rho I_z}{R}\ddot{w}+\Omega\frac{\rho I_r}{R}\dot{w}'+k_u\frac{b_{\text{op}}^2}{4}\phi_\theta+c_u\frac{b_{\text{op}}^2}{4}\dot{\phi}_\theta=q_{Mx}, \tag{2.19}$$

where b_{op} denotes the nominal width of the ring, EI_r represents the out-of-plane bending stiffness, GI_p is the torsional stiffness and ρI_p means the torsional inertia. It can be found that the in-plane and out-of-plane equations are decoupled. Therefore, Eqs. (2.18-2.19) can be solved independently. When the in-plane governing Eqs. (2.16-2.17) are simplified by the in-extensibility assumption, i.e., $u=-v'$, the same form as given in [44] can be obtained.

2.3 Natural frequencies and modes

With the rotating speed Ω and all external forces being set to zero, one can obtain the analytical solution for the natural frequencies by assuming the wave function of the free vibration mode in the sinusoidal series, which has been stated in the author's previous work [32]. Since the relevant theory of this part has been illustrated in detail, the author would not repeat the derivation here. For a better understanding of the overall organization of this thesis, the expressions for the solution of the natural frequencies are listed here for the readers' reference only.

By substituting the wave function in the sinusoidal series of the free vibration mode into Eqs. (2.16-2.17), the following the coefficient determinant of the characteristic equation is obtained,

$$\begin{vmatrix} \frac{EA}{R^2}+\frac{EI}{R^4}n^4+\frac{p_0 b}{R}n^2+k_u-\rho A\omega^2 & -\frac{EA}{R^2}n-\frac{EI}{R^4}n^3-\frac{p_0 b}{R}n \\ -\frac{EA}{R^2}n-\frac{EI}{R^4}n^3-\frac{p_0 b}{R}n & \frac{EA}{R^2}n^2+\frac{EI}{R^4}n^2+\frac{p_0 b}{R}n^2+k_v-\rho A\omega^2 \end{vmatrix}=0, \tag{2.20}$$

where n is the mode number. Expanding the coefficients in the expression results in the following

equation,

$$\begin{aligned}
&\left(\rho A\omega^2\right)^2 - \rho A\omega^2\left[\frac{EI_z}{R^4}n^2\left(1+n^2\right)+2p_0b\frac{n^2}{R}+\frac{EA}{R^2}\left(1+n^2\right)+k_v+k_u\right]\\
&+\frac{p_0bEI_z}{R^5}\left(n^6-n^4\right)+\frac{p_0bEA}{R^3}\left(n^4-n^2\right)+\frac{EI_zEA}{R^6}\left(n^6-2n^4+n^2\right)+\frac{k_vEI_z}{R^4}n^4\\
&+\frac{k_uEI_z}{R^4}n^2+\frac{k_uEA}{R^2}n^2+\frac{k_vp_0b}{R}n^2+\frac{k_up_0b}{R}n^2+\frac{{p_0}^2b^2}{R^2}\left(n^4-n^2\right)+\frac{k_vEA}{R^2}+k_uk_v=0.
\end{aligned} \tag{2.21}$$

Solving Eq. (2.21) yields the analytical expression of the natural frequency related to the in-plane vibration,

$$\rho A\omega^2 = \frac{B_1 \pm \sqrt{{B_1}^2-4C_1}}{2}, \tag{2.22}$$

in which the coefficients are given as,

$$\begin{aligned}
B_1 &= \frac{EI_z}{R^4}n^2\left(1+n^2\right)+\frac{2bp_0}{R}n^2+\frac{EA}{R^2}\left(1+n^2\right)+k_v+k_u,\\
C_1 &= \frac{bp_0EI_z}{R^5}\left(n^6-n^4\right)+\frac{bp_0EA}{R^3}\left(n^4-n^2\right)+\frac{EI_zEA}{R^6}\left(n^6-2n^4+n^2\right)\\
&\quad+\frac{k_vEI_z}{R^4}n^4+\frac{k_uEI_z}{R^4}n^2+\frac{k_uEA}{R^2}n^2+\frac{k_vbp_0}{R}n^2+\frac{k_ubp_0}{R}n^2\\
&\quad+\frac{b^2{p_0}^2}{R^2}\left(n^4-n^2\right)+\frac{k_vEA}{R^2}+k_uk_v.
\end{aligned} \tag{2.23}$$

Considering a special condition, i.e., $n=0$, and substituting it into Eq. (2.22), two eigenvalues $(\omega_{in01}^2, \omega_{in02}^2)$ corresponding to the 0^{th}-order circumferential rotation mode and breathing mode are obtained, respectively,

$$\omega_{in01}^2 = \frac{k_v}{\rho A}, \quad \omega_{in02}^2 = \frac{R^2k_u+EA}{R^2\rho A}. \tag{2.24}$$

Similarly, the solution of the natural frequency of out-of-plane vibration is derived. The characteristic equation for out-of-plane vibration has a similar form to the one for in-plane vibration, i.e.,

$$\begin{vmatrix}
-\frac{EI_r}{R^4}n^4-\frac{GI_p}{R^4}n^2-k_w+\rho A\omega_n^2 & -\frac{EI_r}{R^3}n^2-\frac{GI_p}{R^3}n^2\\
-\frac{EI_r}{R^3}n^2-\frac{GI_p}{R^3}n^2 & -\frac{EI_r}{R^2}-\frac{GI_p}{R^2}n^2-k_u\frac{b_{op}^2}{4}+\rho I_p\omega_n^2
\end{vmatrix}=0 \tag{2.25}$$

Eq. (2.25) is reformed as,

$$\rho\omega_n^4+\rho\omega_n^2\left[\frac{1}{\rho I_p}\left(-\frac{EI_r}{R^2}-\frac{GI_p}{R^2}n^2-k_u\frac{b_{op}^2}{4}\right)+\frac{1}{\rho A}\left(-\frac{EI_r}{R^4}n^4-\frac{GI_p}{R^4}n^2-k_w\right)\right]+\frac{k_wk_ub_{op}^2}{4I_p\rho A}$$
$$+\frac{k_ub_{op}^2}{4I_p\rho A}\left(\frac{EI_r}{R^4}n^4+\frac{GI_p}{R^4}n^2\right)+\frac{k_w}{I_p\rho A}\left(\frac{EI_r}{R^2}+\frac{GI_p}{R^2}n^2\right)+\frac{EI_rGI_p}{\rho AR^6}n^2\left(n^2-1\right)^2=0. \tag{2.26}$$

The natural frequency of the out-of-plane vibration is expressed as,

$$\omega^2=\frac{B_2\pm\sqrt{{B_2}^2-4C_2}}{2R^2}, \tag{2.27}$$

where

$$B_2=\frac{1}{\rho I_p}\left(GI_pn^2+EI_r+k_u\frac{b_{op}^2}{4}R^2\right)+\frac{1}{\rho A}\left(\frac{GI_p}{R^2}n^2+\frac{EI_r}{R^2}n^4+k_wR^2\right),$$
$$C_2=\frac{1}{\rho I_p\rho A}\left[\frac{GI_pEI_r}{R^2}n^2\left(n^2-1\right)^2+\frac{k_ub_{op}^2}{4}(GI_pn^2+EI_rn^4)\right]$$
$$+\frac{1}{\rho I_p\rho A}\left[k_wR^2\left(GI_pn^2+EI_r\right)+\frac{k_wk_ub_{op}^2R^4}{4}\right]. \tag{2.28}$$

Substituting $n=0$ into Eq. (2.27) yields two specific solutions $(\omega_{out01}^2,\omega_{out02}^2)$, which correspond to the 0^{th}-order torsional mode and the lateral translational mode,

$$\omega_{out01}^2=\frac{1}{\rho I_pR^2}\left(EI_r+k_u\frac{b_{op}^2}{4}R^2\right),\quad \omega_{out02}^2=\frac{k_w}{\rho A}. \tag{2.29}$$

2.4 Steady-state response of rings

In this section, the solutions of the three-dimensional steady-state responses are obtained. The displacements of the rotating ring subjected to a set of harmonic concentrated loads in both in-plane and out-of-plane directions are given. To solve for a set of harmonic unit forces (q_u, q_v, q_w) and moments (q_β, q_{Mx}, q_{Mz}) which are applied at the point $\phi_0=0$ on the mid-plane of the ring, a unified form of the external forces and moments is defined as

$$q(\theta,t)=Q\delta(\phi-\phi_0)\cos\left(\omega_ft\right), \tag{2.30}$$

where ω_f denotes the applied load frequency, $\delta(\phi-\phi_0)$ represents the Dirac delta function, ϕ_0 is the stationary angular coordinate of the applied load, and Q means the amplitude of external forces or moments. It is noted that Q has the same unit as the external force q. The in-plane external loads include the radial force q_u and circumferential force q_v, and the in-plane moment q_β. The out-of-plane loads include the lateral force q_w and the out-of-plane moments around the X and Z axes, i.e., q_{Mx} and q_{Mz}.

Substituting the expressions of the external loads into the equations of motion, Eqs. (2.16-2.19), a set of fourth-order partial differential equations is obtained. For convenience, the equations of motion are rewritten in the field of complex numbers. The external loads and the solutions are expressed in a complex form. It should be noted that the displacements are the real parts of these complex solutions.

2.4.1 In-plane displacements

First, the in-plane equations are discussed. The displacement u in the radial direction and v in the tangential direction are assumed to be periodic functions of the angular coordinate θ or ϕ. In order to obtain the analytical expressions of the three-dimensional displacements, the solutions are expanded by means of complex Fourier series as follows

$$\widetilde{u}(\theta,t)=\sum_{n=-\infty}^{+\infty} a_n(t)\mathrm{e}^{\mathrm{i}n\theta}, \tag{2.31}$$

$$\widetilde{v}(\theta,t)=\sum_{n=-\infty}^{+\infty} \mathrm{i}b_n(t)\mathrm{e}^{\mathrm{i}n\theta}, \tag{2.32}$$

where the tilde denotes the corresponding complex-valued solution of the equations of motion. The generalized coordinates can be defined as $a_n(t)=A_n e^{\mathrm{i}\omega_n t}$ and $b_n(t)=B_n e^{\mathrm{i}\omega_n t}$, where ω_n means the natural frequency. It is assumed that $A_n=-A_{-n}, B_n=-B_{-n}$. To keep the expressions consistent, the complex solutions, $\widetilde{u}$ and $\widetilde{v}$, are written in the same letters as the in-plane displacements, i.e., u and v. The expressions can be rearranged as

$$\widetilde{u}(\theta,t)=a_0(t)+2\sum_{n=1}^{+\infty} a_n(t)\mathrm{e}^{\mathrm{i}n\theta}, \tag{2.33}$$

$$\widetilde{v}(\theta,t)=\mathrm{i}b_0(t)+2\sum_{n=1}^{+\infty} \mathrm{i}b_n(t)\mathrm{e}^{\mathrm{i}n\theta}. \tag{2.34}$$

Substituting Eqs. (2.33-2.34) into the equations of motion in the rotating coordination, Eqs. (2.16)

and (2.17), the fourth-order partial differential equations are reduced to a set of linear second-order ordinary differential equations with the generalized coordinates $a_n(t)$ and $b_n(t)$. With the mode order $n \geq 1$, the equations are then expressed as follows

$$\begin{bmatrix} m_{11} & 0 \\ 0 & m_{11} \end{bmatrix} \begin{Bmatrix} \ddot{a}_n \\ \ddot{b}_n \end{Bmatrix} + \begin{bmatrix} c_u & \mathrm{i}g_{1n} \\ \mathrm{i}g_{1n} & c_v \end{bmatrix} \begin{Bmatrix} \dot{a}_n \\ \dot{b}_n \end{Bmatrix} + \begin{bmatrix} k_{11} & k_{12} \\ k_{12} & k_{13} \end{bmatrix} \begin{Bmatrix} a_n \\ b_n \end{Bmatrix} = \begin{Bmatrix} \xi_{n1} \\ \xi_{n2} \end{Bmatrix}, \ (n \geq 1), \tag{2.35}$$

in which

$$\begin{aligned} m_{11} &= \rho A, \quad g_{1n} = -2\rho A\Omega, \\ k_{11} &= \frac{EA}{R^2} + \frac{EI_z}{R^4}n^4 + \frac{\sigma_\theta^0 A}{R^2}\left(1+n^2\right) - \rho A\Omega^2 - \frac{bp_0}{R} + k_u, \\ k_{12} &= -\frac{EA}{R^2}n - \frac{EI_z}{R^4}n^3 - \frac{2\sigma_\theta^0 A}{R^2}n + \frac{bp_0}{R}n, \\ k_{13} &= \frac{EA}{R^2}n^2 + \frac{EI_z}{R^4}n^2 + \frac{\sigma_\theta^0 A}{R^2}\left(1+n^2\right) - \rho A\Omega^2 - \frac{bp_0}{R} + k_v. \end{aligned} \tag{2.36}$$

It is noted that the elements of these matrices can be represented by physical and geometric parameters. Additionally, the rotation effect leads to the radial and circumferential deformations coupling through the gyroscopic term g_n. By considering the orthogonality of trigonometric functions, the generalized forces ξ_{n1} and ξ_{n2} are expressed as

$$\xi_{n1} = \frac{1}{2\pi}\int_0^{2\pi}\left(q_u + \frac{1}{R}q'_\beta\right)\mathrm{e}^{-\mathrm{i}n\theta}\mathrm{d}\theta, \tag{2.37}$$

$$\xi_{n2} = \frac{1}{2\pi\mathrm{i}}\int_0^{2\pi}\left(q_v + \frac{1}{R}q_\beta\right)\mathrm{e}^{-\mathrm{i}n\theta}\mathrm{d}\theta. \tag{2.38}$$

The complex form of the in-plane external loads is given as follows

$$q_u(\theta,t) = Q_u\delta\left(\phi-\phi_0\right)\mathrm{e}^{\mathrm{i}\omega_f t} = Q_u\delta\left(\theta-(\phi_0-\Omega t)\right)\mathrm{e}^{\mathrm{i}\omega_f t}, \tag{2.39}$$

$$q_v(\theta,t) = Q_v\delta\left(\phi-\phi_0\right)\mathrm{e}^{\mathrm{i}\omega_f t} = Q_v\delta\left(\theta-(\phi_0-\Omega t)\right)\mathrm{e}^{\mathrm{i}\omega_f t}, \tag{2.40}$$

$$q_\beta(\theta,t) = Q_\beta\delta\left(\phi-\phi_0\right)\mathrm{e}^{\mathrm{i}\omega_f t} = Q_\beta\delta\left(\theta-(\phi_0-\Omega t)\right)\mathrm{e}^{\mathrm{i}\omega_f t}. \tag{2.41}$$

Here, Q_u, Q_v, and Q_β are the amplitudes of the radial and circumferential forces and the in-plane moment, respectively, $\delta(\phi-\phi_0)$ represents a concentrated point force acting at a specified point ϕ_0 in the non-rotating coordinate system or the corresponding point $\theta_0 = \phi_0 - \Omega t$ in the rotating

coordinate system. Substituting Eqs. (2.39-2.41) into Eqs. (2.37) and (2.38), the generalized forces in the rotating coordinate system are obtained, i.e.,

$$\xi_{n1} = \frac{1}{2\pi}\left(Q_u + \mathrm{i}\frac{n}{R}Q_\beta\right)\mathrm{e}^{-\mathrm{i}n(\phi_0-\Omega t)}\mathrm{e}^{\mathrm{i}\omega_f t}, \tag{2.42}$$

$$\xi_{n2} = \frac{1}{2\pi\mathrm{i}}\left(Q_v + \frac{1}{R}Q_\beta\right)\mathrm{e}^{-\mathrm{i}n(\phi_0-\Omega t)}\mathrm{e}^{\mathrm{i}\omega_f t}. \tag{2.43}$$

The steady-state response can be obtained by using the method of undetermined coefficients. The complex-valued solutions take the following forms

$$\widetilde{u}(\phi,t) = \sum_{n=1}^{+\infty}\mathbf{A}_{un}^{\mathbf{T}}\mathbf{Q}_{in}\mathrm{e}^{-\mathrm{i}n(\phi_0-\phi+\gamma_{n1})}\mathrm{e}^{\mathrm{i}\omega_f t}, \tag{2.44}$$

$$\widetilde{v}(\phi,t) = \sum_{n=1}^{+\infty}\mathbf{A}_{vn}^{\mathbf{T}}\mathbf{Q}_{in}\mathrm{e}^{-\mathrm{i}n(\phi_0-\phi+\gamma_{n1})}\mathrm{e}^{\mathrm{i}\omega_f t}, \tag{2.45}$$

where $\mathbf{Q}_{in} = \left\{Q_u\ Q_v\ Q_\beta\right\}^{\mathbf{T}}$ denotes the vector of the amplitudes of the radial and circumferential line forces and the in-plane moment. The vectors of the complex-valued coefficients, $\mathbf{A}_{un}$ and $\mathbf{A}_{vn}$, are given in the Appendix A. It can be found from Eqs. (2.44) and (2.45) that the in-plane response is time independent and the total phase lag which affects the response is influenced by two factors. One impact is from the term $n\gamma_{n1}$, which is a function of both, Coriolis and damping effects associated with the rotation of the ring, and another one is from the external forces $\mathbf{Q}_{in}$.

For a special case, where $n=0$, the terms can be derived similarly. Eqs. (2.44) and (2.45) are reduced to

$$\widetilde{u}(\phi,t)|_{n=0} = \frac{1}{2\pi\sqrt{B_1^2+B_2^2}}\left[(B_3+\mathrm{i}B_4)Q_u + \mathrm{i}A_{12}\left(Q_v+\frac{Q_\beta}{R}\right)\right]\mathrm{e}^{\mathrm{i}\omega_f t}, \tag{2.46}$$

$$\widetilde{v}(\phi,t)|_{n=0} = \frac{1}{2\pi\sqrt{B_1^2+B_2^2}}\left[-\mathrm{i}(B_5+\mathrm{i}B_6)\left(Q_v+\frac{Q_\beta}{R}\right) - A_{12}Q_u\right]\mathrm{e}^{\mathrm{i}\omega_f t}. \tag{2.47}$$

By considering the expressions of the external loads, it can be found that the displacements are the real parts of the solutions, Eqs. (2.44-2.47). Therefore, the radial and circumferential displacements are given as

$$u(\phi,t) = \Re\left\{\widetilde{u}(\phi,t)\right\}, \tag{2.48}$$

$$v(\phi,t) = \Re\left\{\widetilde{v}(\phi,t)\right\}, \tag{2.49}$$

where $\Re\{\}$ denotes the real part of a complex value.

2.4.2 Out-of-plane displacements

The solutions of the out-of-plane displacements are derived and solved similarly to the in-plane solutions. With a set of out-of-plane external loads (q_w, q_{Mx} and q_{Mz}), the complex solutions of the lateral displacement and the torsional angle are expressed as

$$\widetilde{w}(\theta,t) = c_0(t) + 2\sum_{n=1}^{+\infty} c_n(t)\mathrm{e}^{\mathrm{i}n\theta}, \tag{2.50}$$

$$\widetilde{\phi}_\theta(\theta,t) = d_0(t) + 2\sum_{n=1}^{+\infty} d_n(t)\mathrm{e}^{\mathrm{i}n\theta}. \tag{2.51}$$

Similarly, the second-order ordinary differential equations for the out-of-plane motion in generalized coordinates $c_n(t) = C_n e^{\mathrm{i}\omega_n t}$ and $d_n(t) = D_n e^{\mathrm{i}\omega_n t}$ are given by

$$\begin{bmatrix} m_{21} & m_{22} \\ m_{22} & m_{23} \end{bmatrix} \begin{Bmatrix} \ddot{c}_n \\ \ddot{d}_n \end{Bmatrix} + \begin{bmatrix} c_w & \mathrm{i}g_{2n} \\ \mathrm{i}g_{2n} & c_u\frac{b_{op}^2}{4} \end{bmatrix} \begin{Bmatrix} \dot{c}_n \\ \dot{d}_n \end{Bmatrix} + \begin{bmatrix} k_{21} & k_{22} \\ k_{22} & k_{23} \end{bmatrix} \begin{Bmatrix} c_n \\ d_n \end{Bmatrix} = \begin{Bmatrix} \xi_{n3} \\ \xi_{n4} \end{Bmatrix}, \ (n \geq 1), \tag{2.52}$$

with

$$\begin{aligned} &m_{21} = \rho A, \quad m_{22} = -\frac{\rho I_z}{R}, \quad m_{23} = \rho I_\rho, \quad g_{2n} = \frac{\rho I_r}{R}\Omega n, \\ &k_{21} = \frac{EI_r}{R^4}n^4 + \frac{GI_\rho}{R^4}n^2 + k_w, \quad k_{22} = \frac{EI_r}{R^3}n^2 + \frac{GI_\rho}{R^3}n^2, \\ &k_{23} = \frac{EI_r}{R^2} + \frac{GI_\rho}{R^2}n^2 + \frac{b_{op}^2}{4}k_u. \end{aligned} \tag{2.53}$$

Note that these coefficients are not only related to the out-of-plane parameters but also associated with the in-plane parameters. Here, a new equivalent parameter of the width in terms of nominal width b_{op} is introduced by considering the mass involved in the out-of-plane vibration. Furthermore, the complex-valued solutions of the out-of-plane displacements are represented as

$$\widetilde{w}(\phi,t) = \sum_{n=1}^{+\infty} \mathbf{A}_{wn}^{\mathbf{T}}\mathbf{Q}_{out}\mathrm{e}^{-\mathrm{i}n(\phi_0-\phi+\gamma_{n2})}\mathrm{e}^{\mathrm{i}\omega_f t}, \tag{2.54}$$

$$\widetilde{\phi}_\theta(\phi,t) = \sum_{n=1}^{+\infty} \mathbf{A}_{\phi n}^{\mathbf{T}}\mathbf{Q}_{out}\mathrm{e}^{-\mathrm{i}n(\phi_0-\phi+\gamma_{n2})}\mathrm{e}^{\mathrm{i}\omega_f t}, \tag{2.55}$$

$$\widetilde{w}(\phi,t)|_{n=0} = \frac{1}{2\pi\sqrt{D_1^2+D_2^2}}\left[(D_3+\mathrm{i}D_4)\,Q_w - C_{12}Q_{Mx}\right]\mathrm{e}^{\mathrm{i}\omega_f t}, \tag{2.56}$$

$$\widetilde{\phi}_\theta(\phi,t)\Big|_{n=0} = \frac{1}{2\pi\sqrt{D_1^2+D_2^2}}\left[(D_5Q_{Mx} - C_{12}Q_w) + \mathrm{i}D_6Q_{Mx}\right]\mathrm{e}^{\mathrm{i}\omega_f t}, \tag{2.57}$$

where $\mathbf{Q}_{out} = \{Q_w \quad Q_{Mx} \quad Q_{Mz}\}^{\mathbf{T}}$ is the vector of the amplitudes of the lateral force and the out-of-plane moments around the X and Z axes. Accordingly, the lateral displacement and the torsional angle are given as

$$w(\phi,t) = \Re\left\{\widetilde{w}(\phi,t)\right\}, \tag{2.58}$$

$$\phi_\theta(\phi,t) = \Re\left\{\widetilde{\phi}_\theta(\phi,t)\right\}. \tag{2.59}$$

The expansions of the in-plane and out-of-plane displacements can be truncated beyond the first n modes considering the acceptable error bound of percentage to the displacements.

2.5 Numerical examples

2.5.1 Validation of the model

In the author's [32] previous work, the natural frequency analysis of the tire was presented and the effectiveness of the three-dimensional ring model in describing the free vibration characteristics of the tires was verified. A set of experimental results of the natural frequencies has been obtained by using the hammering excitation method. It has been applied to validate the effectiveness of the identified parameters of the ring model. Here, the modal superposition method is used to calculate the steady-state response of the tire. The parameters of the model for this calculation are taken from [32]. Fig. 2.2 shows the relation between the amplitudes of the in-plane and out-of-plane displacements A_{ni} and the order number n of the modes. It is observed from Fig. 2.2 that the amplitudes A_{ni} are greatly decreasing with the increment of the order number n. In this section, the truncated number of modes n is selected to be 30.

The steady-state response of the tire is calculated by using the present numerical model, and corresponding results are compared with Gong's method [44] as shown in Fig. 2.3. As Gong only gave the solution for the in-plane displacements, the comparisons presented here are only for u and v.

It is found that the calculated results from the present model are in good agreement with Gong's

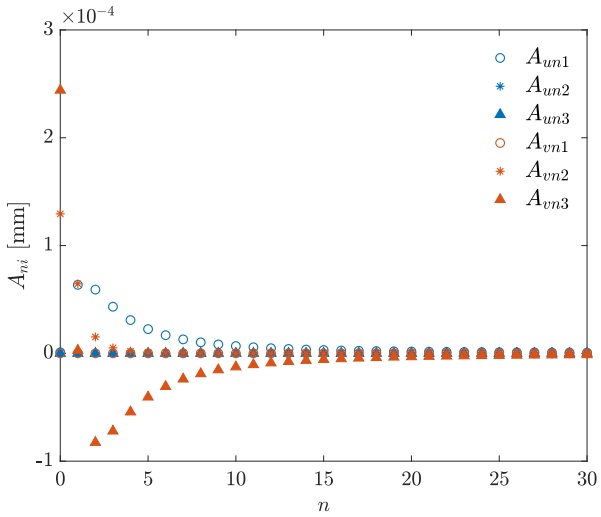

(a) Coefficients corresponding to in-plane displacements.

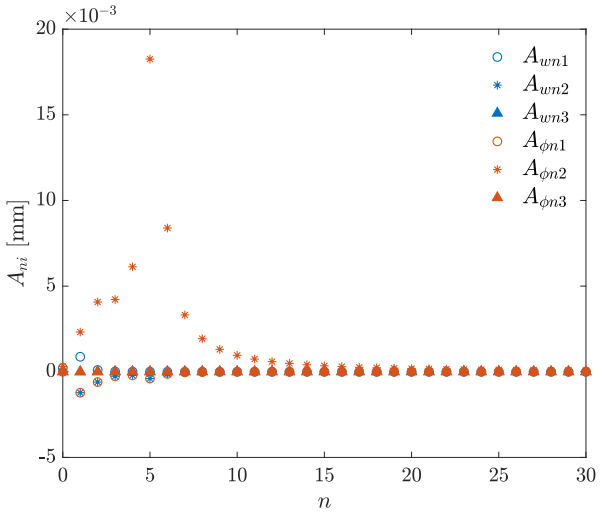

(b) Coefficients corresponding to out-of-plane displacements.

Figure 2.2: Relation between the amplitudes of displacements A_{ni} and the order number n of modes.

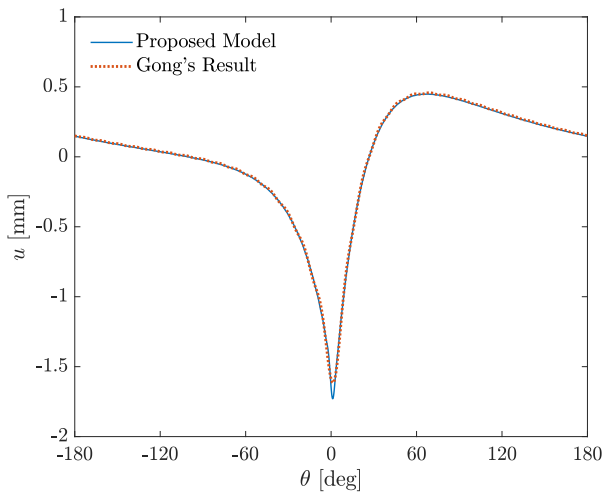

(a) Radical displacement u.

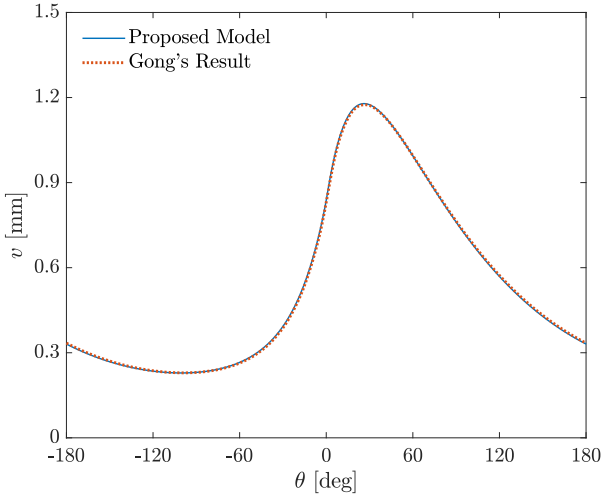

(b) Circumferential displacement v.

Figure 2.3: Comparison of steady-state displacements with Gong's method [44].

results. Furthermore, the equations for a tire with high circumferential stiffness can be simplified by using the assumption of in-extensibility without losing much precision. However, some special modes are not obtained due to the limit of deformation.

2.5.2 Evaluation parameter-equivalent radiated sound power

One characteristic of sound radiation is a proper evaluation index to describe the overall dynamic response of a structure. It can be determined by the vibrating velocity of the structural surface. However, the determination of the accurate sound radiation power is generally a fluid-structure interaction problem, and the convergence speed of the corresponding calculation is rather slow. Therefore, the equivalent radiated sound power is selected as a simplified evaluation scale to describe the maximum radiated sound power of a vibrating structure [119]. It is assumed that the vibrating surface is rigid, and the radiation efficiency is assumed to be 1. Accordingly, the equivalent radiated sound power is stated as

$$P(\omega) = \frac{1}{2}\rho c \int_A |\upsilon(\omega)|^2 \mathrm{d}A, \tag{2.60}$$

where P represents the sound power, A is the vibrating surface, υ denotes the velocity, ω means the angular frequency of the vibration, and c represents the speed of sound. When the uncertainty is introduced into the system, the vibrating velocity υ will become a random parameter and influence the probability characteristics of the radiated sound power.

2.5.3 Numerical results

In this section, the solutions of the steady-state response and the equivalent radiated sound power for the tire are presented. When the tire is rolling steadily on a perfectly flat road, the amplitude of external forces or moments can be considered as a constant. In order to analyze the responses of the tire under different excitation frequencies, $f = \omega_f/2\pi$, a sweep excitation varying from 1Hz to 200Hz is selected. Fig. 2.4 shows the radial displacement and torsional angle $(u_f, \phi_{\theta f})$ at the load acting point on the middle line of the ring. The effect of rotation is also shown. Regardless of the damping effect, it is observed from Fig. 2.4 that the positions of the resonance peaks are consistent with the natural frequencies given in [32]. The accuracy of the present numerical model is proved. Further, the rotating speed leads to a splitting of natural frequencies. However, this splitting due to rotation does not apply for the 0^{th}-order natural frequencies.

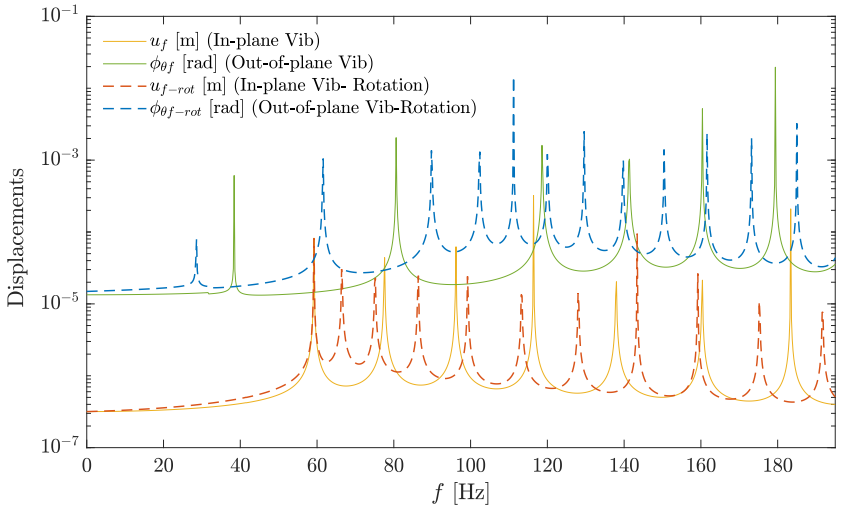

Figure 2.4: Radial displacement and torsional angle at the load acting point on the middle line of the ring under different excitation frequencies.

For sound radiation analysis, the velocity of the vibrating surface is calculated by taking the derivative with respect to displacements. For a more practical consideration, the damping of the sidewall is taken into account for the calculation of the equivalent radiated sound power. Considering the situation that the thickness of the equivalent ring is far less than the width, the acoustic power contributed by the velocity on the side surfaces is not considered. The corresponding results are given in Fig. 2.5. It is shown that the damping effect reduces the amplitude of the equivalent radiated sound power and decreases the resonance peaks. In the following section, the random distribution of the sound power radiation is discussed based on the deterministic dynamic results shown in this part.

2.6 Summary

In this chapter, a theoretical three-dimensional ring model was established for describing the in-plane and out-of-plane vibrations as well as the steady-state response of tires. Especially, the out-of-plane deformation was completely discussed. Additionally, by relaxing the in-extensibility assumption and considering the out-of-plane deformation, the analytical expression of the steady-state response was given. By comparing the solutions with the results proposed in [44], it is shown that, for a tire with high circumferential stiffness, the equations can be simplified by using the assumption of in-extensibility without losing much precision, but some special modes (breathing mode) cannot be obtained due to the limitation of the deformation. In the sound radiation analysis, the concept

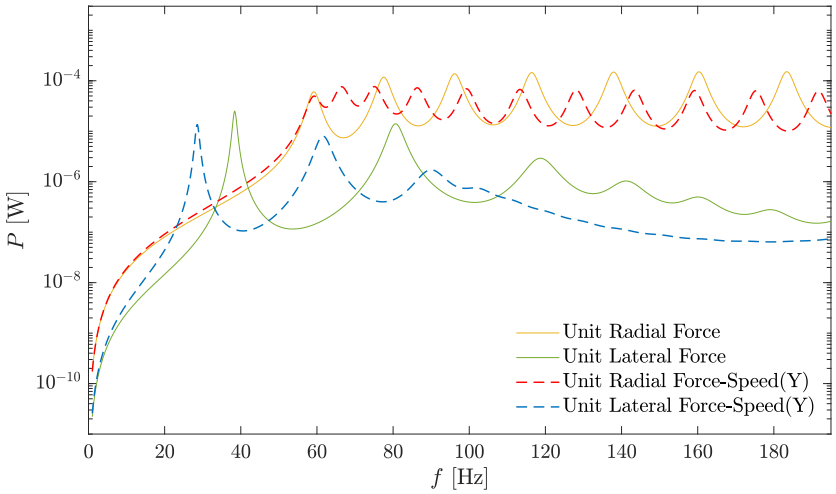

Figure 2.5: Equivalent radiated sound power of the belt ring under different excitation frequencies.

of the equivalent radiated sound power was introduced to evaluate the overall vibrating velocity of the ring surface, consisting of the in-plane and out-of-plane bending and lateral torsion. From the foregoing analysis, it is found that the rolling speed results in a mode splitting. However, this splitting due to rotation does not apply for the 0^{th}-order natural frequencies.

Chapter 3

Coupled Rigid-flexible Ring Model

Based on the existing 2D flexible ring model and the assumption of the rigid ring, an innovative coupled rigid-flexible ring model is developed in this section. Moreover, the tire-road contact model in the literature [120] is extended to the case of uneven road surfaces, so that the proposed algorithm can be applied to more extensive scenarios. Compared with the classic rigid ring models, the model presented herein can well reflect the geometric design parameters of the tires, and even uniformity parameters can be introduced into the expression of the model.

3.1 A brief overview of two kinds of ring models

Throughout the years, trying to concisely and accurately model the physical properties of tires and their interaction with the road surface has been a key issue in automotive dynamics analysis. To evaluate the impacts of the tire structural parameters and the uniformity parameters, the analysis model is required to have the ability to describe the structural and material properties of tires. As mentioned in the literature review, ring models not only provide a fundamental description of the tire structure but can also ensure a concise mathematical solution [13, 28, 29]. The previous works have categorized the tire ring models as rigid ring models [13, 121, 122] and flexible ring models [16, 17]. While the rigid ring model has fewer DOFs and is much faster to compute, the determination of its tire-road contact has unavoidable drawbacks. The calculation of contact forces is usually achieved by establishing an equivalent road surface [13, 14]. This simplification limits the model bandwidth to approx. 80Hz. The description of the physical properties using the flexible ring models is more consistent with the actual structure of tires than the simplification of the rigid ring models. Therefore, the model is more complex but can reach an application range up to 200Hz [16, 17].

In this work, a 2D ring model is developed for analyzing the dynamic response in the wheel plane. Herein, a coupled model combining rigid and flexible rings is proposed, that enables the description of the elastic deformation of tires while achieving a fast solution process of the transient dynamic analysis. The coupled rigid-flexible ring model is mainly composed of three components: a flexible ring, a rigid ring, and a damped spring element simplified by the sidewall of tires. First, the flexible ring model is used to theoretically analyze the deformation and contact characteristics of the tire to obtain the steady-state deformation of the tire and the forces on the contact patch. Meanwhile, the rigid ring model is applied to solve the overall motion and dynamic response of the tire. Eventually, the coupling relationship between these two ring models is established, and the complete theoretical expression and the calculation process of the coupled rigid-flexible ring model are given, laying a theoretical foundation for the analysis of the tire dynamics.

3.2 Modeling for tire dynamics

3.2.1 2D flexible ring model

Firstly, the 2D flexible ring model in the coupled rigid-flexible ring model is introduced. Herein, a radial tire is simplified and transformed into a ring-shape structure on an elastic foundation. It aims to obtain the steady-state deformation and contact properties. A 2D flexible ring model is mainly composed of three parts. The steel belt and part of the carcass are equivalent to a 2D deformable ring that can be bent in the wheel plane. The sidewall and the inflation effect are assumed to be a damped elastic foundation. A uniform pressure distribution generated by tire pressure is applied to the inner surface. A set of radial and circumferential distribution springs (k_u, k_v) is introduced to describe the elastic properties of the foundation, respectively. The damping effect of the sidewall is described by the coefficients (c_u, c_v). The rim is assumed to be rigid. A schematic plot of a 2D flexible ring on an elastic foundation is shown in Fig. 3.1.

To solve for the steady-state response, it is supposed that only the pavement moves backward with a velocity of V_r, while the position of the flexible ring is fixed. At this moment, the ring only rotates in space with a speed of Ω. Considering the condition of the tire at a particular rotational speed, it is necessary to establish a set of proper coordinate systems to describe the deformation and the motion of the tire. In this work, a rotating polar coordinate system (r, θ) and a non-rotating polar coordinate system (r, ϕ) are employed, whose origins are at the center of the wheel. These polar coordinates can be used to define the position of any point on the ring. When describing the overall displacements of tires, a more concise form can be given in a non-rotating Cartesian

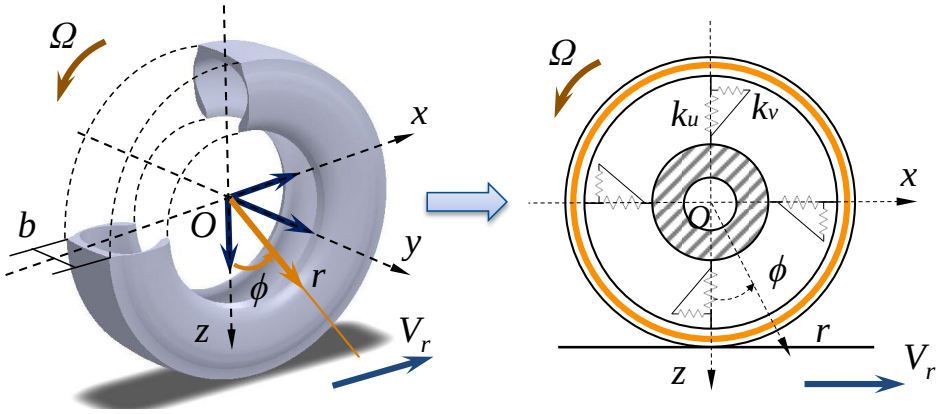

Figure 3.1: Illustration of the conversion of an actual tire structure to a 2D flexible ring model. The equivalent ring is fixed in space and rotates at a speed Ω. Meanwhile, the road surface moves backward with a velocity of V_r.

coordinate system (x, z) and a rotating Cartesian coordinate system (x_1, z_1). The x-axis is positive in the direction of the forward velocity of the road surface, and the z-axis is positive in the downward direction. As shown in Fig. 3.2, the angular coordinates ϕ and θ are assumed to be positive from the z-axis or z_1-axis in the counterclockwise direction.

The motion of the ring is described in terms of the radial and circumferential displacements (u_a, v_a), which are represented by the mid-plane displacements (u, v). The displacements of any point on the ring are given as

$$u_a = u, \tag{3.61}$$

$$v_a = v - (R - r)\frac{v - u'}{R}, \tag{3.62}$$

where the prime $(\,)'$ designates differentiation with respect to θ. It is important to note that the difference between r and R, i.e., r is the r-axis coordinate, but R represents the constant mean radius of the ring. The in-plane equations of motion listed here have been adequately derived in the previous studies of the authors and other researchers [32, 44, 123].When the external generalized forces and moment (q_u, q_v, q_β) act on the middle-line of the ring, the equations of in-plane motions are represented as follows:

$$\begin{aligned} &\frac{EA}{R^2}\left(u + v'\right) + \frac{EI_z}{R^4}\left(u^{(4)} - v'''\right) + \frac{\sigma_\theta^0 A}{R^2}\left(u + 2v' - u''\right) \\ &+\rho A\left(\ddot{u} - 2\Omega\dot{v} - \Omega^2 u\right) - \frac{bp_0}{R}\left(u + v'\right) + k_u u + c_u\dot{u} = q_u + \frac{1}{R}q'_\beta, \end{aligned} \tag{3.63}$$

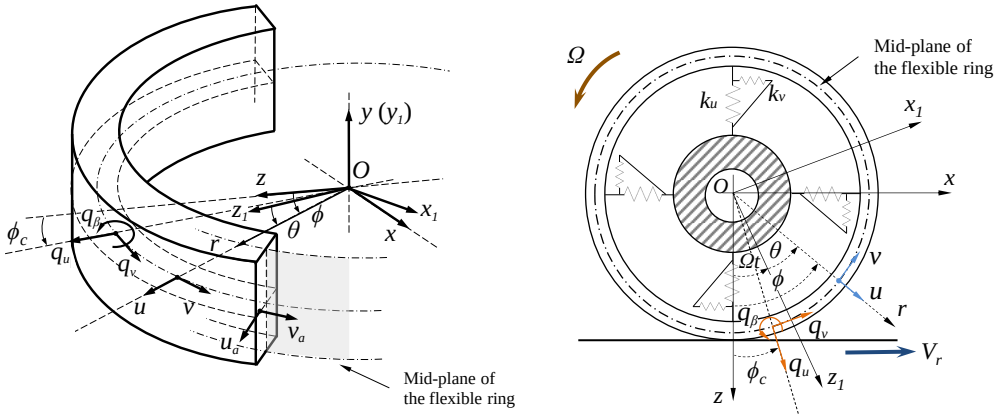

(a) Diagram of the flexible ring from the simplification of the belt and part of the carcass.

(b) The 2D flexible ring model and the definition of coordinate systems.

Figure 3.2: Schematic diagram of the displacements and coordinate systems of the flexible ring model. (The defined positive direction of the displacements and the generalized forces are shown.)

$$
\begin{aligned}
&-\frac{EA}{R^2}\left(u'+v''\right)+\frac{EI_z}{R^4}\left(u'''-v''\right)+\frac{\sigma_\theta^0 A}{R^2}\left(v-2u'-v''\right)\\
&+\rho A\left(\ddot{v}+2\Omega\dot{u}-\Omega^2 v\right)+\frac{bp_0}{R}\left(u'-v\right)+k_v v+c_v\dot{v}=q_v+\frac{1}{R}q_\beta,
\end{aligned}
\tag{3.64}
$$

in which b means the effective width, A indicates the area of the ring cross-section, ρ is the density, σ_θ^0 denotes the initial stress, and p_0 is the internal pressure on the inner surface. The dot $\dot{(\,)}$ denotes differentiation with respect to time t. Here, EA and EI_z respectively mean the membrane stiffness and the in-plane bending stiffness of the flexible ring.

Furthermore, the inextensibility assumption [44],which is adopted here to simplify the equations for a tire with high circumferential stiffness, supposes that the midline circumference of the treadband is invariable during deformation. The number of dynamic equations can be reduced without losing much accuracy [32, 123]. Under the inextensibility assumption, the circumferential normal strain ε_θ at the middle surface is given as

$$
\varepsilon_\theta=\frac{1}{R}\left(u+v'\right)=0. \tag{3.65}
$$

Then, the displacements of any point on the ring are represented as

$$
u=-v'. \tag{3.66}
$$

Differentiating Eq. (3.63) with respect to θ and substituting Eq. (3.66) into Eq. (3.63), then adding it

to Eq. (3.64), the equation of motion under the inextensibility assumption is obtained, (cf.[44, 123])

$$
\begin{aligned}
&-\frac{EI_z}{R^4}\left(v^{(6)}+2v^{(4)}+v''\right)-\frac{bp_0}{R}\left(v''+v\right)+\rho A\left[\ddot{v}-\ddot{v}''-4\Omega\dot{v}'+\Omega^2\left(v''-v\right)\right]\\
&+\frac{\sigma_\theta^0 A}{R^2}\left(v^{(4)}+2v''+v\right)-k_u v''+k_v v-c_u\dot{v}''+c_v\dot{v}=q_u{}'+q_v+\frac{1}{R}\left(q_\beta{}''+q_\beta\right).
\end{aligned}
\tag{3.67}
$$

To obtain the analytic expressions for in-plane displacements, the radial displacement u_a and the tangential displacement v_a are approximated as a periodic functions of the angular coordinates ϕ or θ. The mid-plane tangential displacement v is expanded by employing a modal expansion as follows,

$$
v(\theta,t)=\sum_{n=0}^{\infty}\left[a_n(t)\cos(n\theta)+b_n(t)\sin(n\theta)\right].
\tag{3.68}
$$

The generalized coordinates are defined as $a_{1n}(t)=\zeta_n\sin(\omega_n t)$ and $a_{2n}(t)=\zeta_n\cos(\omega_n t)$, where ω_{1n} means the n^{th}-order natural frequency and ζ_n is a constant. By the expression of the generalized coordinates $a_{1n}(t)$ and $a_{2n}(t)$, the equation of motion, Eq. (3.67), is simplified to a linear second-order ordinary differential equation,

$$
\mathbf{M}_n\ddot{\mathbf{a}}_n+\mathbf{C}_n\dot{\mathbf{a}}_n+\mathbf{G}_n\dot{\mathbf{a}}_n+\mathbf{K}_n\mathbf{a}_n=\boldsymbol{\xi}_n
\tag{3.69}
$$

where,

$$
\mathbf{M}_n=\begin{bmatrix} m_n & 0\\ 0 & m_n\end{bmatrix},\quad \mathbf{C}_n+\mathbf{G}_n=\begin{bmatrix} c_n & g_n\\ -g_n & c_n\end{bmatrix},\quad \mathbf{K}_n=\begin{bmatrix} k_n & 0\\ 0 & k_n\end{bmatrix},
$$

$$
\mathbf{a}_n=\begin{Bmatrix} a_{1n}\\ a_{2n}\end{Bmatrix},\quad \boldsymbol{\xi}_n=\begin{Bmatrix} \xi_{n1}\\ \xi_{n2}\end{Bmatrix}.
\tag{3.70}
$$

The coefficients are listed as

$$
\begin{aligned}
&m_n=\left(1+n^2\right)\rho A,\quad c_n=n^2c_u+c_v,\quad g_n=-4n\rho A\Omega,\\
&k_n=\left(1-n^2\right)^2\left(\frac{EI_z}{R^4}n^2+\frac{\sigma_\theta^0 A}{R^2}\right)+n^2k_u+k_v-\left(1-n^2\right)\frac{p_0 b}{R}-\left(1+n^2\right)\rho A\Omega^2,
\end{aligned}
\tag{3.71}
$$

and the generalized forces ξ_{n1} and ξ_{n2} given by

$$\xi_{n1} = \frac{1}{\pi}\int_0^{2\pi} [q_u{}' + q_v + \frac{1}{R}\left(q_\beta + q_\beta{}''\right)]\cos(n\theta)\mathrm{d}\theta, \tag{3.72}$$

$$\xi_{n2} = \frac{1}{\pi}\int_0^{2\pi} [q_u{}' + q_v + \frac{1}{R}\left(q_\beta + q_\beta{}''\right)]\sin(n\theta)\mathrm{d}\theta. \tag{3.73}$$

When a set of radial and tangential concentrated forces and in-plane moment (q_u, q_v, q_β) are applied to the point θ_c, the normalized form of the in-plane external forces in the rotating coordinate system is written as

$$q_u(\theta,t) = Q_u\delta\left(\theta-\theta_c\right), \tag{3.74}$$

$$q_v(\theta,t) = Q_v\delta\left(\theta-\theta_c\right), \tag{3.75}$$

$$q_\beta(\theta,t) = Q_\beta\delta\left(\theta-\theta_c\right), \tag{3.76}$$

in which Q_u and Q_v represent the amplitudes of the radial and circumferential forces, respectively, Q_β is the in-plane moment, and $\delta(\theta-\theta_c)$ indicates the angular coordinate of the generalized force acting at the position θ_c in the rotating coordinate system or the corresponding coordinate in the non-rotating coordinate system $\phi_c = \theta_c + \Omega t$. The expressions of the generalized forces under the concentrated forces in the rotating coordinate are derived as

$$\xi_{n1} = \frac{1}{\pi}\left[\left(Q_v + \left(1-n^2\right)Q_\beta\right)\cos(n\theta_c) + nQ_u\sin(n\theta_c)\right], \tag{3.77}$$

$$\xi_{n2} = \frac{1}{\pi}\left[\left(Q_v + \left(1-n^2\right)Q_\beta\right)\sin(n\theta_c) - nQ_u\cos(n\theta_c)\right]. \tag{3.78}$$

Especially, when $n = 0$

$$\xi_{01} = \frac{1}{2\pi}\left(Q_v + Q_\beta\right), \quad \xi_{02} = 0. \tag{3.79}$$

It should be noted that the equations of motion are established in the rotating coordinate system. In order to obtain the solution in the non-rotating coordinate system, the tangential displacement v is given in a similar form to Eq. (3.68) as

$$v(\phi,t) = \sum_{n=0}^{\infty}\left[\bar{a}_n(t)\cos(n\phi) + \bar{b}_n(t)\sin(n\phi)\right]. \tag{3.80}$$

Substituting the transformation equation $\theta = \phi - \Omega t$ into the expression of $v(\theta,t)$ and comparing the coefficients, the relationship between these expressions in two coordinate systems is given as

follows,

$$\begin{cases} a_{1n} = \bar{a}_{1n}\cos(n\Omega t) + \bar{a}_{2n}\sin(n\Omega t) \\ a_{2n} = -\bar{a}_{1n}\sin(n\Omega t) + \bar{a}_{2n}\cos(n\Omega t) \end{cases}. \tag{3.81}$$

The expression for the tangential displacement under the concentrated forces acting at the specific location ϕ_c in the non-rotating coordinate system by employing the method of undetermined coefficients is written as

$$v(\phi,t) = \sum_{n=1}^{\infty} \left\{ A_{n1}\left(Q_v + \left(1-n^2\right)Q_\beta\right)\cos\alpha + A_{n2}Q_w\sin\alpha \right\}. \tag{3.82}$$

with

$$\begin{aligned} A_{n1} &= \left(\pi\sqrt{(M_n - G_n)^2 + C_n^2}\right)^{-1}, \quad A_{n2} = nA_{n1}, \quad \alpha = n\left(\phi_c - \phi + \gamma_n\right), \\ M_n &= -(n\Omega)^2 m_n + k_n, \quad G_n = ng_n\Omega, \quad C_n = nc_n\Omega, \quad \gamma_n = \frac{1}{n}\arctan\left(\frac{C_n}{M_n - G_n}\right). \end{aligned} \tag{3.83}$$

When the flexible ring is discretized, the overall tangential displacement and the corresponding radial displacement is obtained by superimposing the response under the action of each concentrated force, i.e.,

$$u(\phi,t) = \sum_{k=1}^{N_c}\sum_{n=1}^{\infty}\left[-nA_{n1}\left(Q_{vk} + \left(1-n^2\right)Q_{\beta k}\right)\sin\alpha_k + nA_{n2}Q_{uk}\cos\alpha_k\right], \tag{3.84}$$

$$v(\phi,t) = \sum_{k=1}^{N_c}\sum_{n=1}^{\infty}\left[A_{n1}\left(Q_{vk} + \left(1-n^2\right)Q_{\beta k}\right)\cos\alpha_k + A_{n2}Q_{uk}\sin\alpha_k\right], \tag{3.85}$$

$$\alpha_k = n\left(\phi_{ck} - \phi + \gamma_n\right). \tag{3.86}$$

Here, N_c denotes the total number of nodes in the contact patch. Moreover, Eqs. (3.84-3.85) are expressed in matrix form as

$$\mathbf{U} = \mathbf{TQ}, \tag{3.87}$$

in which $\mathbf{U}$ is the matrix of the displacements of the ring, $\mathbf{T}$ denotes the compliance matrix, and $\mathbf{Q}$ represents the matrix of generalized forces. The coefficients of these matrices are given in B.1. Once the generalized forces (q_u, q_v, q_β) acting on the ring are given, the mid-plane displacements

(u, v) on the ring are calculated from Eq. (3.87). Additionally, the displacements at any point on the flexible ring also can be calculated.

3.2.2 Contact pressure distribution

Since the flexible ring, i.e., the structure equivalent to the tire belt and carcass, is not directly in contact with the road surface, the actual deformation is unknown beforehand. It means that the displacements of the ring cannot be straightforwardly calculated by Eq. (3.87). In the contact area with the ground, the displacements of the ring and the tread rubber should match each other to satisfy the geometric compatibility condition [120]. The displacements of the ring and the tread rubber in undeformed and deformed states are shown in Fig. 3.3.

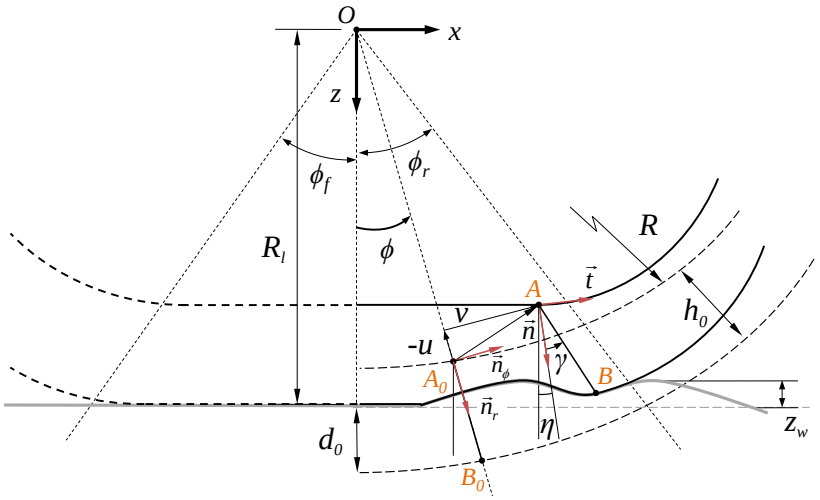

Figure 3.3: Geometric compatibility condition between the displacements of the ring and the tread rubber in undeformed and deformed states.

Under a given vertical deflection d_0, the points A_0 and B_0 on the ring and the tread surface shift to the corresponding new positions A and B. The rotation angle of the cross-section of the ring β is expressed as

$$\beta = \frac{v - u'}{R}. \tag{3.88}$$

By introducing the change in curvature of the deformed flexible ring described by the deflection angle of the normal to the ring η (see Fig. 3.3), the deflection and rotation angles of the cross-section of the ring at any given coordinate ϕ are related by

$$\eta = \phi + \beta. \tag{3.89}$$

Considering small deformations on the tread surface, the angle between the normal to the ring and the tread surface γ simultaneously affects the normal and tangential deformations of the tread rubber, i.e., $v_s = \gamma u_s$, where (u_s, v_s) are the normal and tangential deformations on the tread surface. Therefore, with a determined overall vertical deflection, the vector from the wheel center O to any point B on the deformed tread surface is expressed as

$$\mathbf{r}_{OB} = \mathbf{r}_{OA_0} + \mathbf{r}_{A_0A} + \mathbf{r}_{AB} = \left[(R+u)\,\mathbf{n}_r + v\mathbf{n}_\phi\right] + (u_s\mathbf{n} + v_s\mathbf{t})\,, \tag{3.90}$$

where η means the declination angle, $(\mathbf{n}_r, \mathbf{n}_\phi)$ are unit vectors in the radial (i.e., normal) and tangential directions at points on the undeformed flexible ring, and $(\mathbf{n}, \mathbf{t})$ are unit vectors in the normal and tangential directions on the deformed flexible ring. Under a given overall vertical deformation, the change in curvature of the deformed flexible ring is expressed by the declination of the normal to the ring η which also simultaneously affects the tangential deformation on the surface of the tread rubber. In this case, the normal and tangential displacements of the tread rubber (u_s, v_s) and the declination angle η at any coordinate ϕ are expressed respectively as

$$x_B = (R+u_b)\sin\phi + v_b\cos\phi + u_s\sin\eta + v_s\cos\eta, \tag{3.91}$$

$$z_B = (R+u_b)\cos\phi - v_b\sin\phi + u_s\cos\eta - v_s\sin\eta, \tag{3.92}$$

$$\eta = \phi + \beta. \tag{3.93}$$

Meanwhile, the coordinates (x_B, z_B) of the point B on the deformed tread surface should be constrained by the friction and the uneven geometry of the pavement surface. The constraint equations in the contact area are

$$x_B = R_e\Omega, \tag{3.94}$$

$$z_B = R_l - z_w, \tag{3.95}$$

where R_l is the loaded radius, i.e., the height of the location of the wheel center from the road profile, R_e denotes the effective rolling radius, and z_w is the relative height of the pavement to the reference flat road surface. By combining Eqs. (3.89-3.95), the normal and tangential displacements on the surface of the tread rubber are solved as

$$u_s = -(R+u)\cos\beta - v\sin\beta + R_e\phi\sin\eta + (R_l - z_w)\cos\eta, \tag{3.96}$$

$$v_s = (R+u)\sin\beta - v\cos\beta + R_e\phi\cos\eta - (R_l - z_w)\sin\eta. \tag{3.97}$$

Once the displacements of the treadband are calculated, the normal force F_{ns} and the tangential force F_{ts} acting on the tread surface are given by

$$F_{ns} = k_{Es}(u_s - h_0), \tag{3.98}$$

$$F_{ts} = k_{Gs} v_s, \tag{3.99}$$

where h_0 represents the undeformed thickness of the tread rubber, k_{Es} and k_{Gs} mean the normal stiffness and shear stiffness of the tread rubber corresponding to each unit length of treadband, respectively.

The following equations show the coordinate transformations between the normal and tangential forces of the treadband (F_{ns}, F_{ts}), the generalized forces acting on the ring (q_u, q_v, q_β), and the normal and shear traction pressure in the contact area (p_σ, p_τ). The forces under different basis vectors are determined as

$$\begin{Bmatrix} q_u(\phi) \\ q_v(\phi) \\ q_\beta(\phi) \end{Bmatrix} = \begin{bmatrix} \cos\beta & -\sin\beta \\ \sin\beta & \cos\beta \\ 0 & u_s \end{bmatrix} \begin{Bmatrix} F_{ns}(\phi) \\ F_{ts}(\phi) \end{Bmatrix}, \tag{3.100}$$

$$\begin{Bmatrix} p_\sigma(\phi) \\ p_\tau(\phi) \end{Bmatrix} = \begin{bmatrix} \cos\eta & -\sin\eta \\ \sin\eta & \cos\eta \end{bmatrix} \begin{Bmatrix} F_{ns}(\phi) \\ F_{ts}(\phi) \end{Bmatrix}. \tag{3.101}$$

In this chapter, the displacements are assumed to be small compared to the mean radius R, and then the terms involving the product of the small displacements (u, v) and the small declination angle η can be neglected. Thus, the nonlinear boundary conditions (3.96-3.97) and the transformation equations (3.100-3.101) are linearized. By substituting Eqs. (3.96-3.97) into Eq. (3.100) and rewriting it in matrix form, it results in a linearized force-deflection equation of the ring and the treadband as

$$\mathbf{Q} = \mathbf{F} + \mathbf{H}\mathbf{U}, \tag{3.102}$$

where $\mathbf{F}$ denotes the generalized force matrix associated with the deformation of the tread rubber, the parameters of which are independent of the displacement vector $\mathbf{U}$, and $\mathbf{H}$ is the coefficient

matrix associated with the displacements of the ring, which contains the coupling terms between the stiffness coefficients of the tread rubber and the displacements of the ring. The coefficients of these matrices are given in B.2. When the vertical overall deflection is determined, the contact forces are obtained by successive substitution of the approximate solution for each step into the exact boundary conditions (3.96-3.97) and the transformation equations (3.100-3.101).

After getting the distributed pressure $(p_\sigma(\phi_i), p_\tau(\phi_i))$ at each node in the contact area, the overall vertical force F_{cz} equals the sum of the distributed forces of each discrete element, i.e.,

$$F_{cz} = \sum_{i=1}^{N_c} p_\sigma(\phi_i). \tag{3.103}$$

For the longitudinal force F_{cx}, the concept of relaxation length is introduced in the rigid ring model to describe the hysteresis effect of longitudinal forces due to tread elasticity. This is because when the slip condition is changed, the longitudinal deformation will not occur simultaneously. The definition of the relaxation length is the distance traveled needed to reach 63% of the steady-state deflection after a step change, which is almost independent of the rolling speed [13, 14]. To calculate the longitudinal force existing in the contact area, the distributed contact pressure obtained from the steady-state flexible ring model is set as the nominal longitudinal force F_{cxn},

$$F_{cxn} = \sum_{i=1}^{N_c} p_\tau(\phi_i), \tag{3.104}$$

then, the actual longitudinal force F_{cx} is obtained by solving a first-order differential equation with respect to the relaxation length. The transient model in the form of longitudinal force [14, 124, 125] is given by,

$$\sigma_t \dot{F}_{cx} + |V_r| F_{cx} = |V_r| F_{cxn}. \tag{3.105}$$

Here, V_r is the velocity of the tire belt on the contact area. The relaxation length σ_t reads as,

$$\sigma_t = \frac{C_x}{C_{tx}}, \tag{3.106}$$

with

$$C_x = k_{tx} \cdot 2a^2, \tag{3.107}$$

$$C_{tx} = k_{tx} \cdot 2a\ , \tag{3.108}$$

in which C_x denotes the total longitudinal tire stiffness, C_{tx} is the total tread element stiffness, and k_{tx} means the longitudinal stiffness of the treadband with each unit length. Since the impacts of the tire uniformity parameters at low speed are considered in this thesis, the actual longitudinal slip under the simulation conditions remains within the linear region. Therefore, the relaxation length of the tread contact model used in Eq. (3.105) at full adhesion equals half of the contact length a [14, 125].

Because of the hysteresis loss caused by the elasticity of rubber, the contact pressure shows an asymmetric distribution at the center of the contact area, which leads to the generation of an additional moment. The expression for the rolling moment is given as follows:

$$M_{by} = \sum_{i=1}^{N_c} \sigma(\phi_i) \cdot R_e \sin\phi_i. \tag{3.109}$$

Eventually, the contact forces and the moment will be input into the rigid ring model as an excitation in the subsequent dynamics solution to calculate the transient response of the tire.

3.2.3 Rigid Ring

A complete dynamics model considering the elastic deformation and rotation effects of tires makes the partial differential equations of motion too complex for the solution and multi-body simulations. Therefore, to solve such kind of issues, the proposed model employs the assumption that the 1^{st}-order mode of tires can be utilized to approximate the in-plane transient response within 100Hz [126]. It means that the carcass and the belt remain as a rigid element during motion. For the primary application scenarios of the model, this simplification for multi-body dynamics is sufficient to cover the frequency range of the ride comfort analysis.

A rigid ring consists of the steel belt, part of the carcass, and the sidewall of a tire, which is connected to the rim by a 3-DOF spring and damper element. These two components, separately denoted by (k_{bx}, k_{bz}, $k_{b\theta}$) and (c_{bx}, c_{bz}, $c_{b\theta}$) in Fig. 3.4, represent the elastic and damping effect of the sidewall in the longitudinal, vertical, and circumferential directions.

The in-plane displacements of the rigid ring (x_b, z_b, θ_b) and the in-plane displacements of the rim (x_a, z_a, θ_a) are considered. In particular, the longitudinal DOF of the rim x_a will be determined when the wheel speed is constant. The in-plane equations of motion of the rigid ring and rim are

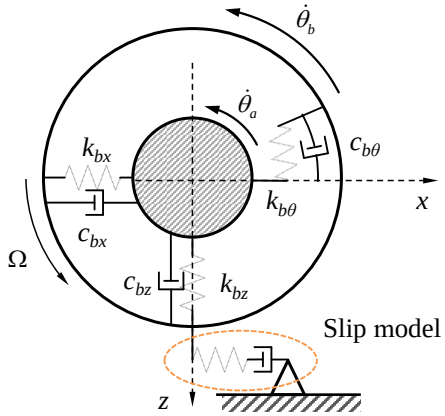

Figure 3.4: Rigid ring model with a 3-DOF spring and damping element.

represented as

$$m_b\ddot{x}_b + c_{bx}\left(\dot{x}_b - \dot{x}_a\right) + k_{bx}\left(x_b - x_a\right) - c_{bx}\left(\Omega + \dot{\theta}_a\right)\left(z_b - z_a\right) = F_{cx}, \tag{3.110}$$

$$m_b\ddot{z}_b + c_{bz}\left(\dot{z}_b - \dot{z}_a\right) + k_{bz}\left(z_b - z_a\right) - c_{bz}\left(\Omega + \dot{\theta}_a\right)\left(x_b - x_a\right) = F_{cz}, \tag{3.111}$$

$$I_{by}\ddot{\theta}_b + c_{b\theta}\left(\dot{\theta}_b - \dot{\theta}_a\right) + k_{b\theta}\left(\theta_b - \theta_a\right) = M_{by} + F_{cx}R_e, \tag{3.112}$$

$$m_a\ddot{z}_a + c_{bz}\left(\dot{z}_a - \dot{z}_b\right) + k_{bz}\left(z_a - z_b\right) - c_{bz}\left(\Omega + \dot{\theta}_a\right)\left(x_a - x_b\right) = F_{z0}, \tag{3.113}$$

$$I_{ay}\ddot{\theta}_a + c_{b\theta}\left(\dot{\theta}_a - \dot{\theta}_b\right) + k_{b\theta}\left(\theta_a - \theta_b\right) = M_{ay}, \tag{3.114}$$

in which m_a and m_b are the mass of the rim and the rigid ring, respectively, I_{ay} and I_{by} represent the moment of inertia of the rim and the rigid ring respectively, k_{bx}, k_{bz}, and $k_{b\theta}$ indicate the longitudinal, vertical, and torsional equivalent stiffness of the sidewall, respectively, c_{bx}, c_{bz}, and $c_{b\theta}$ denote the longitudinal, vertical, and torsional damping coefficients of the sidewall, F_{cx} and F_{cz} are the longitudinal and vertical contact forces, F_{z0} is the vertical load of the tire, and M_{ay} and M_{by} represent the torques acting on the rim and the rigid ring, respectively. The determination of the parameters of the 3-DOF spring is the core to achieving a reasonable analysis of the dynamic response. Elastic characteristics can be identified by the results of the 1st-order modes from modal tests or over-cleat tests, the determination of which is discussed in the following section.

3.2.4 Coupled rigid-flexible ring model

Because of the theoretical shortcomings of rigid ring models in the representation of the tire-road contact mechanism, a coupled relationship between the flexible and rigid rings, i.e., using the coupled rigid-flexible ring model to estimate the dynamic response of tires, is established in this section. The flexible ring in this model is introduced to estimate the steady-state deformation and

contact forces of the tire. The transient dynamic response can be analyzed by the rigid ring. Fig. 3.5 illustrates the fundamental structure of the coupling model adopted for this study.

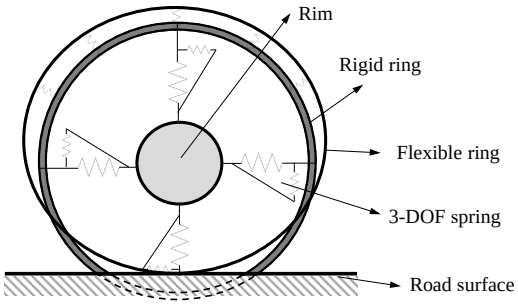

Figure 3.5: The coupled rigid-flexible ring model.

The equations of the rigid ring and the flexible ring are integrated to establish the complete computational model. The contact force obtained from the local deformations in the flexible ring model is considered as the rigid ring excitation. Once the velocity and the coordinates of the rigid ring are identified by dynamic analysis, the simulation time is frozen and the overall displacements are updated. And later, the local deformations and the contact forces are statically calculated at the beginning of the next time step. The calculation procedure is executed until all iterations of the time step are finished. The complete simulation flow chart is shown in Fig. 3.6.

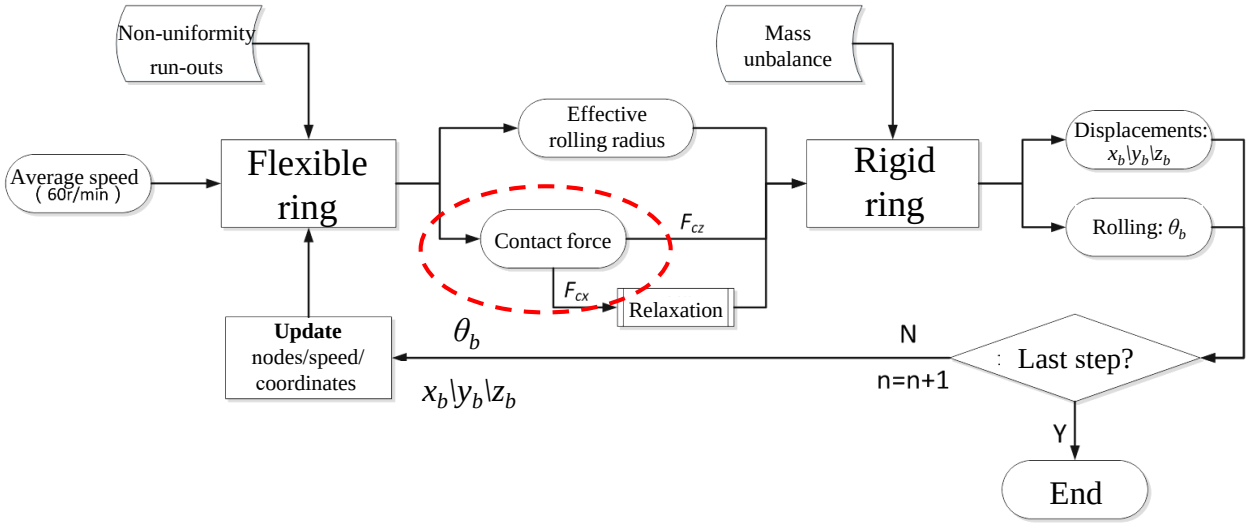

Figure 3.6: Flow chart of the simulation based on the coupled rigid-flexible ring model.

3.3 Model parameters

The parameters of the coupled rigid-flexible ring model consist of geometric and physical parameters. Some geometric parameters can be directly obtained from the design parameters or FE models. Hence, the identification of the physical parameters will be the decisive part of the accuracy of the developed simulation method. In this part, the identification method of the physical parameters is first discussed, and then the genetic algorithm (GA) optimization method is selected to determine part of the model parameters for different simulation scenarios (see Fig. 3.7). This section shows an example of a low-speed uniformity test and provides a standard process for optimizing the parameters of a tire with a non-ideal structure in an attempt to make the simulated radial force variation (RFV) coincide with those measured on the low-speed uniformity test rig. This optimization procedure for model parameters is very readily transferable to a more diverse range of measurement types and application scenarios.

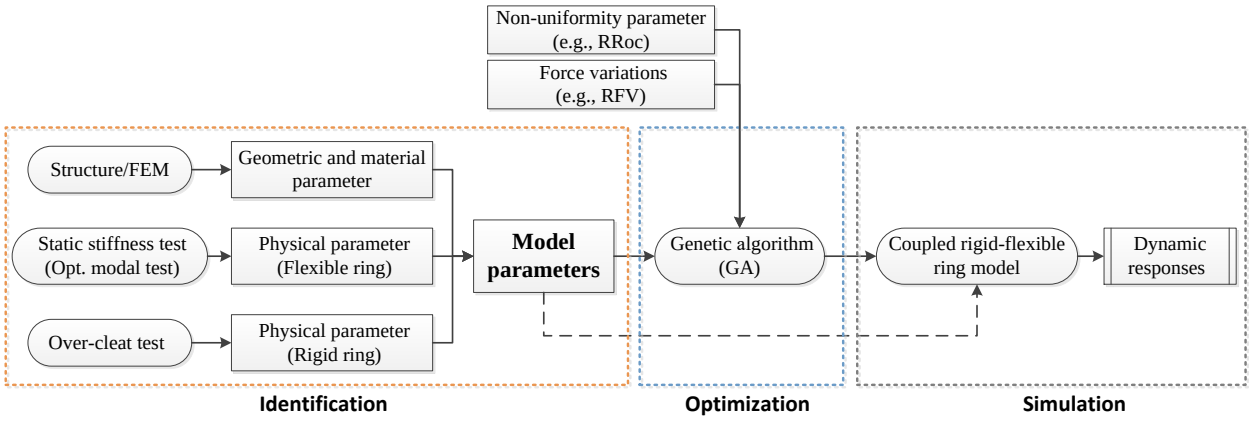

Figure 3.7: Flow chart of the identification and optimization process in the coupled rigid-flexible ring model.

3.3.1 Identification of physical parameters

The physical parameters can be naturally divided into two parts:

1. the parameters of the flexible ring model, which mainly include the stiffness of the flexible ring, the equivalent stiffness and damping coefficients of the sidewall, and the contact stiffness of the tread rubber;

2. the parameters of the rigid ring model, which mainly include the mass and moment of inertia of the rigid ring and the equivalent dynamic stiffness and damping coefficients of the sidewall.

In the proposed coupled flexible-rigid ring model, the accuracy of the contact algorithm will determine the precision of the overall simulated results. Considering that the contact model in the flexible ring model is established on the basis of steady-state deformation of the belt, the radial stiffness data obtained from the tire static stiffness measurements have been used to estimate the parameters of the flexible ring model. The nonlinear least-squares method is adopted in this section to achieve the aim that the simulated results of static stiffness are as close as possible to the test data. The initial setting of the parameters is referred to as the method of identifying the flexible ring model using tire modal analysis presented in the literature [32, 123], so as to realize the determination of the original parameter range.

For those parameters in the rigid ring model, the equivalent stiffness and damping coefficients can be determined from modal tests or an over-cleat test [126]. However, the diverse identification methods lead to different identified results. It is found that the 1^{st}-order natural frequencies acquired from the over-cleat tests are slightly lower than those identified by a modal test [14, 126, 127]. One of the reasons for the disagreement is that the setups of the boundary conditions are different, i.e., the modal test is conducted with unloaded conditions to simulate the free vibration, but the contact and rolling effect is inevitably introduced into the over-cleat test. Another possible explanation is that the strain hardening effect occurs when the tread rubber is in contact with the road surface during rolling, while it does not exist in the modal test. In fact, the two distinct sets of stiffness parameters for the flexible and rigid rings reflect the difference in the physical meaning of tire dynamic and static stiffness.

3.3.2 Optimization of physical parameters using GA

Due to the complex manufacturing process, there are inevitable imperfections in the structure and material distribution of tires, which are generally known as tire uniformity. These defects can directly affect the test results of the tire and thereby introduce errors into the model parameters. Thus, a method for the optimization of model parameters for tires with structural or dimensional defects is proposed in this section. To illustrate the optimization process, an example of the optimization of model parameters is introduced here, in terms of geometric defects of the tire and low-speed uniformity analysis. For the measured tire, the radial run-out (RRo) is an additional input to the model, and the RFV is the corresponding outcome. They can both be readily accessed on the uniformity test machine.

It is well known that optimization problems require an objective function to be defined. For the uniformity analysis of tires, one attempt is to optimize the physical parameters so that the simulated

RFV corresponds with the measured results on the test rig. Considering the good performance of multi-variable optimization design, GAs become an applicable tool for the effective identification of physical parameters [74, 128]. In this study, consequently, RFV is chosen as the performance index of the algorithm, and a GA is used to determine the physical parameters of the specific tire mentioned above.

In order to run the optimization algorithm based on the proposed tire model, the GA first randomly generates an initial population within a user-defined range of variables, which is determined by the initial physical parameters given in the previous section. Each set of variables, i.e., an individual, is substituted into the equations of motion of the tire, which is also later on used to calculate the RFV which constitutes the evaluation function prescribed in the GA. Then, the value of the fitness function for each individual in the current generation is calculated based on how well the numerical results matched the measurement data. In this work, the deviation between the experimental and simulated RFV results is adopted to evaluate the fitness value, i.e.,

$$f_d(\mathbf{x}) = \left\| \mathbf{F}_{z,\mathrm{exp}} - \mathbf{F}_{z,\mathrm{sim}} \right\|_2, \tag{3.115}$$

where $\mathbf{x}$ is the vector of the variables to be optimized, $f_d(\mathbf{x})$ denotes the objective function in the GA, $\mathbf{F}_{z,\mathrm{exp}}$ and $\mathbf{F}_{z,\mathrm{sim}}$ are the measured and simulated RFVs, respectively. $\|\cdot\|_2$ means the 2-norm of the vector. However, the inherent function of the GA is to maximize the value of the fitness function, therefore, the actual objective function applied in the algorithm $f(\mathbf{x})$ is

$$f(\mathbf{x}) = \frac{1}{f_d(\mathbf{x})} = \frac{1}{\left\| \mathbf{F}_{z,\mathrm{exp}} - \mathbf{F}_{z,\mathrm{sim}} \right\|_2}, \tag{3.116}$$

which suggests that maximizing this fitness function will minimize the error between the test data and the modeled results. In the iterative process, each individual in a given generation, i.e., a set of model parameters, is firstly evaluated by the fitness function. When these individuals are assessed by a probabilistic selection function [128], some of them are chosen to either directly pass to the next generation or perform crossover and mutation to create new individuals, resulting in a new generation. In each generation, this procedure is executed repeatedly until the given maximum number of generations is achieved. Eventually, the physical parameters of the model are determined.

3.4 Numerical results of the dynamic responses

To validate the presented model, a specific radial tire for passenger cars is simulated and evaluated in this section. As an application of the model to a practical structure, the dynamic analysis of a 205/55R16 radial tire is conducted. Based on the above-mentioned model and the identification method of the model parameters, the model parameters are determined and the steady-state contact forces and the dynamic responses of the objective tire are subsequently calculated. Furthermore, the accuracy of the contact algorithm and the dynamic analysis is verified by the static radial stiffness measurements and the over-cleat tests. The investigated tires and their measurements discussed in this section were provided by the Shandong Linglong Tire Co.,Ltd.

3.4.1 Model parameter identification and experimental system implementation

In this subsection, according to the parameter identification method proposed above, the identification algorithm of the physical parameters in this established model is an implementation of a two-step process. The physical parameters of the flexible ring model are first estimated using the radial stiffness measurement. And then those of the rigid ring model are estimated by conducting the over-cleat tests. For the specific modeled tire, the designed structural and geometric parameters are listed in Table 3.1. These parameters can be obtained directly from dimensional measurements or FE models.

Table 3.1: Geometric and material parameters of a 205/55R16 tire.

Parameter type	Unit	Value
Ring effective width b	m	0.172
Ring thickness h	m	0.018
Effective density ρ	kg/m^3	1.60×10^3
Mean radius R	m	0.32
Initial pressure p_0	Pa	2.1×10^5

Parameters of the flexible ring model

First, the experimental results of the radial tire stiffness are obtained by conducting the static stiffness measurements, which have been used for identifying the physical parameters in the flexible ring model. The measurement was performed to obtain the stiffness of the tire using the Stiffness Test Machine, manufactured by TS TestingService GmbH, in Shandong Linglong Tire Co., Ltd. The system implementation of the measurement is shown in Fig. 3.8(a). The forces applied to the tire and its displacements are measured by the force and displacement sensors on the test rig. The tire pressure needs to be adjusted to the nominal inflation pressure of 0.22MPa and set at room temperature (22.6°C) for 24h before assembling on the test rig. The test loads are set to 3077N, 5128N, and 7179N. Thereafter, the radial load was applied to the tire to 80% of its test load at a radial loading speed of 50mm/min. When the loading was completed, it was held for 5s and repeated 3 times. Before each loading process, the tire inflation should be adjusted to the nominal value. The radial force is then loaded to 50% of the test load at a radial loading speed of 50mm/min and maintained for 1min before being unloaded. Finally, the loading procedure is repeated once to 80% of the test load of the tire. The radial stiffness is defined from the radial deformation characteristic by using a computational relationship, which is determined by points corresponding to 50% and 80% of the test load. The radial stiffness under each test load is calculated by the following equation,

$$k_r = \frac{F_{r,80\%} - F_{r,50\%}}{d_{r,80\%} - d_{r,50\%}}, \tag{3.117}$$

where k_r means the radial stiffness of the tire, $F_{r,80\%}$ and $F_{r,50\%}$ respectively denote the vertical forces for 80% and 50% of the test load, and $d_{r,80\%}$ and $d_{r,50\%}$ respectively represent the displacements corresponding to 80% and 50% of the test load. The test data are presented in Table 3.2. It is found that the radial stiffness of the tire grows with the increase of the load.

Utilizing the measured data for the radial stiffness, the parameters of the flexible ring model were estimated by combining the determination method of the initial input of the parameters based on the authors' previous work [32] and the nonlinear least-squares method, which led to the minimum error between the simulated and the test results of the radial stiffness. The identified parameters of the flexible ring are listed in Table 3.3 (Identified Value). The radial stiffness calculated from the identified parameters is shown in Table 3.2, and the comparison between the simulated and measured force-displacement curves is illustrated in Fig. 3.8(b).

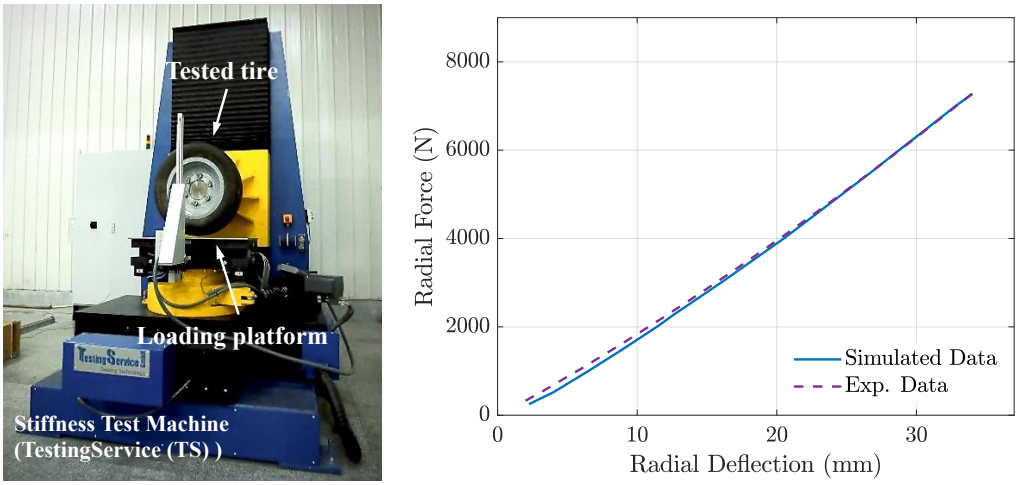

(a) System implementation of the stiffness test machine with a measured tire.

(b) The comparison of the simulated relationship between the radial deflection and force using the identified parameters of Table 3.3 with the measurement results.

Figure 3.8: Setup of the radial stiffness measurement.

Parameters of the rigid ring model

For the determination of the parameters of the rigid ring, we have used the data provided by Shandong Linglong Tire Co., Ltd in this thesis, which was obtained from the HSU5.3 Tire High-speed Test System produced by ZF Friedrichshafen AG. The experimental equipment is depicted in Fig. 3.9(a). It mainly consists of a mechanical motion system, a computer control interface, and a data acquisition system, where the diameter of the drum is 2m. The measured tire is restrained by the rim. During the measurement, the position of the wheel center is fixed and the tire is driven by the rotation of the drum. The tire is rolled over a cleat at a predetermined speed, and the dynamic responses are monitored in real-time by a force sensor mounted at the center of the rim. The cleat is rectangular with a dimension of 10mm$\times$20mm (height$\times$width), which is mounted on the drum surface at an angle of 90°. Three vertical loads were selected for the testing conditions, which were 0.4, 0.8, and 1.2 times the load index (LI), i.e., 2471N, 4942N, and 7414N, and implemented at velocities of 30km/h, 60km/h, and 90km/h, respectively. Once the tire reaches a stabilized position, the speed of the drum slowly increases to the test speed. At this moment, the data acquisition system collects the response of each impact and then stores it.

The nonlinear least-squares method is selected for the identification algorithm of the parameters of the rigid ring. The fundamental concept is the minimization of the error between the simulation results and the test data of the dynamic properties under the operating condition. The test setup is input into the rigid-flexible ring model for simulation, the simulated longitudinal and vertical forces at the wheel center are obtained and the error is evaluated. The time step of the simulation

Table 3.2: Measurement results of the radial stiffness of the 205/55R16 tire.

Radial force (N)	3077		5128		7179	
	Test	Simulated	Test	Simulated	Test	Simulated
Radial deflection corresponding to 50% radial force (mm)	9.58	8.50	14.59	13.56	19.41	18.36
Radial deflection corresponding to 80% radial force (mm)	14.33	13.07	21.67	20.67	28.75	27.73
Radial stiffness (N/mm)	194.33	202.11	217.30	216.36	230.60	229.73

is consistent with the sampling interval of the measurement, which means that the data length of the simulated result in one period is equal to the data length of the measured result. If the accuracy requirement is not fulfilled, the parameters in the model are modified until the deviation with the experimental data is within the tolerance range of the accuracy requirement. Here, the objective function of the minimization is denoted as

$$\min \left[\sum \left[w_1 (F_{zc} - F_{zm})^2 + w_2 (F_{xc} - F_{xm})^2 \right] \right], \tag{3.118}$$

where F_{zm}, F_{zc} respectively denote the measured and calculated vertical forces, F_{xm}, F_{xc} respectively represent the measured and calculated longitudinal forces, and w_1, w_2 are the weight factors. Herein, the values of w_1 and w_2 are both taken as 1. In this section, the performance at 30km/h under 0.4LI vertical load is adopted to recognize the parameters, and those results under other operating conditions are taken as the verification of the model (cf. Section 3.4.3). The comparison between the simulation and experimental results for this operating condition is provided in Fig. 3.9(b), and the corresponding parameters are indicated in Table 3.4 (Identified Value).

3.4.2 Contact forces distribution

In the developed rigid-flexible coupled ring model, contact forces are the primary parameters that combine the flexible and rigid ring models. Therefore, the accuracy of the algorithm to characterize the tire-road contact mechanism becomes the key point of the entire theoretical model. In this subsection, the results of the steady-state contact forces on a flat road surface are discussed first.

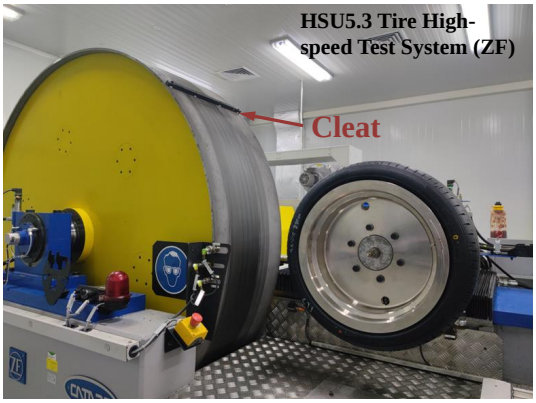

(a) System implementation of the over-cleat test.

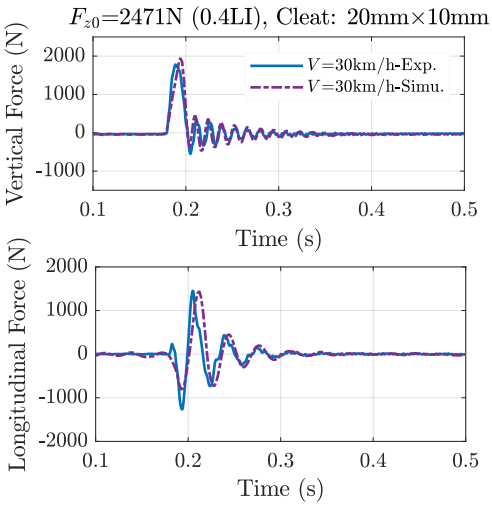

(b) Simulated and measured time traces of vertical force and horizontal longitudinal force for the tire running at a given speed of 30km/h and an initial vertical load of 0.4LI over the cleat at constant axle height using the identified parameters in Table 3.4.

Figure 3.9: Rolling over a rectangular cleat.

Convergence of contact algorithm

On the basis of the steady-state contact algorithm for the flexible ring, the distribution of contact forces is calculated by assuming that the road surface is ideally flat and the geometric uniformity of the tire is not considered. The flexible ring is discretized to provide a fast solution for the steady-state displacements and the distribution of contact forces. In Fig. 3.8, the comparison of the static radial stiffness between the experimental data and the simulated results indicates that the flexible ring model can appropriately represent the physical characteristics of the tire at steady-state contact. Thus, in this section, the convergence analysis of the contact forces is discussed. The simulation results of the vertical contact force for the different number of nodes are presented in Fig. 3.10. The flexible ring model can achieve good convergence under different vertical displacements (10mm, 15mm, 20mm). Considering the computational efficiency of the model, the number of discrete nodes selected is 360 in this work.

Steady-state contact forces

The results of the normal and shear pressure distributions under different vertical loads in the contact patch are shown in Fig. 3.11. It is seen that the properties of the contact force under different vertical

Table 3.3: Physical parameters of the flexible ring.

Parameter type	Unit	Identified Value
In-plane bending stiffness EI	Nm^2	2.10
Radial stiffness of the sidewall k_u	N/m^2	4.54×10^5
Circumferential stiffness of the sidewall k_v	N/m^2	1.77×10^5
Radial damping coefficient of the sidewall c_u	Ns/m^2	222.47
Circumferential damping coefficient of the sidewall c_v	Ns/m^2	218.13
Undeformed thickness of tread rubber h_0	m	0.0125
Normal stiffness of tread rubber k_{Es}	N/m	4.63×10^5
Tangential stiffness of tread rubber k_{Gs}	N/m	3.60×10^5

loads can be well reflected by the contact algorithm based on the flexible ring model. Under the smaller vertical loads, the contact pressure of the tire shows a convex and parabola-like distribution; when the vertical load gradually increases, the curve tends to become saddle-shaped, which means that the central part of the treadband in the contact area tends to buckle. This is an essential property of the structure of a tire with high circumferential stiffness. A reasonable physical model should be able to reflect this tendency properly. This phenomenon is in general agreement with the trend reported in experimental studies [44, 120, 129, 130] Meanwhile, it demonstrates the theoretical basis and rationality of the flexible ring model as an approximation for the steady-state deformation and tire-road contact.

An advantage of the proposed model over the classic rigid ring model is that the flexible ring can be utilized to calculate the steady-state contact forces. Therefore, this established model can be utilized to simulate the contact behavior of tires on an uneven road surface. Owing to the unevenness of the pavement, an additional algorithm typically has to be involved in the rigid ring model to evaluate the tire motion [13]. In contrast, the derivation of the contact forces in the flexible ring model requires a more complex computational approach for the solution of partial differential equations. However, reasonable computational costs can be generated by the linearization assumptions adopted in the contact algorithm developed in the previous section. Moreover, the flexible ring model can be applied to analyze the tire response caused by cleats or potholes, and even extended to estimate the handling dynamics on uneven roads. Hence, the simulated results of the contact deformation when the tire is rolling over a cleat are given here to illustrate the possibility of using the proposed

Table 3.4: Physical parameters of the rigid ring.

Parameter type	Unit	Identified Value
Mass of the rim m_a	kg	7.80
Mass of the rigid ring m_b	kg	6.90
Moment of inertia of the rim I_{ay}	kg·m^2	0.455
Moment of inertia of the rim I_{by}	kg·m^2	0.643
Longitudinal stiffness of the spring k_{bx}	N/m	2.76×10^5
Vertical stiffness of the spring k_{bz}	N/m	1.19×10^6
Torsional stiffness of the spring $k_{b\theta}$	N/rad	8.27×10^5
Longitudinal damping coefficient c_{bx}	Ns/m	4.03×10^2
Vertical damping coefficient c_{bz}	Ns/m	4.38×10^2
Torsional damping coefficient $c_{b\theta}$	Ns/rad	2.18×10^2

contact algorithm for simulations on uneven road surfaces. Fig. 3.12(a) presents the displacements and the deformation of the tire as it moves over the profile of the cleat. Fig. 3.12(b) exhibits the deformation curve of the belt when the tire is just rolling on the cleat.

3.4.3 Simulations and experimental evidence when rolling over a cleat

As stated in Section 3.4.1, Shandong Linglong Tire Co., Ltd provided a large amount of test data from measurements carried out on a drum test rig (Fig. 3.8(a)). The over-cleat tests were conducted under vertical loads of 0.4LI, 0.8LI, and 1.2LI at speeds of 30km/h, 60km/h, and 90km/h. The specific experimental setup and the testing conditions were given in detail in Section 3.4.1. This section performs the evaluation using the established coupled rigid-flexible ring model.

Fig. 3.13-3.15 demonstrate the application when the tested tire rolled over the same rectangular cleat with different loads. The computed vertical and longitudinal forces seem to capture the measured properties accurately for different vertical loads until the frequency is about 120Hz or higher. It reveals a reasonable level of agreement. As seen in the figures, the impact of the cleat can be considered to be an impulsive excitation at a light load, when the vertical response of the tire primarily depends on the vertical vibration mode. But as the vertical load increases, the vertical forces at the wheel center exhibit two peaks with almost the same magnitude. The reason is that the

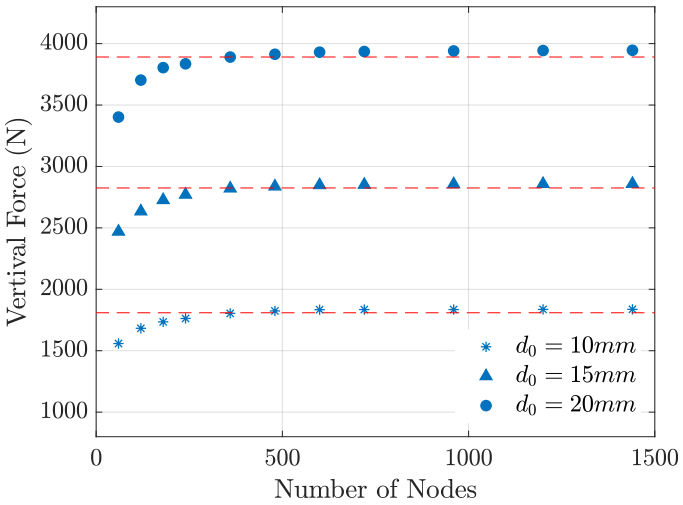

Figure 3.10: Convergence analysis of the vertical contact force and the number of nodes.

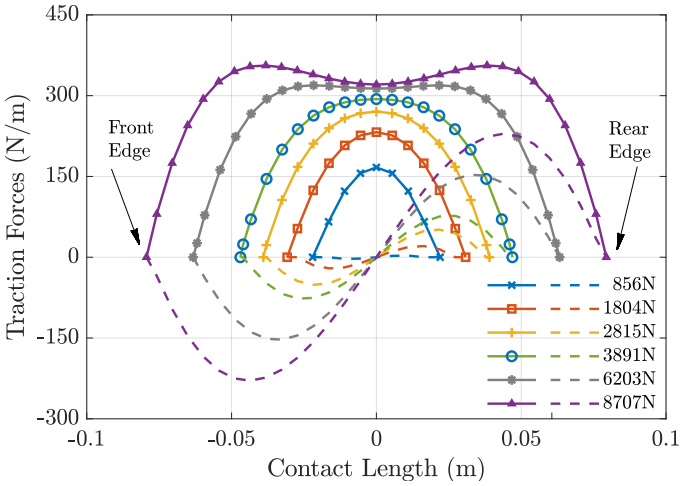

Figure 3.11: The distributions of normal pressure (solid line) and shear pressure (dashed line) under different vertical loads.

vertical force responses are the result of a combination of the enveloping characteristics and the vertical vibration mode of the tire. (The first natural frequency of a vertical mode of the rigid ring is about 92Hz).

Fig. 3.13, 3.16, and 3.17 illustrate the results of measurements and the simulations of with different speeds over the same cleat in both the time and frequency domains, while the position of the axes is kept constant. The time-domain responses of the vertical and longitudinal forces have been indicated and the amplitude spectra of these quantities are presented. The simulated results show good agreement for the vertical force at operating speeds in the measurements. The spectrum shows that the natural frequency of the first vertical mode corresponding to the tested tire is approximately 92Hz, matching the results from the modal test. At lower speeds, the vertical responses are mainly

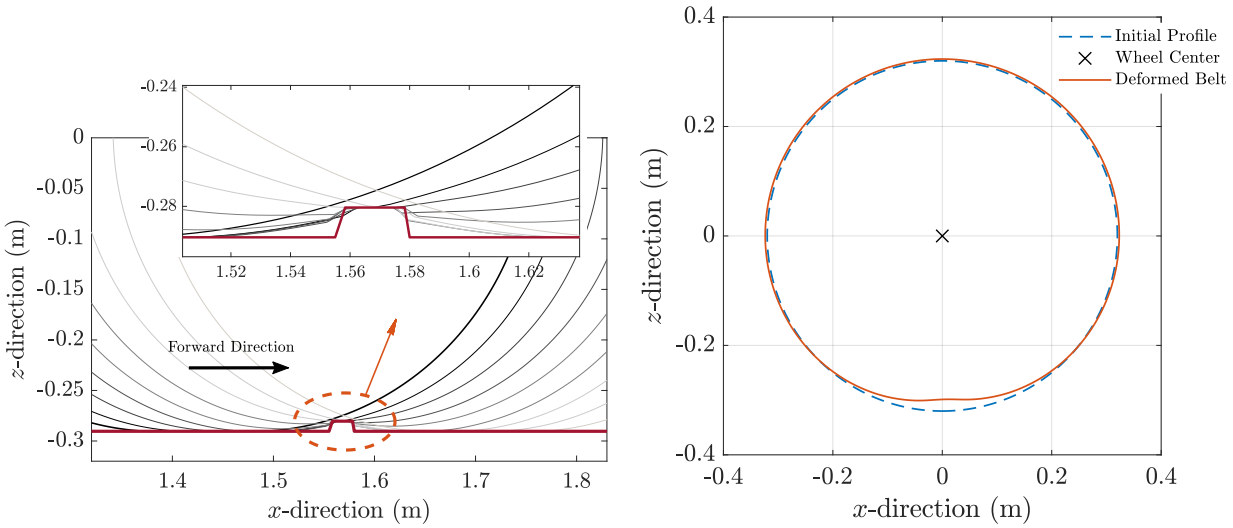

(a) Profile curves of the treadband surface while rolling over a 10mm*20mm rectangular cleat (each 2 time steps).

(b) Deformation curve of the belt when the tire is just rolling on the cleat.

Figure 3.12: Tire deformation when rolling over a cleat.

affected by the envelope characteristics, at which time the vertical vibration mode of the tire is not completely activated. While at higher speeds the vertical force responses of tires rolling over a rectangular cleat mainly depend on the vertical vibration mode, which can be excited by the cleat. In the amplitude spectra at different speeds, it is found that the natural frequency of the first vertical mode is not a constant value, which tends to decrease slightly with an increase in speed. It can be interpreted as possibly associated with the reduction of the dynamic stiffness at different speeds or the Doppler effect [127]. In this case, the stiffness parameters in this model are taken as constant values. It leads to small deviations in the prediction of the responses at different speeds. It is an inherent limitation of using the rigid ring model for dynamics simulation.

It is observed that the amplitude spectrum of the longitudinal forces has a peak at 29Hz. This phenomenon arises due to the 0^{th}-order modes in the rotation of the tire and the connected rim. The 1^{st}-order rotational mode (92Hz) appears when the speed reaches 60km/h. In the measurements of the longitudinal forces at 60km/h and 90km/h (Fig. 3.18(a)), the 1^{st}-order rotational mode is stimulated, which is the predominant frequency component. But it is not as obvious in the simulated results as it is in the tested data. The response of the longitudinal force is not effectively excited by the rotating vibration in the dynamics computation. Considering this in the rigid ring model, the motion of the belt is estimated by only considering the forces induced by the 0^{th}-order and 1^{st}-order vibration modes. It means that the belt always keeps a circular shape. This assumption may cause the identified rotational stiffness to be larger, which is obtained using only the measured responses at 30km/h, thus failing to stimulate the 1^{st}-order rotational mode. In future implementations, the

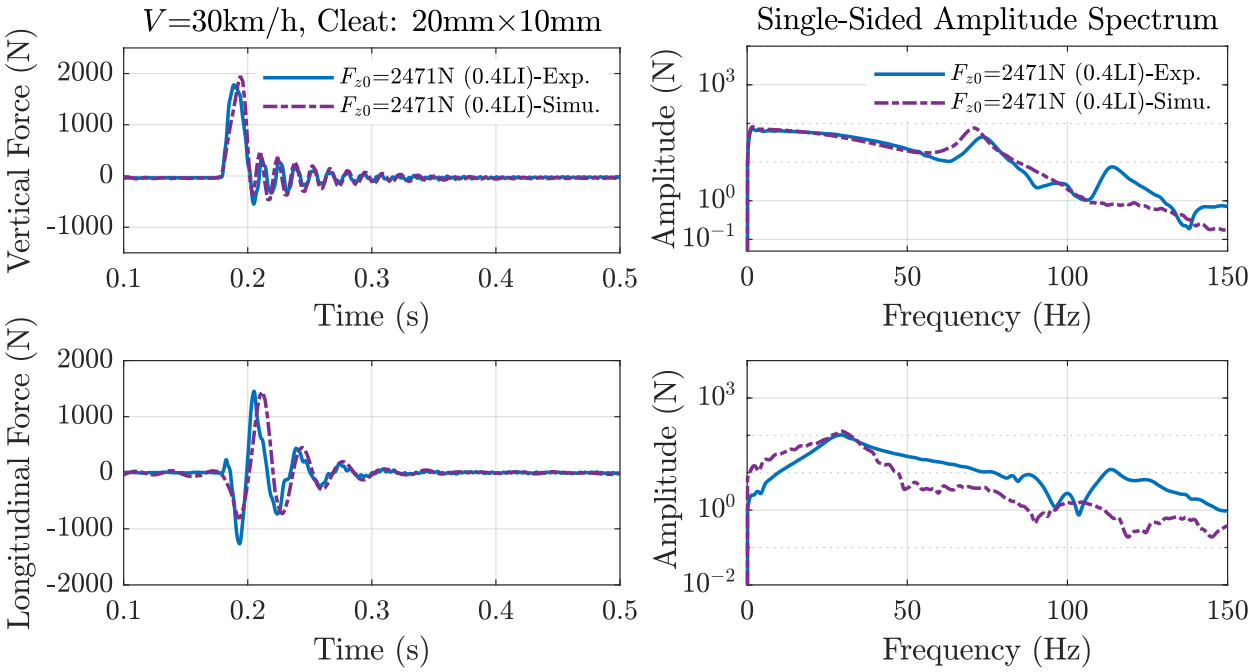

Figure 3.13: Time traces and amplitude spectra of the vertical force and longitudinal force for the tire operating at a vertical load of 0.4LI (2471N) and a testing speed of 30km/h. The cleat shape is a 10mm×20mm (height×width) rectangular. (Solid line: measurement data; dashed line: calculated results of the proposed model).

model parameters can be considered to be identified by different speed ranges according to the operating conditions to be discussed.

The performance of the model contributed in this chapter is considered to be in between that of the rigid and flexible ring models. These existing models include different analysis processes for transient dynamics, contact algorithms, and friction models, so their accuracy is slightly different. In the previous studies, the simulation results for the condition of a tire rolling over a cleat have been given by applying SWIFT [13] and FTire [131, 132]. The results of this section can be analyzed in a similar frequency range and accuracy as SWIFT. However, for the prediction of longitudinal forces at high speeds, FTire has a broader analytical range and greater precision. This is achieved by considering the 1st-order radial mode of the tires in FTire.

With regard to the computational cost of this established model, the average CPU time is approximately 20 to 40 times that of the real-time condition. It relies on the number of discrete elements set in the flexible ring model and the current scenario of simulation (cf. Fig. 3.19). The total simulation time is clearly close to FTire, but it takes longer than SWIFT. The simulation part of the transient dynamics in the developed model is similar to the rigid ring model, which is much more simplified than directly solving the dynamic problem using a flexible ring, but the contact part is obviously

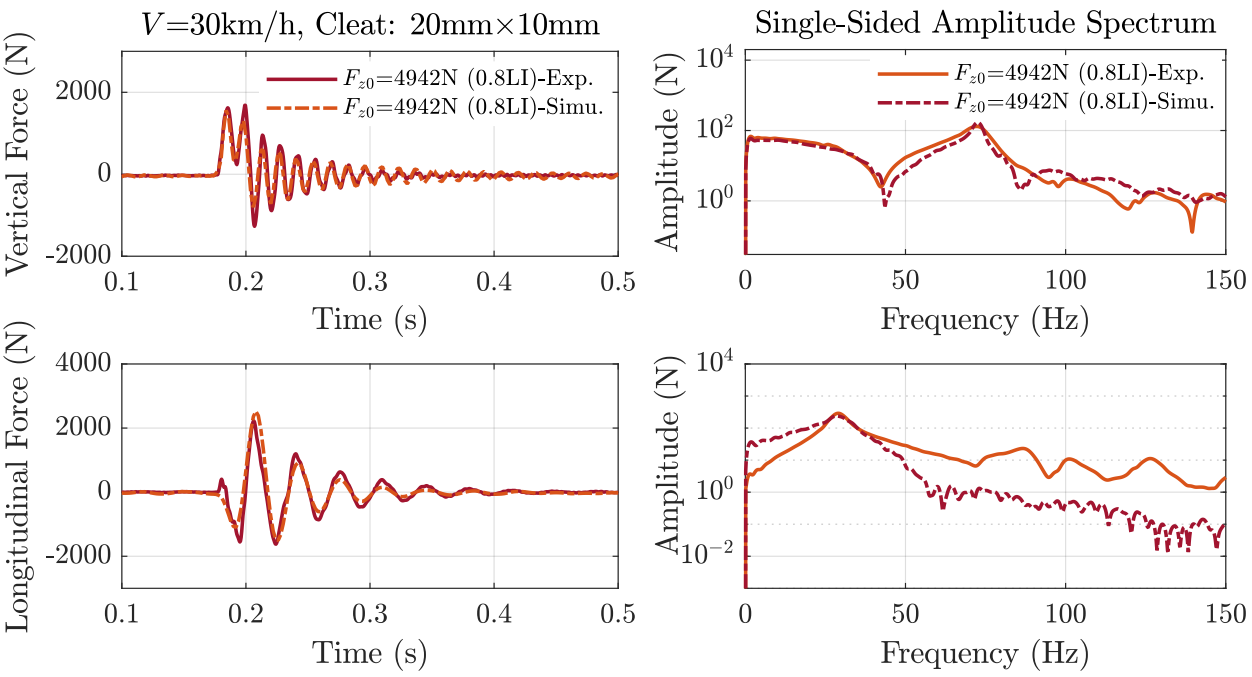

Figure 3.14: Same as Fig. 3.13 but at a different initial vertical load, 0.8LI (4942N).

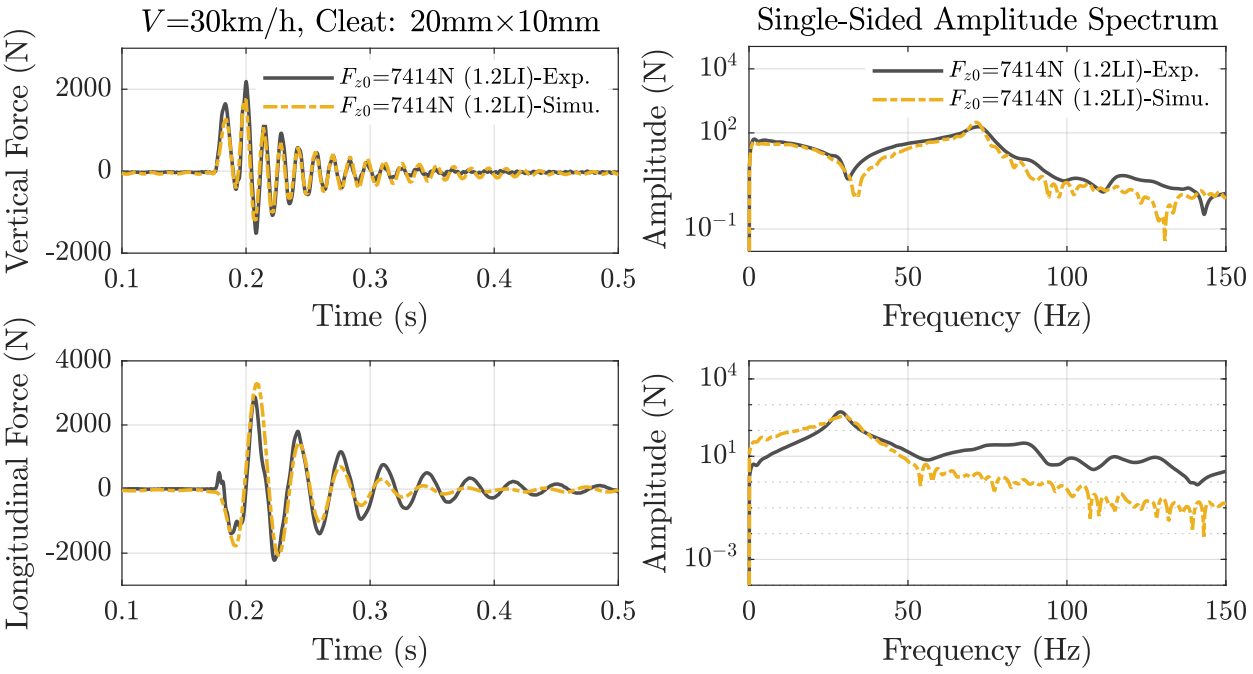

Figure 3.15: Same as Fig. 3.13 but at a different initial vertical load, 1.2LI (7414N).

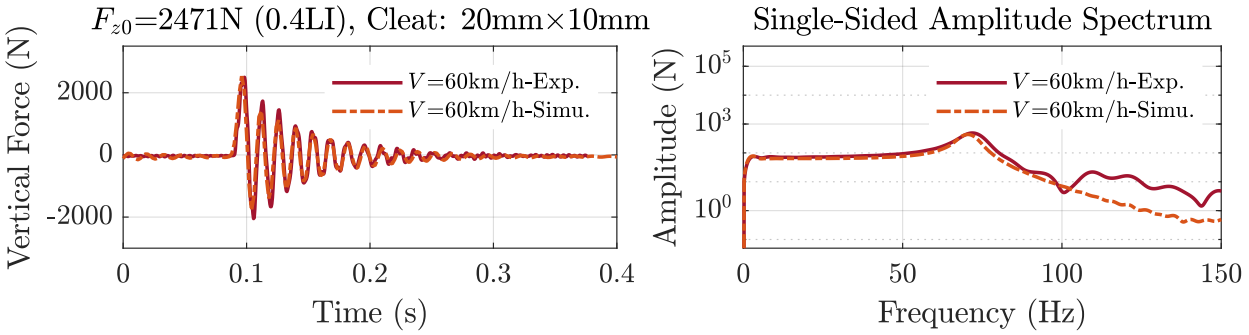

Figure 3.16: Same as Fig. 3.13 but at a different speed, 60km/h.

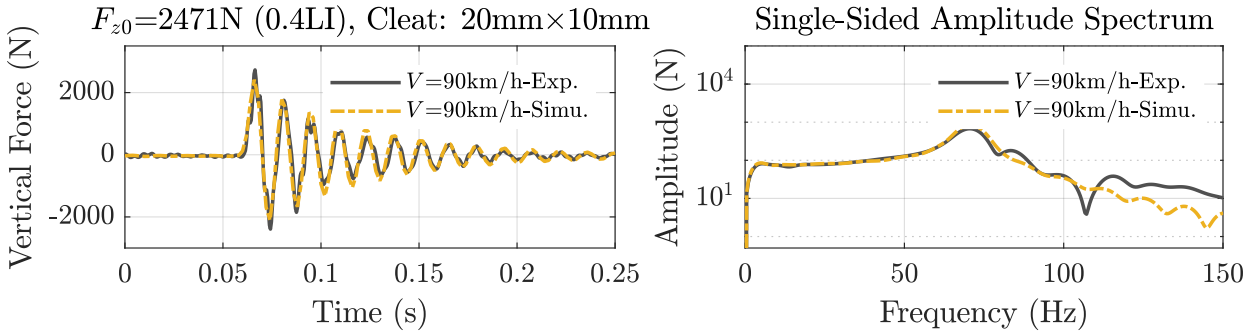

Figure 3.17: Same as Fig. 3.13 but at a different speed, 90km/h.

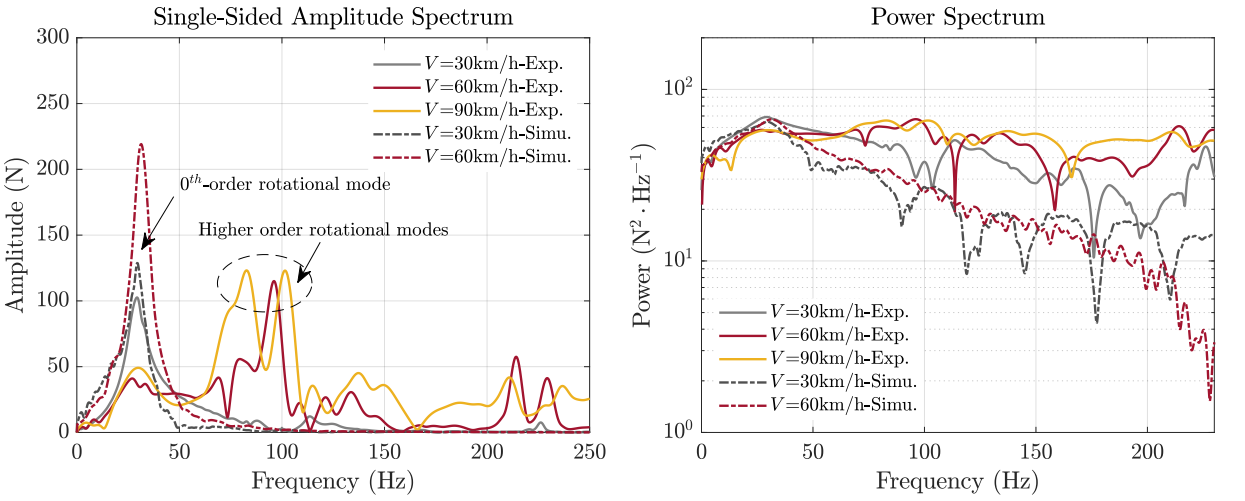

(a) Single-sided amplitude spectrum.

(b) Power spectrum.

Figure 3.18: Amplitude and power spectra of the longitudinal forces at different speeds (30km/h, 60km/h, and 90km/h).

more complex than the single-point contact algorithm. The efficiency of different tire models can not be compared straightforwardly, since the current algorithm is only a theoretical prototype and it has not yet been combined through an interface with the multibody simulation software of whole vehicles, such as CarSim or ADAMS. Nevertheless, the computational cost can be reduced by a thorough optimization of the algorithm in the future.

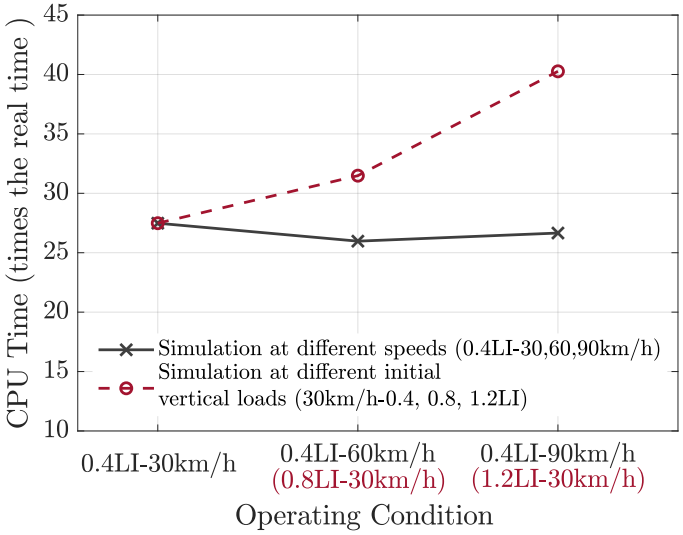

Figure 3.19: The multiplier of CPU time to the real time for different operating conditions

3.5 Summary

In this chapter, a theoretical model has been developed to evaluate the characteristics of the in-plane dynamic responses of tires and analyze the transient responses at the spindle on the uneven road surface. A contact algorithm based on the 2D flexible ring provides a pressure distribution on the tire-road contact patch and the length of the footprint under different vertical loads. The transient dynamic response is then estimated by combining the rigid ring model with the flexible ring model. Further, the identification of model parameters based on the static stiffness measurements and the over-cleat test, and the optimization approach have been given. The accuracy of the contact algorithm and the transient responses are validated by experimental data.

A novel coupled rigid-flexible ring model has been presented to analyze the characteristics of the dynamic responses of tires. The contact algorithm based on the 2D flexible ring provides the analysis of the pressure distribution in the tire-road contact area under different vertical loads. The comparison of the static radial stiffness between the experimental data and the simulated

results has been shown. The contact pressure distribution indicates that the contact model can appropriately represent the physical characteristics of the tire at steady-state contact. It demonstrates the theoretical basis and rationality of the flexible ring model as an approximation for the steady-state deformation and tire-road contact. The applicability of the model in the simulation of transient response has been validated by the experimental data of over-cleat tests at different speeds and different vertical loads. In this way, the proposed new method has the merits of both high accuracy up to 150Hz and low computing cost.

For the dynamic analysis of tires, the accuracy of the identification of the physical parameters directly affects the simulated results. So the nonlinear least-squares method has been adopted to determine the physical parameters of a specific tire in this work, and a set of measured data of the static stiffness and the over-cleat responses has been chosen as the performance index of the identification algorithm. It is clear that this approach yields an effective simulation in terms of parameter determination.

Chapter 4

Analysis of Low-speed Uniformity of Tires

Up to this point, the theoretical modeling based on the coupled rigid-flexible ring model and its experimental validation has been completely described. However, this tire dynamics model should not be limited to this area, as its application can be introduced to more scenarios. Taking into account the inevitable dimensional deviations and the material non-uniformity in the tire manufacturing process, this section analyzes the transfer characteristics of the tire with geometric defects at low speeds. This analysis corresponds to the testing condition of the low-speed uniformity measurements in the tire manufacturing process. Since the focus of this work is on the derivation of an innovative theoretical model, not on uniformity analysis, this section does not analyze the properties of the high-speed uniformity, which can be further extended in subsequent studies. The purpose of this section is to illustrate the greater applicability and functional expansion possibilities of the proposed model in the analysis of tire uniformity simulation.

4.1 System implementation of low-speed uniformity measurements

Uniformity test machines are one of the most common devices for detecting the level of uniformity in tires at present. Tire uniformity measurements are performed by assessing the variations of the tire forces during rotational motion. The tire is mounted on the spindle of the test machine, and during the measuring process the spindle and the drum are kept stationary by mechanical supports, and the axes are positioned parallel to each other. The drum is equivalent to the road surface, and it applies a load to the tire that corresponds to the contact forces exerted by the ground during the movement. The vibration of the tire is transmitted to the drum and is delivered to a multi-phase

force sensor fixed on the drum, which can respectively collect the periodic variations of radial, transitional, and lateral forces, and subsequently calculate the conicity (CON) and ply steer (PLY) of the objective tire.

This test is based on the High-Speed Uniformity Test Machine from TS TestingService GmbH (Fig. 4.1). The tire is mounted on the test rim in accordance with the requirements of the equipment and inflated to an air pressure of 0.21MPa. Then the tire is placed in a test environment at a constant temperature for 2h and adjusted to eliminate the error in air pressure caused by the ambient temperature factor. Before the uniformity test begins, the tire is warmed up for 30min under the test load at a speed of 120km/h to equilibrate the air pressure inside the tire. According to the given vertical load, speed, and rotational direction, the corresponding RFV and its first harmonic are then obtained. Simultaneously, the geometric measurement system can capture the data of the corresponding RRo. For the low-speed uniformity measurement, the standard testing speed is 60rpm. The data sampling period is 1s, which equals one rotating period of the tire. The number of sampling points in one period is 256.

Figure 4.1: Experimental system setup of the tire uniformity measurement.

4.1.1 Modeling radial run-outs

Structural and geometric non-uniformities in tires can directly affect the distribution of contact forces and consequently influence the dynamic response of the tire [68, 71]. The radial run-out of the center-point (RRoc), which is the error of the nominal radius, inevitably arises during the tire manufacturing process. In this study, the RRoc is introduced into the flexible ring model, and the resulting deviation of the contact forces distribution is analyzed. In the contact model, RRoc

is considered to be the factor that causes the variation of the tread rubber thickness. Eq. (3.98) is reformulated as

$$F_{ns} = k_{Es}\left[u_s - (h_0 + \lambda_R)\right], \tag{4.119}$$

where λ_R is the RRoc. Therefore, when geometric uniformity is introduced, the additional generalized forces are generated in the dynamic system and this part of the excitation is subsequently transferred to the rigid ring model, which in turn affects the output of the dynamic response. The influence of the RRoc on the RFV is discussed in the following section.

4.1.2 Parameter optimization for tires with geometric defects

As clarified in Section 7.4, when the parameters are identified from the experimental data, the complete coupled rigid-flexible ring model and its parameters are established. This set of parameters is then available for the dynamics simulation of the tires. Taking into account the differences between each tire that exist in the production process, this work utilizes a GA to further optimize the physical parameters of the model. The measured tire is also “non-uniform" to some extent, so it is always possible to modify and optimize the model parameters somehow by using the test results of the corresponding low-speed uniformity of this tire. The parameters to be optimized include the stiffness and damping coefficients in the flexible ring model (see Table 3.3), and the stiffness and damping coefficients of the 3-DOF element in the rigid ring model (see Table 3.4, except for the mass and the moment of inertia of the rigid ring and the rim).

For this, the GA for optimization of the model parameters applied here was developed as a MATLAB toolbox. It is part of the Global Optimization Toolbox consisting of a set of MATLAB functions that generate an initial population, perform genetic operations, and implement the selection process. For a given set of RRoc, the GA is performed to optimize part of the model parameters by successive iterations, which enables these parameters to minimize the deviation between the predicted results and the test data of the corresponding RFV. All test data were obtained by the test procedure presented in Section 4.1. To determine 14 parameters using the GA, 126 generations with a size of 150 populations are selected. In the GA, both the simulated and tested datasets used for the computation of the fitness function take one rolling period (1s) from the RFV results. The time step for the simulation in the coupled rigid-flexible ring model is set to the same value as the test sampling interval, i.e., 1/256s, to ensure that the datasets are of equal length in calculating the error. Further, this guarantees that the tested and evaluated results at the same time instants are utilized.

The optimized physical parameters of the flexible ring model are presented in Table 3.3 and those

of the rigid ring model are shown in Table 3.4. Fig. 4.2 shows the RRoc data used for optimization, as well as the comparison of the RFV simulated results with the test data. To illustrate the influence of RRoc, whose value is normalized and plotted in the same figure with the RFV results using the double y-axis. The value of RRoc is shown on the right y-axis in Fig. 4.2(b).

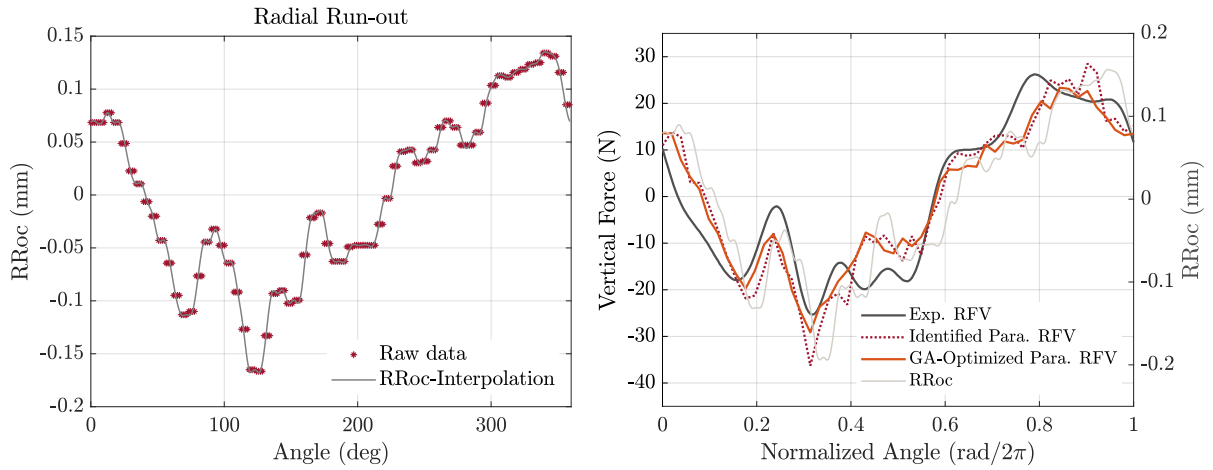

(a) A set of RRoc test data used for identification and optimization.

(b) The comparison of the RFV simulated results with the experimental data.

Figure 4.2: A set of RRoc data and corresponding measurement results of RFV for parameter identification using the GA.

4.2 Deterministic analysis of low-speed uniformity

4.2.1 Contact forces variation with RRoc

Geometric non-uniformities of tires directly lead to the variation of contact forces. It is assumed that the variation of the thickness of the tread rubber is the cause of RRoc in this study, which can simplify the modeling process by neglecting the stiffness variation and non-uniform internal material distribution. To fit the test data with the nodes of the discretized flexible ring, it is necessary to interpolate the raw RRoc data so that its influence can be introduced in the contact model. The raw test data and the interpolated curve for a set of RRoc are shown in Fig. 4.3(a). Considering the test condition of the low-speed uniformity test rig, the height of the spindle is fixed and the rolling speed is set to 60rpm. The variation of the vertical contact force induced by the RRoc is shown in Fig. 4.3(b). The “uniform radius" in Fig. 4.3(b) refers to the ideal design parameter, i.e., without any dimensional variations. The slight deviation of the value (black solid line) is due to the discretization of the flexible ring in the contact algorithm.

Table 4.1: Optimized physical parameters of the flexible ring.

Parameter type	Unit	Identified Value	GA Optimized
In-plane bending stiffness EI	Nm^2	2.10	2.199
Radial stiffness of the sidewall k_u	N/m^2	4.54×10^5	4.43×10^5
Circumferential stiffness of the sidewall k_v	N/m^2	1.77×10^5	1.86×10^5
Radial damping coefficient of the sidewall c_u	Ns/m^2	222.47	228.04
Circumferential damping coefficient of the sidewall c_v	Ns/m^2	218.13	258.32
Undeformed thickness of tread rubber h_0	m	0.0125	0.0140
Normal stiffness of tread rubber k_{Es}	N/m	4.63×10^5	3.64×10^5
Tangential stiffness of tread rubber k_{Gs}	N/m	3.60×10^5	3.30×10^5

Comparing the test data of the RRoc with the corresponding variation of the vertical contact force, it is observed that although the amplitude fluctuation of the RRoc is only 0.316mm, the variation of the steady-state vertical force reaches 63.93N. This indicates that the uniformity of tires is a crucial factor to be considered in the comfort and handling simulation. If the curve of the RRoc is compared with the variation of the static contact force as given in Fig. 4.3(b), it indicates that the filtering effect of the tire structure on the RRoc is reflected, which means that not all the small peaks and minor fluctuations of the profile curve are transmitted to the response of the contact force completely. The reason for this phenomenon includes the influence of the elasticity of the material and the geometric construction, which is revealed in the length of the contact footprint.

4.2.2 Comparison with experimental results of RFV

In this section, the algorithm established in the previous chapter is used to respectively analyze the low-speed uniformity characteristics of two tires with geometric defects (Tire-RRoc1 and Tire-RRoc2), which includes the results in time and frequency domains.

Time-domain analysis

In this case study, using the coupled rigid-flexible ring model established in the preceding part, the RRoc is selected as the input parameter to calculate the corresponding RFV. The comparison for the

Table 4.2: Optimized physical parameters of the rigid ring.

Parameter type	Unit	Identified Value	GA Optimized
Mass of the rim m_a	kg	7.80	-
Mass of the rigid ring m_b	kg	6.90	-
Moment of inertia of the rim I_{ay}	kg·m^2	0.455	-
Moment of inertia of the rim I_{by}	kg·m^2	0.643	-
Longitudinal stiffness of the spring k_{bx}	N/m	2.76×10^5	6.58×10^5
Vertical stiffness of the spring k_{bz}	N/m	1.19×10^6	0.840×10^6
Torsional stiffness of the spring $k_{b\theta}$	N/rad	8.27×10^5	6.26×10^5
Longitudinal damping coefficient c_{bx}	Ns/m	4.03×10^2	5.32×10^2
Vertical damping coefficient c_{bz}	Ns/m	4.38×10^2	9.12×10^2
Torsional damping coefficient $c_{b\theta}$	Ns/rad	2.18×10^2	3.70×10^2

time-domain simulation of the RFV with the measured data on the low-speed uniformity test rig is shown in Fig. 4.4.

Comparing the curve shape of the RRoc and its corresponding RFV, it reveals that the RRoc is the primary factor affecting the RFV at low speed. By contrasting the simulation result with the experimental data, it states that the coupled rigid-flexible ring model can properly describe the trend of the amplitude and peak positions of the RFV, but there are still some deviations in the numerical results. One of the reasons is that only the in-plane dynamic responses are considered in the proposed model. It consequently cannot reflect the geometric imperfections in the width direction of the tread, such as the out-of-roundness of the tire shoulder and the taper effect, etc. Another reason for the error is that the non-uniform stiffness distribution is not introduced into the model, including the stiffness deviation caused by the lap joints in the interior structure of tires and the asymmetrical sidewall. However, these factors can still have an impact on RFV.

Frequency-domain analysis

Herein, the spectrum analysis of the simulated results is conducted. The measured data obtained from the low-speed uniformity measurements were filtered up to the 12$^{\text{th}}$-order as a result of the limitation of the test rig. For this, an 8$^{\text{th}}$-order Butterworth low-pass filter with a cut-off frequency

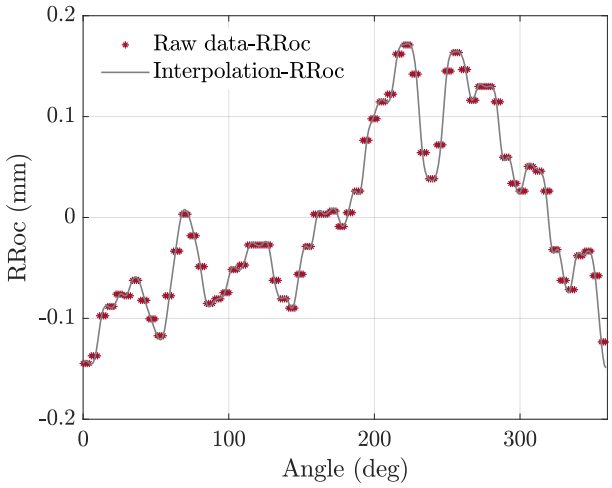

(a) The raw test data and the interpolated curve for a set of RRoc.

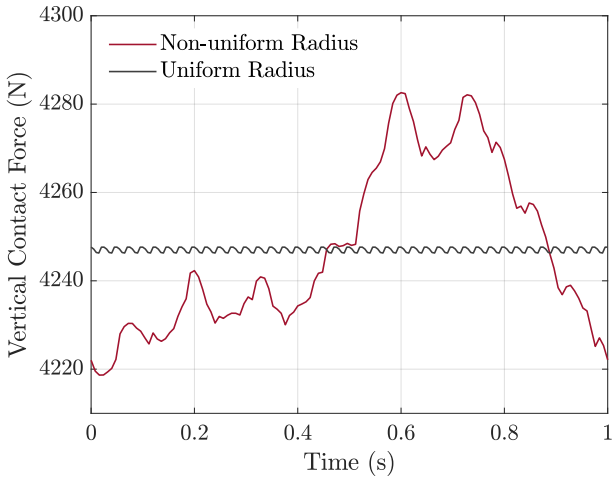

(b) The variation of the vertical contact forces.

Figure 4.3: The variation of the vertical contact force of the tire caused by the RRoc.

of 12Hz is implemented for the data processing of the simulated results. The experimental and simulated results of the one-sided amplitude spectrum of the RFV corresponding to the RRoc given in Fig. 4.3 are shown in Fig. 4.5(a). The power spectrum is given in Fig. 4.5(b).

Fig. 4.5 confirms that the simulation results can predict the peak positions with sufficient accuracy in the single-sided amplitude spectrum and the power spectrum of the RFV, and approximately predict the magnitude of each order frequency component. It suggests that the method for estimating RFV generated by RRoc based on the proposed coupled rigid-flexible ring model shows reasonably good accuracy and reliability.

4.3 Summary

In this chapter, the coupled rigid-flexible ring model has been extended to the analysis of low-speed uniformity of tires with geometric defects and has been validated experimentally. It indicates that the novel proposed model offers many application scenarios and extension possibilities. For the uniformity analysis of tires, the GA has been adopted to determine the physical parameters of a specific tire, and a set of RFV has been chosen as the performance index of the simulated algorithm. The impacts of the geometric imperfection have been evaluated in the proposed model. It has been found that a small amplitude fluctuation of the RRoc can lead to a large variation of the steady-state vertical contact force. Moreover, the filtering effect of the tire structure on the RRoc has been shown, which includes the influence of the elasticity of the material and the geometric construction.

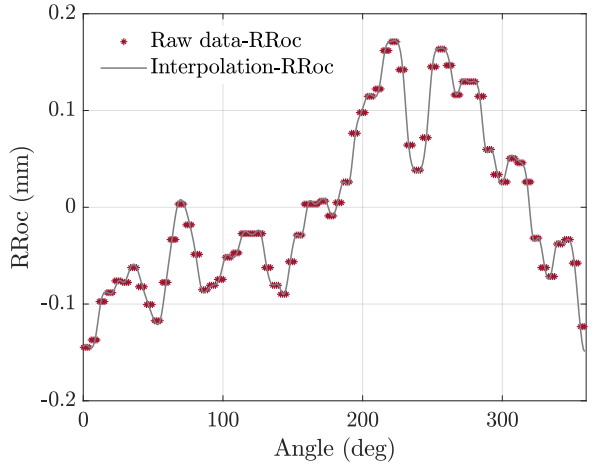

(a) The raw test data and the interpolated curve for a set of RRoc. (Tire-RRoc1)

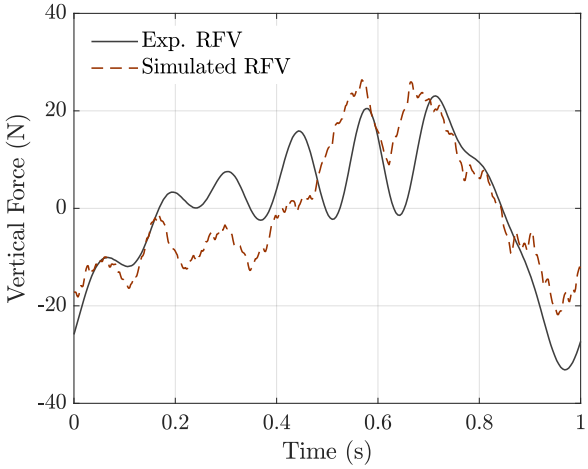

(b) The variation of the vertical contact forces. (Tire-RRoc1)

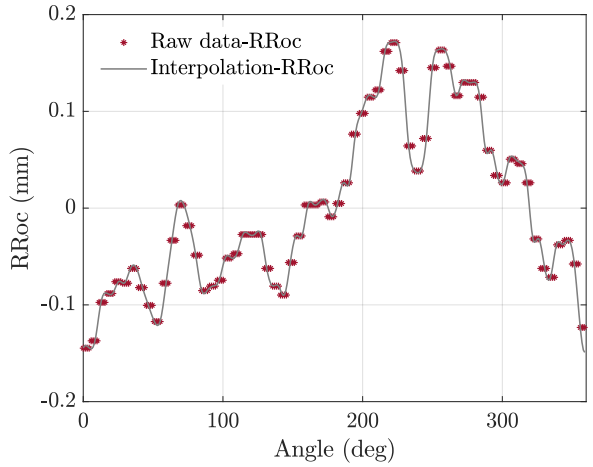

(c) The raw test data and the interpolated curve for a set of RRoc. (Tire-RRoc2)

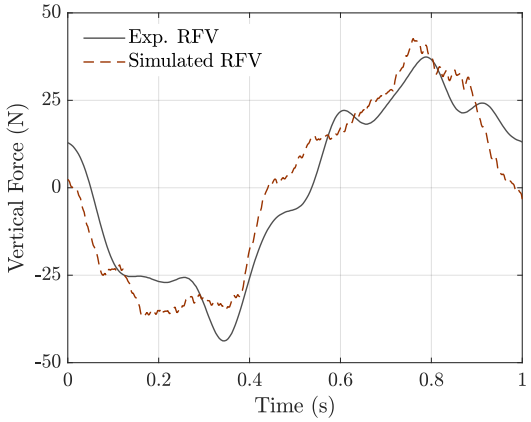

(d) The comparison of the simulated and measured RFVs. (Tire-RRoc2)

Figure 4.4: Comparison of the measured RFV with the simulation result.

The time-domain analysis shows that the RRoc is the most dominant factor affecting the RFV at low speed. By comparing the simulation result with the experimental data, it can be stated that the developed model adequately evaluates the amplitude and peak positions of the RFV. Furthermore, the one-sided amplitude spectrum and the power spectrum of the RFV simulation results have been accurately predicted. The accuracy and reliability of the extended method based on the coupled rigid-flexible ring model have been validated in the low-speed uniformity analysis for the tires with geometric defects.

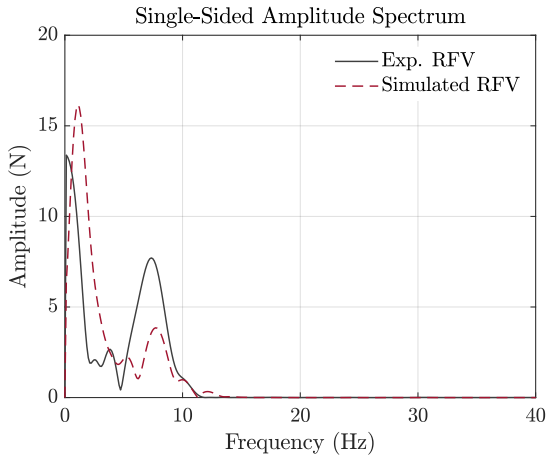

(a) The one-sided amplitude spectrum. (Tire-RRoc1)

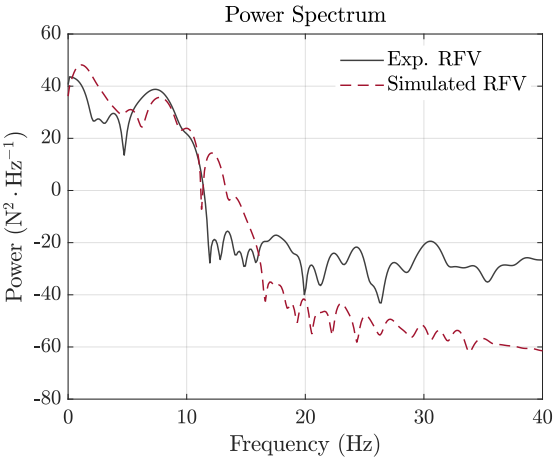

(b) The power spectrum. (Tire-RRoc1)

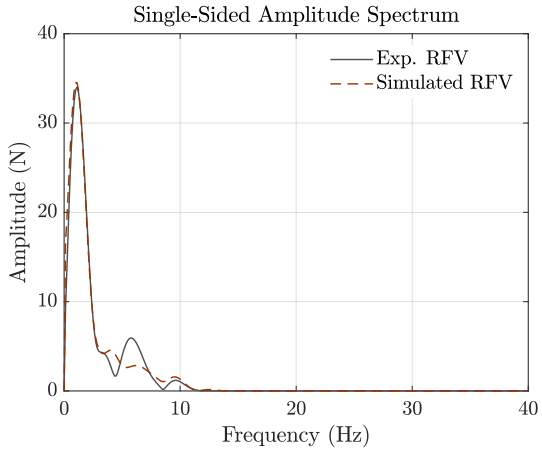

(c) The one-sided amplitude spectrum. (Tire-RRoc2)

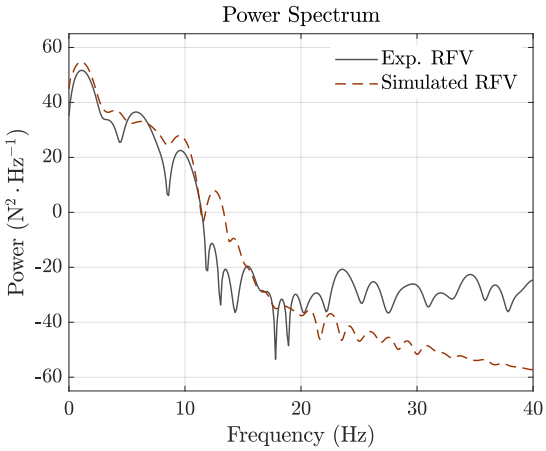

(d) The power spectrum. (Tire-RRoc2)

Figure 4.5: The spectrum analysis of the experimental data and the simulated result of the RFV.

Chapter 5

Theory of Polynomial Chaos Expansion in Uncertainty Quantification

This chapter focuses on the uncertainty quantification method based on the polynomial chaos expansion theory. From the viewpoint of probabilistic statistics, uncertainty quantification is to estimate the stochastic uncertainty in the output of a system with a given random input. It means that when the uncertainties exist in the random input $\mathbf{X} = \{X_1, X_2, \cdots, X_d\}$, the probabilistic statistical information of the output $Y = g(\mathbf{X})$ should be calculated, such as mean value, variance, failure probability, probability density function (PDF), etc. In this work, a stochastic expansion method is used to achieve uncertainty quantification of the dynamic behavior and vibration of tires. The main idea of this type of approach is to represent the random variables as a linear combination of several polynomials. This technique is more accurate and does not require the computation of the derivative of the response function. The most important is that once the expansion of random variables is performed, their probability statistics are conveniently available. Therefore, this chapter provides a brief introduction to the generalized polynomial chaos (gPC) theory. First, the orthogonal polynomials and a classical representation technique for stochastic processes are briefly introduced: the Wiener-Hermite expansion, which is the original Wiener polynomial chaos. Then the construction of gPC based on the Askey scheme is given. At last, the implementation of the gPC expansion based on the probabilistic collocation method (PCM) and the technique for selecting the collocation points are discussed.

5.1 Theory of polynomial chaos expansion

5.1.1 Orthogonal polynomials

The basic knowledge of orthogonal polynomials is first reviewed, which plays an important role in the theory of stochastic expansions and approximation. There are many in-depth discussions of the properties of orthogonal polynomials listed in [133–136]. The general form of an n-order polynomial is given as

$$Q_n(x) = a_n x^n + a_{n-1}x^{n-1} + \cdots + a_1 x + a_0, \quad a_n \neq 0, \tag{5.120}$$

where $x \in D$, a_n is the leading coefficient of the polynomial. Define a weight function $w(x) \geq 0$, and $\int_D w(x)\mathrm{d}x > 0$. If it satisfies the orthogonal relations,

$$\int_D Q_m(x)Q_n(x)w(x)\mathrm{d}x = \gamma_n \delta_{mn}, \tag{5.121}$$

where δ_{mn} is the Kronecker-delta function, i.e.,

$$\delta_{mn} = \begin{cases} 1, & m = n, \\ 0, & m \neq n, \end{cases} \tag{5.122}$$

then $Q_n(x)$ is defined as an orthogonal polynomial with a weight function $w(x)$ in the definition domain D. Here, γ_n are termed normalization constants, which are

$$\gamma_n = \int_D Q_n(x)Q_n(x)w(x)\mathrm{d}x. \tag{5.123}$$

The orthogonal polynomials follow the three-term recurrence relation,

$$-xQ_n(x) = b_n Q_{n+1}(x) + a_n Q_n(x) + c_n Q_{n-1}(x), \quad n \geq 0, \tag{5.124}$$

where $b_n \neq 0,\ c_n \neq 0,\ c_n/b_{n-1} > 0,\ Q_{-1}(x) = 0,\ Q_0(x) = 1$. According to the recurrence relation, different types of orthogonal polynomials can be constructed. Another form of the recurrence relation are expressed as [134, 137]

$$Q_{n+1}(x) = (A_n x + B_n)\, Q_n(x) - C_n Q_{n-1}(x), \quad n \geq 0, \tag{5.125}$$

where $A_n \neq 0,\ C_n \neq 0,\ C_n A_n A_{n-1} > 0,\ Q_{-1}(x) = 0,\ Q_0(x) = 1.$

5.1.2 Wiener-Hermite expansion

Briefly, the polynomial chaos (PC) is an approximation of a random expansion by summing a series of orthogonal polynomials that corresponds to the distribution type of the input parameters. The PC originated from the Wiener-Hermite chaos proposed by Wiener in 1938 [138], which is also termed as the homogeneous chaos [139]. Most physical processes can be described by a general second-order random process $y(\omega)$, which is a process with finite variance [139]. Herein, ω means a random event. It indicates that the quantities involved in it here are random variables, which is omitted in the subsequent section for simplicity of notation. The random process is represented by performing the orthogonal projection [137, 140] in the form of the polynomial chaos

$$\begin{aligned} y(\omega) = \alpha_0 \Gamma_0 + \sum_{i_1=1}^{\infty} \alpha_{i_1} \Gamma_1(\eta_{i1}(\omega)) + \sum_{i_1=1}^{\infty} \sum_{i_2=1}^{i_1} \alpha_{i_1 i_2} \Gamma_2(\eta_{i1}(\omega), \eta_{i2}(\omega)) \\ + \sum_{i_1=1}^{\infty} \sum_{i_2=1}^{i_1} \sum_{i_3=1}^{i_2} \alpha_{i_1 i_2 i_3} \Gamma_3(\eta_{i1}(\omega), \eta_{i2}(\omega), \eta_{i3}(\omega)) + \cdots, \end{aligned} \tag{5.126}$$

where $\boldsymbol{\eta} = \{\eta_{i1}, \eta_{i2}, \cdots, \eta_{in}\}$ is a set of independent standard random variables, $\hat{a}_0$ and $\hat{a}_{i_1, i_2, \ldots, i_r}$ are the deterministic coefficients, and Γ_p denotes the polynomial basis function, which is the polynomials of order p in terms of the multidimensional independent standard random variables $\boldsymbol{\eta}$. These orthogonal polynomials compose the linear space of polynomials of degree at most p, $\hat{\Gamma}_p$. It should be noted that the dimension of $\boldsymbol{\eta}$ is usually assumed to be the same as the dimension of the random inputs $\mathbf{X}$ in the original random space. In fact, the dimension of $\boldsymbol{\eta}$ should be able to represent the number of different random sources in the system. If a certain dimensional random variable X_i implicitly contains more than one random sources, the dimension of $\mathbf{X}$ should also correspondingly increase.

By adopting the orthogonalization procedure, Γ_p are constructed by different types of orthogonal polynomials. When the polynomial basis function is the same as the Hermite polynomials, a specific polynomial chaos can be generated. The general expression of Hermite polynomials $H_n(\boldsymbol{\xi})$ is

$$H_n(\xi_{i1}, \xi_{i2}, \cdots, \xi_{in}) = e^{\frac{1}{2}\boldsymbol{\xi}^{\mathrm{T}}\boldsymbol{\xi}} (-1)^n \frac{\partial^n}{\partial \xi_{i1} \partial \xi_{i2} \cdots \partial \xi_{in}} e^{-\frac{1}{2}\boldsymbol{\xi}^{\mathrm{T}}\boldsymbol{\xi}}, \tag{5.127}$$

where $\boldsymbol{\xi} = \{\xi_1, \xi_2, \cdots, \xi_n\}$ is the multidimensional independent standard Gaussian random variables.

The orthogonality of Hermite polynomials is expressed as

$$\left\langle H_i, H_j \right\rangle = \left\langle H_i^2 \right\rangle \delta_{ij}, \tag{5.128}$$

where δ_{ij} is the Kronecker-delta function and $\langle \cdot, \cdot \rangle$ denotes the inner product of Hilbert space, which is represented as

$$\left\langle f_1(\boldsymbol{\xi}), f_2(\boldsymbol{\xi}) \right\rangle = \int f_1(\boldsymbol{\xi}) f_2(\boldsymbol{\xi}) w(\boldsymbol{\xi}) \mathrm{d}\boldsymbol{\xi}, \tag{5.129}$$

where $w(\boldsymbol{\xi})$ is the weight function. The weight function of Hermite polynomials is

$$w(\boldsymbol{\xi}) = \frac{1}{\sqrt{(2\pi)^n}} e^{-\frac{1}{2}\boldsymbol{\xi}^{\mathrm{T}}\boldsymbol{\xi}}. \tag{5.130}$$

Hence, with a set of independent standard Gaussian random inputs, a random process is expanded by the Hermite polynomials in the following form,

$$y(\omega) = \sum_{k=0}^{\infty} \hat{a}_k \Gamma_k(\boldsymbol{\xi}), \tag{5.131}$$

in which the polynomial basis function $\Gamma_k(\boldsymbol{\xi})$ and the Hermite polynomials of order n, i.e., $H_n(\boldsymbol{\xi})$, have a one-to-one correspondence, as well as between them and the coefficients $\hat{a}_k$. This approximation method for random processes was first proposed by Wieners [138] and is therefore also known as the Wiener-Hermite expansion. In general, Eq. (5.131) is referred to as the polynomial chaos expansion (PCE) model.

However, in Eq. (5.131), the number of terms in the PCE is infinite, so for the consideration of computational implementation, the expansion needs to be truncated at the p^{th} order, which means the highest order of the Hermite polynomials is p. The corresponding p-order PCE model is expressed as

$$y(\omega) \approx \tilde{y}(\omega) = \sum_{k=0}^{P} \hat{a}_k \Gamma_k(\boldsymbol{\xi}). \tag{5.132}$$

The number of coefficients in the truncated p-order PCE model is Q, which is calculated by

$$Q = P + 1 = \frac{(n+p)!}{n!p!}. \tag{5.133}$$

Although Q increases considerably with the order of the PCE model p and the dimension of

the random variables n, using Wiener-Hermite polynomial chaos still achieves the exponential convergence rate when solving a system involving Gaussian distributed random variables. Moreover, Hermite-chaos can also be employed for other distributed types of random inputs by transforming a non-Gaussian distributed random variable into a standard normal distribution. But the convergence rate of the PCE model will inevitably be reduced.

5.2 Generalized polynomial chaos (gPC)

5.2.1 The Askey scheme

As mentioned before, the PCE model can well deal with the problem in the Gaussian-distributed random field. However, the literature [141] demonstrates that for more general random inputs, the PCE model can converge but with a severely deteriorated rate. So is there an analogy to Wiener-Hermite polynomial chaos that makes the solution as effective for systems including general non-Gaussian random inputs?

Therefore, to overcome this problem, Xiu and Karniadakis [93, 139] generalized the concept of the original Wiener's Hermite-chaos and obtained a family of polynomial chaos for the random variables with different distribution types, i.e., the Askey-chaos. According to the Askey scheme, the optimal orthogonal polynomials corresponding to each class of distribution are established so that the weight functions are the same as or differ by only a constant factor from the PDFs of the random variable. Thus, the basis functions in Eq. (5.126) are not restricted to Hermite polynomials, but any type of polynomials in the Askey scheme, while achieving an exponential rate of convergence. This generalized form of the Hermite-chaos is defined as the generalized polynomial chaos (gPC) or the Askey-chaos [137, 139]. In the literature [139], the correspondence between the type of gPC and their underlying random variables is shown in Table 5.1.

5.2.2 Generalized polynomial chaos (gPC) expansion

The Askey-chaos provides the optimal basis functions for the approximation of some specific types of random inputs, and the selection criterion is that the PDF of the random variable coincides with the weight function of the orthogonal polynomials. In this case, the type of random input is not limited to the standard Gaussian distribution but is any distribution type in the Askey scheme. This generalized form of PCE is defined as the generalized polynomial chaos (gPC) expansion [137, 139].

Table 5.1: The correspondence between the type of generalized polynomial chaos and their underlying random variables ($N \geq 0$ is a finite integer) [139].

	Randon variables	Wiener-Askey Chaos	Support
Continuous	Gaussian	Hermite-chaos	$(-\infty, \infty)$
	Gamma	Laguerre-chaos	$[0, \infty)$
	Beta	Jacobi-chaos	$[a, b]$
	Uniform	Legendre-chaos	$[a, b]$
Discrete	Poisson	Charlier-chaos	$\{0, 1, 2, \cdots\}$
	Binomial	Krawtchouk-chaos	$\{0, 1, \cdots, N\}$
	Negative binomial	Meixner-chaos	$\{0, 1, 2, \cdots\}$
	Hypergeometric	Hahn-chaos	$\{0, 1, \cdots, N\}$

Similar to the Hermite-chaos, Eq. (5.131), a general random process $\chi(\omega)$ of interest is represented as

$$\chi(\omega) = \hat{x}_0 \Phi_0 + \sum_{i_1=1}^{\infty} \hat{x}_{i_1} \Phi_1(\zeta_{i_1}) + \sum_{i_1=1}^{\infty} \sum_{i_2=1}^{i_1} \hat{x}_{i_1 i_2} \Phi_2(\zeta_{i_1}, \zeta_{i_2}) + \sum_{i_1=1}^{\infty} \sum_{i_2=1}^{i_1} \sum_{i_3=1}^{i_2} \hat{x}_{i_1 i_2 i_3} \Phi_3(\zeta_{i_1}, \zeta_{i_2}, \zeta_{i_3}) + \cdots, \tag{5.134}$$

where $\hat{x}_0$, $\hat{x}_{i_1}$, and $\hat{x}_{i_1 i_2 \ldots}$ are the deterministic coefficients of the gPC expansion, $\Phi_i(\boldsymbol{\zeta})$ is a set of orthogonal polynomials concerning the vector consisting of the random variables $\boldsymbol{\zeta} = \{\zeta_{i1}, \zeta_{i2}, ..., \zeta_{in}\}$, which denotes the Askey-chaos of order n. For simplicity of notation, Eq. (5.134) is usually rewritten by a truncation of the infinite series after $(N+1)$ terms as

$$\chi(\boldsymbol{\zeta}) = \sum_{i=0}^{N} \hat{x}_i \Phi_i(\boldsymbol{\zeta}), \tag{5.135}$$

where $\hat{x}_i$ denotes the deterministic coefficients in the gPC expansion.Because each probability distribution type has a corresponding optimal orthogonal polynomial basis, the distribution types of the random inputs should be pre-known. In the scenario of practical applications, the Pearson model [142, 143] is one implementation for the identification of distribution types, and the detailed theory is stated in Section 7.2. When the type of the orthogonal polynomials has been determined,

the most crucial step is to determine the coefficients of the gPC expansion. There are usually two methods to solve it: the probabilistic collocation method (PCM) [137, 144] and the Galerkin projection method [137, 145]. Typically, the distribution types of the input parameters are known or can be identified. So the Galerkin projection method is used to calculate the gPC coefficients $\hat{x}_i$ by utilizing the orthogonality of polynomials, i.e.,

$$\hat{x}_i = \frac{\langle \chi, \Phi_i(\boldsymbol{\zeta}) \rangle}{\langle \Phi_i^2 \rangle}, \qquad i = 0, 1, 2, ..., N. \tag{5.136}$$

However, the probabilistic distribution of the output variables is not foreknown. The coefficients cannot be directly computed by implementing the inner product in the Galerkin projection method. Therefore, the PCM is adopted here, which is capable of processing complex nonlinear equations efficiently.

5.3 Probabilistic collocation method (PCM)

5.3.1 Implementation of PCM

The PCM is a surrogate model developed with the gPC expansion, which is an extension of the stochastic response surface method (SRSM) [94] based on regression methods. The PCM forces the residual error at each sampling point to be determined as zero. To obtain an accurate result for the unknown coefficients, the oversampling technique is usually performed. Because the gPC expansion is a function of the standard random variables, N_c sets of available sampling points $\boldsymbol{\zeta}^s = \left\{ \boldsymbol{\zeta}_1^s \cdots \boldsymbol{\zeta}_j^s \cdots \boldsymbol{\zeta}_{N_c}^s \right\}$, where $\boldsymbol{\zeta}_j^s = \left\{ \zeta_{j1}^s \cdots \zeta_{jk}^s \cdots \zeta_{jn}^s \right\}$, need to be selected in the standard random space (ζ-space). When substituting each set of sample points into the deterministic equations $g(\mathbf{X})$, $\boldsymbol{\zeta}^s$ should be transformed into the original physical random space (X-space) and then used to compute the corresponding output responses. In short, the PCM provides a surrogate model, i.e.,

$$\begin{bmatrix} \Phi_0\left(\boldsymbol{\zeta}_1^s\right) & \Phi_1\left(\boldsymbol{\zeta}_1^s\right) & \cdots & \Phi_N\left(\boldsymbol{\zeta}_1^s\right) \\ \Phi_0\left(\boldsymbol{\zeta}_2^s\right) & \Phi_1\left(\boldsymbol{\zeta}_2^s\right) & \cdots & \Phi_N\left(\boldsymbol{\zeta}_2^s\right) \\ \vdots & \vdots & \ddots & \vdots \\ \Phi_0\left(\boldsymbol{\zeta}_{N_c}^s\right) & \Phi_1\left(\boldsymbol{\zeta}_{N_c}^s\right) & \cdots & \Phi_N\left(\boldsymbol{\zeta}_{N_c}^s\right) \end{bmatrix} \begin{Bmatrix} \hat{x}_0 \\ \hat{x}_1 \\ \vdots \\ \hat{x}_N \end{Bmatrix} = \begin{Bmatrix} g\left(\mathbf{X}_1^s\right) \\ g\left(\mathbf{X}_2^s\right) \\ \vdots \\ g\left(\mathbf{X}_{N_c}^s\right) \end{Bmatrix}. \tag{5.137}$$

The matrix form of Eq. (5.137) is expressed as

$$\mathbf{A}\hat{\mathbf{x}} = \mathbf{G}, \tag{5.138}$$

in which $\hat{\mathbf{x}}$ is the vector of the unknown coefficients, $\mathbf{A}$ is an $N_c \times (N+1)$-dimensional coefficient matrix obtained by substituting the standardized collocation points into the orthogonal polynomials, and $\mathbf{G}$ means the vector of the corresponding output responses at the collocation points. By adopting least-squares regression, the coefficients $\hat{\mathbf{x}}$ are calculated, i.e.,

$$\hat{\mathbf{x}} = (\mathbf{A}^{\mathrm{T}}\mathbf{A})^{-1}\mathbf{A}^{\mathrm{T}}\mathbf{G}, \tag{5.139}$$

where $(\mathbf{A}^{\mathrm{T}}\mathbf{A})^{-1}$ is an invertible N_c-order matrix. Once the coefficients are obtained, the statistical property of the output can be simply estimated by performing the MCSs on the gPC extended model. Thereby, the computational efficiency issue arising from massive calls to the deterministic analysis model is evaded. It is important to note that the sample points used as the inputs to the MCSs should be generated in the standard probability space.

5.3.2 Selection of the collocation points

The key point of the construction of the PCM model is the solution of the unknown coefficients. Hence, it requires some input and output value sample points. For a set of random inputs $\boldsymbol{\zeta}$ with n-dimensional independent random variables, the number of the unknown coefficients $(N+1)$ for a p^{th}-order gPC expansion is calculated by Eq. (5.133), i.e.,

$$N+1 = \frac{(n+p)!}{n!p!}. \tag{5.140}$$

When the PCM is adopted to solve the coefficients, the number of the collocation points N_c is generally larger than the number of undetermined coefficients N to obtain a robust result. It can balance the influence of each collocation point and also overcome the instability brought by individual collocation points. The method of selecting the collocation points apparently determines part of the accuracy of PCM. In this work, the following three sampling methods for selecting the collocation points are discussed to obtain an efficient but accurate sampling method: random sampling, Latin hypercube sampling (LHS), and the linear-independence-based roots method.

1. Random sampling

After transforming the uncertain variables into their standard probability space, equal probability

sampling (EPS) can be employed in the interval of variables. However, it usually requires a huge sample size and leads to low computational efficiency.

2. Latin hypercube sampling (LHS)

Traditional random sampling generates sample points that are difficult to effectively cover the tails of the probability distribution of variables, and most of them are concentrated near the mean value. Since the tails of the distribution have an important influence on the reliability analysis, the LHS technique can be applied to generate multivariate samples to improve the global accuracy of computation. LHS was first proposed by McKay *et al.* [146] in 1979, which has good one-dimensional projection and uniform stratified distribution properties and can fully cover the upper and lower bounds.

- The range of the cumulative distribution function (CDF) of each variable is divided into n non-overlapping intervals on the basis of equal probabilities.
- Randomly select a value from each interval and repeat this step until the values of all random variables are generated.
- Pair the n sample points obtained for each variable with those obtained for the other variables randomly.

This technique provides an optional sample size while ensuring stratified sampling, which means that each input variable is sampled at n levels. For a more detailed theoretical description of LHS, it is possible to refer to Ref. [88–90]. LHS has superior advantages over MCS for complex intensive computational analysis, which can result in a significant reduction in numerical computation in the current scheme.

3. Linear-independence-based roots method

Generally, when the order of the gPC approximation p is given, the collocation points can be generated from the combination of the roots of the $(p+1)^{\text{th}}$-order orthogonal polynomial. Especially for an even-order polynomial, when adding the origin as a root, the total number of available points N_c is given as

$$N_c = \begin{cases} (p+1)^n, & p = \text{odd number} \\ (p+2)^n, & p = \text{even number} \end{cases}. \tag{5.141}$$

It is clear that as p increases, the number of collocation points grows exponentially and will rapidly become much larger than the number of unknown coefficients, i.e., $N_c \gg (N+1)$. Considering

the unique-solution condition for linear non-homogeneous systems, the coefficient matrix $\mathbf{A}$ in Eq. (5.138) should be of full rank $(N+1)$. Therefore, it is adequate to select only $(N+1)$ sets from N_c collocation points. Also, the selected $(N+1)$ sets of collocation points should be located as many as possible in regions with a high probability density. Herein, an improved PCM combined with the linear-independence-based roots method (PCM-Indep) [123, 147, 148], is introduced, and it can be performed as follows. The N_c sample points are first sorted according to decreasing order of the probability density. Then, the coefficients in the matrix $\mathbf{A}$ corresponding to the $(k+1)^{\text{th}}$ collocation point are calculated in sequence. The $(k+1)^{\text{th}}$ row must be linearly independent to the selected k rows of the matrix $\mathbf{A}$. Or else, the point that has the next highest probability density is checked until $(N+1)$ sets of collocation points fulfilling the conditions are selected.

Once the distribution types of the input parameters and the corresponding gPC expansions are defined, the selection of the collocation points can be implemented prior to the overall computational process, even if it is done by conducting the linear independence test. The selected collocation points can be directly used for the next calculation. Such a process can bring an improvement in the performance of the PCM analysis, especially for some time-consuming deterministic models. In the subsequent numerical analysis, the practicability of this approach is demonstrated by the stochastic analysis of a series of actual tires.

5.4 Summary

In order to estimate the impacts of the uncertainties resulting from the tire manufacturing process, the theory of gPC is briefly reviewed in this chapter. Here, the theoretical basis and the solution process applied to the analysis of uncertainty quantification are explained. This chapter emphasizes several sampling techniques in the PCM for solving the coefficients of the gPC expansion. In particular, the PCM-Indep provides an efficient approach to selecting collocation points. It is employed with other sampling techniques in the subsequent chapters and their computational efficiency is also compared.

Chapter 6

Applications of Uncertainty Quantification in Tire Vibration

On the basis of the proposed deterministic model, probabilistic characteristics of natural frequencies and sound power radiation are analyzed using the gPC expansion method. Here, the orthogonal expansion method based on the homogeneous chaos theory is introduced and the MCS is applied for validation. As mentioned earlier, the key point of the gPC expansion method is determining the unknown deterministic coefficients of the gPC expansions. For practical applications, the distribution type should be identified from experimental data [109, 116]. In this work, without loss of generality, the distributions are arbitrarily chosen. A certain distribution type of these input uncertain parameters is assumed. The stochastic free vibration due to uncertainties in structural parameters and internal pressure is first discussed.

6.1 Natural frequencies

In this case study, three parameters of a tire, membrane stiffness EA, in-plane bending stiffness EI_z, and internal pressure p_0, are considered as input random parameters which affect the dispersion property of the in-plane natural frequency. All the model parameters are assumed independent. The structural parameters, EA, and EI_z, are assumed normally distributed and the internal pressure p_0 follows a uniform distribution. The distributions of these parameters are listed in Table 6.1. Here, $U(a,b)$ represents a uniform distribution with the minimum bound a and the maximum bound b. $N(\mu,\sigma^2)$ denotes a normal distribution. The parameter μ is the mean of the distribution and σ^2 is its variance.

Table 6.1: Mean and distribution of the input variables for in-plane vibration analysis.

Parameter	Distribution Type	Mean
p_0 ($\times 10^5$ Pa)	U (7.47, 9.13)	8.3
EI_z (Nm^2)	N (7.401, 0.85)	7.401
EA (N)	N (4.603×10^7, 5×10^5)	4.603×10^7

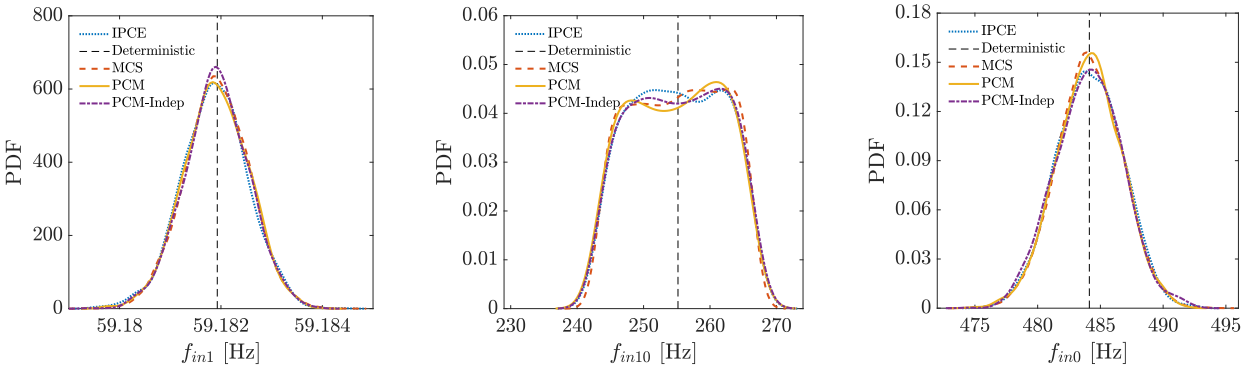

(a) 1st-order radial mode. (b) 10th-order radial mode. (c) 0th-order circumferential mode.

Figure 6.1: Distributions of in-plane natural frequencies. (PCM-Indep means the linear-independence-based PCM.)

Herein, four methods, including the intrusive PCE, MCSs, conventional PCM, and the linear-independence-based PCM, are adopted to show the influence of the random parameters on the in-plane free vibration of the tire. Firstly, the random variables expanded according to the Eq. (5.135) are directly substituted into the analytical expression of the natural frequency given in [32]. Then the conventional PCM and the linear-independence-based PCM are applied. The output responses are approximated by using 3rd-order gPC expansion. Fig. 6.1 presents a comparative plot of 10000 MCSs to verify the effectiveness of the gPC expansion method.

A similar analysis method is adopted to analyze the effects of torsional inertia ρI_p, torsional rigidity GI_p, and out-of-plane bending stiffness EI_r on the stochastic out-of-plane free vibration of the tire. The structural parameters, GI_p, and EI_r, are assumed normally distributed and the torsional inertia ρI_p follows a uniform distribution. distributions are shown in Table 6.2. Compared with the in-plane vibration, some similar conclusions are drawn. It is found that the structural uncertainty has very little impact on the lower order natural frequencies, however, for the higher order modes and some special 0th-order modes the influence of the uncertainty becomes greater.

Meanwhile, the effectiveness of the linear-independence-based PCM is illustrated. The errors

Table 6.2: Mean and distribution of the input variables for out-of-plane vibration analysis.

Parameter	Distribution Type	Mean
ρI_p (kg/m)	U (0.23, 0.29)	0.26
GI_p (Nm^2)	N (1.61×10^3, 1.61×10^2)	1.61×10^3
EI_r (Nm^2)	N (1.06×10^5,1.06×10^4)	1.06×10^5

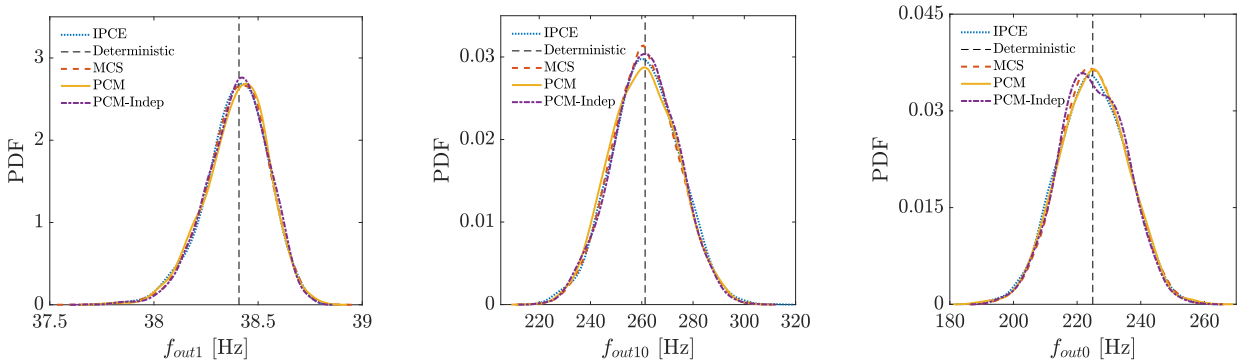

(a) 1st-order lateral mode. (b) 10th-order lateral mode. (c) 0th-order torsional mode.

Figure 6.2: Distributions of out-of-plane natural frequencies. (PCM-Indep means the linear-independence-based PCM.)

of different collocation point methods are shown in Table 6.34. It can be found that even if 125 collocation points are selected in the conventional PCM, the accuracy of the solution for calculating the mean value has not been much improved. When 76 collocation points are tested based on the criteria as discussed previously, the matrix **A** has a full rank of 20 equaling the number of unknown coefficients in the gPC expansion. The generation of the collocation points to be tested depends on the type of random variables, the dimension of the random vector, and the order of the gPC expansion. The result of the selection does not rely on the deterministic model. Therefore, it is possible to carry out the linear-independent tests before the computational progress. It can be found that the linear-independence-based PCM is much more efficient than the conventional PCM.

6.2 Effects of levels of uncertainties on natural frequencies

Furthermore, the levels of uncertainties affected by the natural frequency are investigated. The variances of all the random input parameters are varied from 5% to 20%. It is observed in Fig. 6.3 that, as the level of uncertainty increases, corresponding frequency responses are more dispersed.

Table 6.3: Comparison of the 10th order radial natural frequency between different collocation point methods and MCS.

Method	Sample Number	$\bar{f}$ (Hz)	Error (%)
Deterministic	-	255.18	-
MCS	10000	255.18	0.001
PCM	125	254.86	0.126
Linear-independence-based PCM	20	255.08	0.039

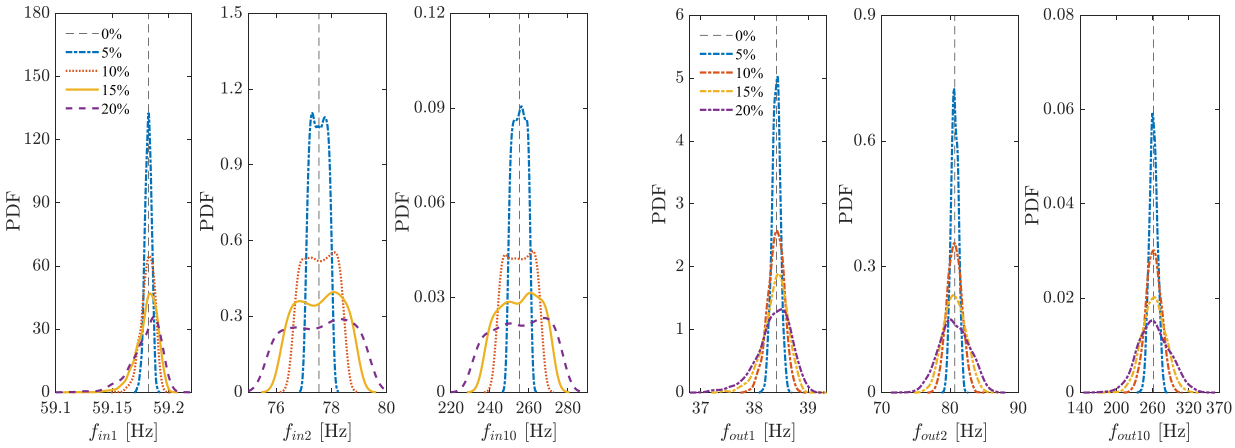

(a) Radial modes. (b) Lateral modes.

Figure 6.3: Distribution of 1st-, 2nd-, and 10th -order natural frequencies under different variances of input parameters.

Here, a situation is considered, in which the uncertainty exists only in one parameter, and meanwhile, the other input variables remain deterministic. It is observed in Figs. 6.4(a) and (b) that the membrane stiffness EA has a significant influence on the breathing mode of the tire. However, the dispersion of higher-order radial modes caused by the internal pressure p_0 is greater than that of the other two variables, EA and EI_z. The distributions of natural frequencies are predominantly distributed symmetrically about the deterministic value. Moreover, in the out-of-plane vibration, when the uncertainty is considered only in ρI_p, the distribution of the natural frequency becomes non-symmetrical about the deterministic peak response, and it affects the distribution of each mode. This implies that the variation in the material and stiffness parameters of the tire significantly affect the distributions of the natural frequencies.

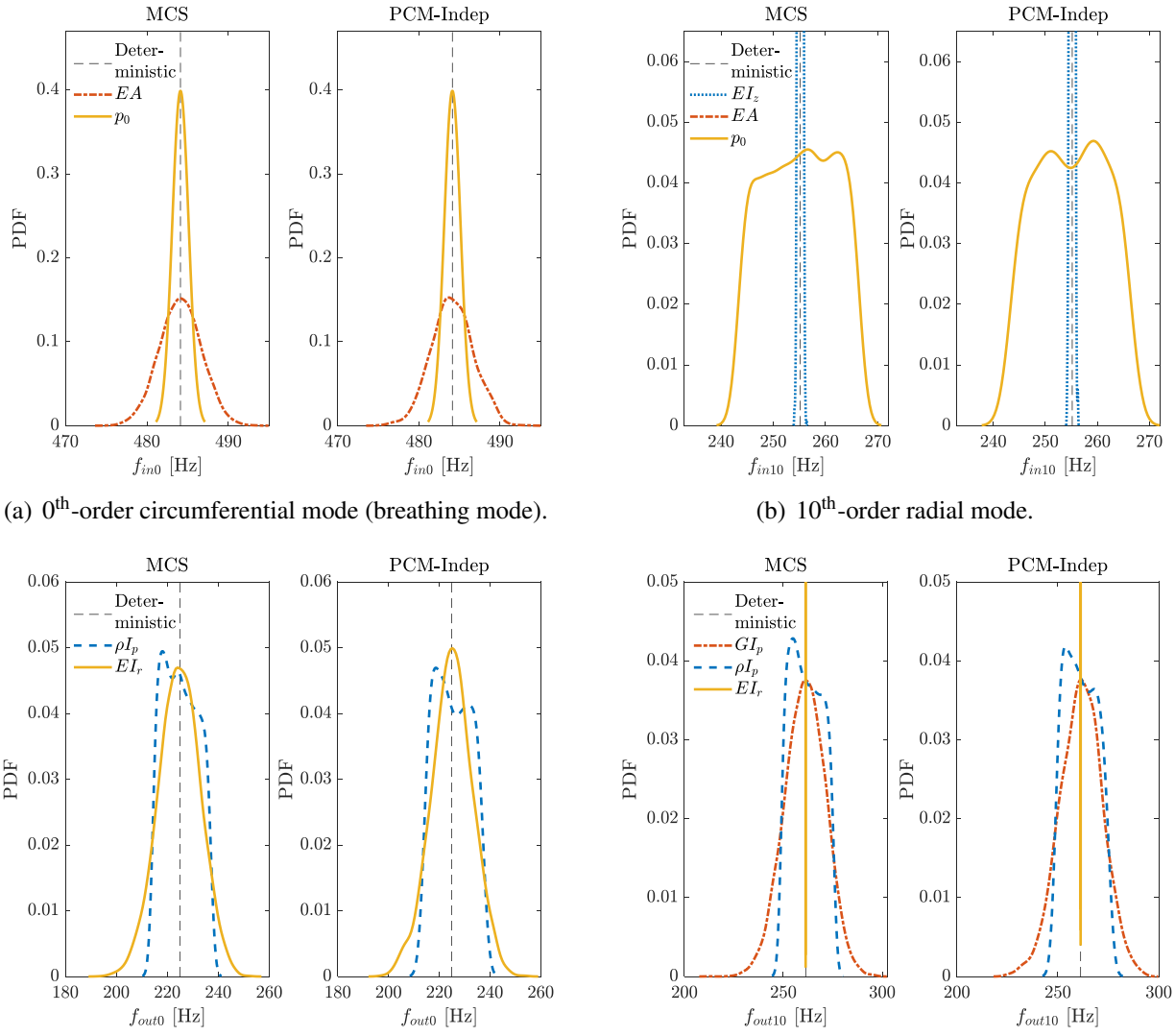

(a) 0^{th}-order circumferential mode (breathing mode).

(b) 10^{th}-order radial mode.

(c) 0^{th}-order torsional mode.

(d) 10^{th}-order lateral mode.

Figure 6.4: Effect of each individual parameter on natural frequencies. (PCM-Indep means the linear-independence-based PCM.)

6.3 Steady-state response and sound power

The random equivalent radiated sound power of the tire subjected to a harmonic excitation is investigated in this section. The amplitude A_f and the angular frequency ω_f of the excitation are selected as uncertain and assumed normally distributed. These two parameters are approximated by a 3$^{\text{rd}}$-order gPC expansion. Here the sound power is simulated for two vehicle speeds, 80km/h and 120km/h. The excitation frequency f is set as $\omega_f/2\pi$, which correspond to 6.67Hz and 10Hz, respectively. It signifies that the period of the excitation is equal to one rotating period. The distributions of these two parameters are listed in Table 6.4. Compared with the deterministic results of the equivalent radiated sound power, the probabilistic distributions under different speeds are shown in Fig. 6.5. It is shown that the distribution of the equivalent radiated sound power becomes more dispersed as the rolling speed increases, even if the variances of the input parameters are the same.

Table 6.4: Mean and distribution of the excitation variables.

Parameter	Distribution Type	Mean Value
A_f (N)	N (1, 0.1)	1
f_{80} (Hz)	N (6.67, 0.67)	6.67
f_{120} (Hz)	N (10, 1)	10

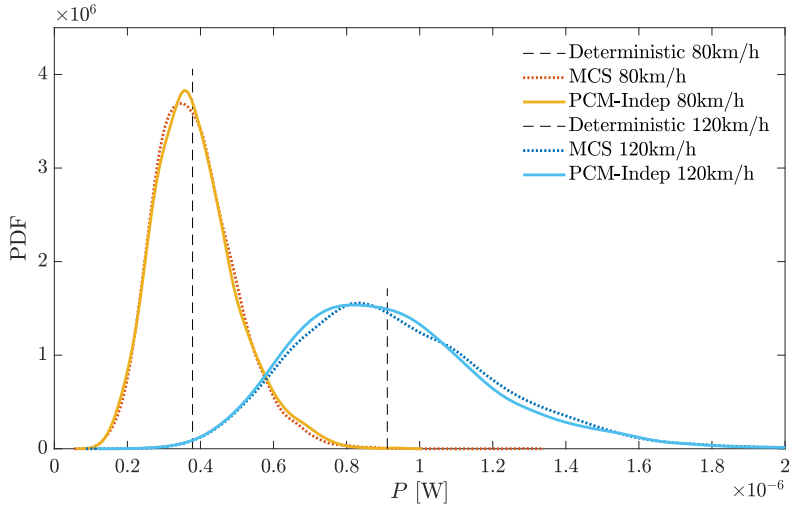

Figure 6.5: Distributions of equivalent radiated sound power under different rolling speeds.

6.4 Summary

In this chapter, the proposed method was applied to evaluate the influence of uncertainties in the structural parameters on the natural frequencies and the sound radiation characteristics under uncertain excitations. When the deterministic model was established, the gPC expansion method was used to estimate the influence of uncertainties. The non-intrusive PCM was employed to obtain the unknown coefficients of the gPC expansion of the natural frequencies and the equivalent radiated sound power. Considering the concept of linear independence of vectors, the number of selected collocation points was reduced as much as possible. This yielded an efficient simulation in terms of computational costs.

Numerical results of the natural frequencies due to uncertain structural parameters were compared with the MCS, which confirm the effectiveness of the proposed stochastic analysis. It has been found that the uncertain material and structural parameters affect each natural frequency. The membrane stiffness EA has a significant influence on the breathing mode of a tire. Furthermore, the sound power due to the forced vibrations under random concentrated line forces was given. With the increase of the rolling speed, the uncertainty in excitation makes the dispersion of the equivalent radiated sound power more significant.

Chapter 7

Stochastic Analysis of Low-speed Uniformity of Tires

As previously mentioned, for practical applications, the distribution type of input parameters should be identified from the experimental data, and then establish the stochastic approximation of random parameters. In this work, based on the proposed deterministic tire model, the probabilistic characteristics of the RFV and RFV1H are estimated by the gPC expansion theory. The first step is to recognize the distribution type of the input uncertain parameters by using Pearson's model and to construct the generalized polynomials using the gPC expansion. As stated in Section 5.3.2, the unknown coefficients of the gPC expansion can be obtained by performing the PCM. Hence, the second step of the stochastic analysis is to reconstruct the collocation points, which are the parameter combinations as the input of the deterministic model. Each set of collocation points includes a vertical displacement and a reconstructed curve of the time-domain RRoc using the harmonic superposition method. Subsequently, the collocation points are generated from different sampling methods and the unknown coefficients in the gPC expansion are determined. At the end of this section, the effects of each factor and the results under different variance levels are discussed and validated by the comparison with a large amount of test data. The flow chart for the analysis of the low-speed uniformity using the coupled rigid-flexible ring model is shown in Fig. 7.1

7.1 Low-speed uniformity measurements for stochastic analysis

Tire uniformity measurements are conducted to detect the force variations in the axle during the rotational motion of tires. Each batch of tires requires comprehensive low-speed uniformity testing

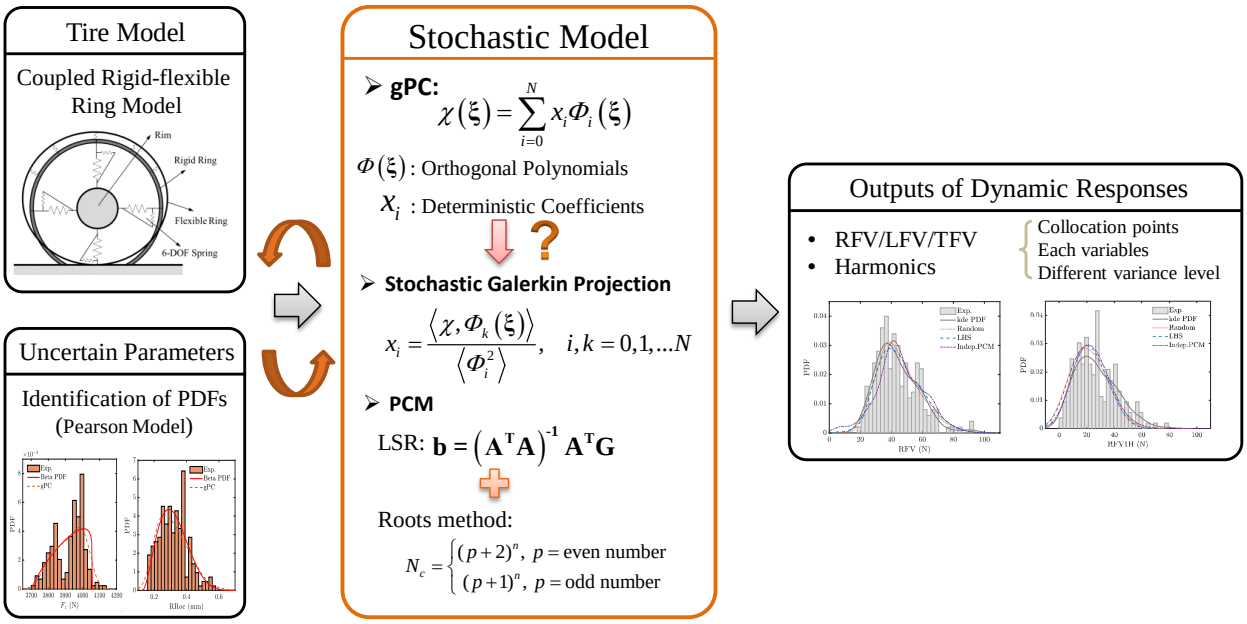

Figure 7.1: Flowchart of solving the coupled rigid-flexible ring model with uncertain parameters.

of the products before they are sold. The distribution of the low-speed uniformity index can also provide a reference for structural optimization and production process control of mass-produced tires. A uniformity testing machine is one of the most common pieces of equipment for examining the degree of tire non-uniformities nowadays. The tire to be tested is mounted on the spindle of the testing machine, and during the measurement process, the spindle and the drum are kept stationary by mechanical support, and their axes are positioned parallel to each other. The action of the ground is simulated by the rotating drum, which applies a certain load to the tire. This corresponds to the contact force provided by the road surface to the tires. The vibration from the tire rotation is transmitted to the drum, and the multi-phase force measurement sensors are fixed to the drum. Once the distance between the spindle axis and the drum axis is steady, the load sensor and the encoder at the bottom of the spindle measure the periodic changes in the RFV, TFV, and LFV of the tire.

The measurement implementation of tire uniformity on the high-speed uniformity (HSU) test machine is given in Section 4.1. Here, for the stochastic analysis, the measured amplitude values of the RRocs and their corresponding RFVs for the same batch consisting of 200 tires are obtained from the LSU test machine on the factory floor, which are the indicators for the uniformity testing program to be performed before sales. This set of data is applied for the identification of the distribution type of uncertain parameters. In addition, 1130 tires are measured for the validation of the stochastic analysis. The results are given in the model validation part in Section 7.4.3. The classification and usage of all uniformity measurement data are listed in Table 7.1.

Table 7.1: Classification and usage of the uniformity measurement data.

Number of tested tires	Type of data	Usage	Test equipment
1	Time traces of RRoc and RFV	1. Parameter identification; 2. GA-based optimization.	HSU Test Machine
2	Time traces of RRoc and RFV	1. Validation of the deterministic model.	HSU Test Machine
200	F_z, RRoc, RRoc1H RFV, RFV1H	1. Identification of distribution types; 2. Validation of stochastic analysis.	LSU Test Machine
1130	F_z, RRoc, RRoc1H RFV, RFV1H	Validation of the conclusions regarding 1. the effects of individual parameters and 2. different variance levels of uncertainties.	LSU Test Machine

7.2 Determination of parameter distribution type from experimental data

To carry out stochastic analysis, it is necessary to accurately know the distribution type of the given parameters from the experimental data. The fit to the samples can be achieved by applying the following general Pearson model [142, 143]. Pearson system provides a unique PDF for each uncertain parameter, including many typical PDF types (e.g., normal, beta, and gamma distributions). The estimation is carried out based on the 3$^{\text{rd}}$ and 4$^{\text{th}}$ central moments of the samples. The implementation of the Pearson framework to identify the PDF type of the experimental data only requires the calculation of the coefficients β_1 and β_2 related to the central moments. Assume that $f(\zeta_z)$ is the PDF of the standardized random variable ζ_z, which corresponds to the measurement data ζ. In this case, the Pearson model is expressed as

$$\frac{df(\zeta_z)}{d\zeta_z} = \frac{a+\zeta_z}{b_0+b_1\zeta_z+b_2\zeta_z^2} f(\zeta_z), \tag{7.142}$$

with

$$a = b_1 = \sqrt{\mu_2}\frac{(\beta_2+3)\sqrt{\beta_1}}{10\beta_2-12\beta_1-18}, \quad b_0 = \mu_2\frac{4\beta_2-3\beta_1}{10\beta_2-12\beta_1-18}, \quad b_2 = \frac{2\beta_2-3\beta_1-6}{10\beta_2-12\beta_1-18}, \tag{7.143}$$

where ζ_z is the standardized random variable, $\zeta_z = (\zeta - \mu_\zeta)/\sigma_\zeta$; μ_ζ represents the mean value, and σ_ζ denotes the standard deviation. The Pearson system is used to illustrate various distribution types in terms of the skewness $\beta_1^2 = \mu_3^2/\mu_2^3$ and the kurtosis $\beta_2 = \mu_4/\mu_2^2$, in which μ_k is the k^{th} statistic central moment. The Pearson family curves and the corresponding distribution types are shown in Appendix C.2.

For the stochastic analysis of the RFV, the distribution type of three input parameters, including the vertical load, the RRoc, and the first harmonic of the RRoc (RRoc1H), are identified. The identified sample consists of 200 measurements. For each parameter, the respective β_1^2 and β_2^2 are calculated and compared with the Pearson family curves to obtain the distribution type. The estimation of these three parameters is shown in Fig. 7.2. Although the distribution types defined by a boundary line, such as Type V and Type III, are presented in the figure, the point corresponding to β_1^2 and β_2^2 calculated from a set of experimental data is hardly located on a line. Therefore, the only distribution types that can be considered are Types I, VI, and IV, which are defined by regions. It is found that all uncertain parameters are distributed according to Type I, i.e., beta distribution [149]. The probability density function of the beta distribution is shown as

$$f(x;\alpha,\beta) = \frac{1}{\mathrm{B}(\alpha,\beta)} x^{\alpha-1}(1-x)^{\beta-1}, (\alpha,\beta) > 0, \tag{7.144}$$

where $\mathrm{B}(\alpha,\beta)$ is the beta function, and (α,β) are the shape parameters. The histograms of the test data and the fitted PDF are given in Fig. 7.3, and the shape parameters of the identified beta distribution are shown in Table 7.2. Based on the identified distributions, Jacobi polynomials are selected as the basis functions for the gPC expansion [139], see in Appendix C.1.

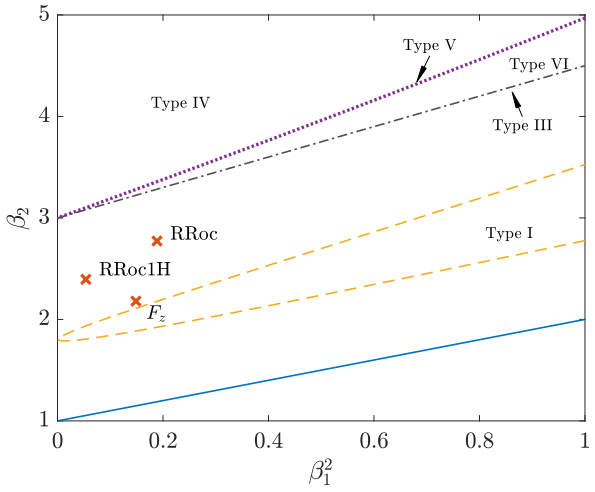

Figure 7.2: The identified distribution type for the measured input data on the Pearson system.

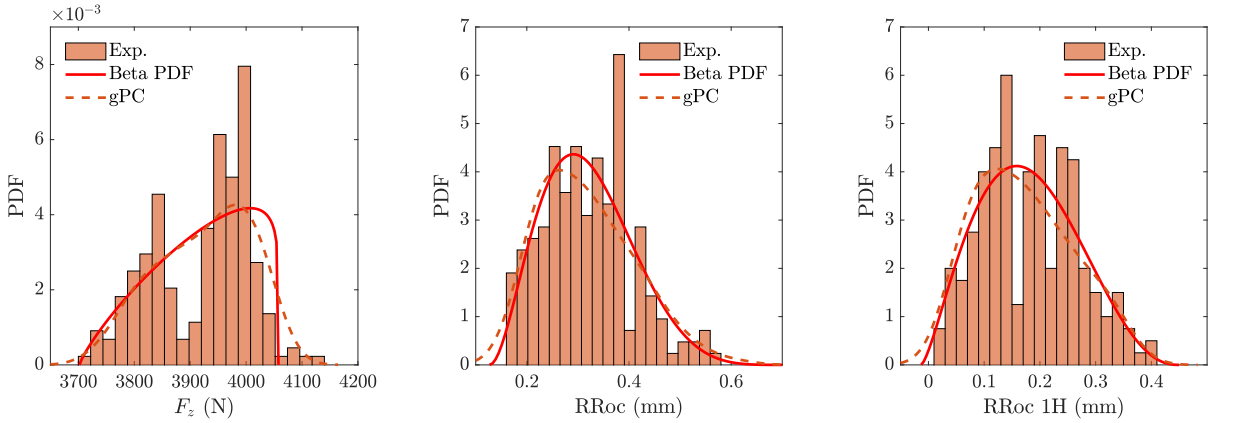

(a) Vertical load (F_z).

(b) Radial run-out of the center-point (RRoc).

(c) The first harmonic of the radial run-outof the center-point (RRoc1H).

Figure 7.3: The identified PDF of the input parameters, including F_z, RRoc, and RRoc1H.

Table 7.2: Shape parameters of the beta distributions of the random input variables.

	Mean value μ_ξ	Standard deviation σ_ξ	Shape parameters α	Shape parameters β
F_z	3921.5	86.856	1.83	1.14
RRoc	0.3207	0.0877	2.99	6.32
RRoc1H	0.1788	0.0870	2.43	3.44

7.3 Construction of collocation points

According to the theory of stochastic analysis illustrated in Section 3, to evaluate the coefficients in the gPC expansion Eq. (5.135) by implementing the PCM, a sufficient number of collocation points need to be selected. A set of collocation points contains three input parameters, i.e., the vertical load, RRoc, and RRoc1H. In order to obtain the response of the RFV, each set of collocation points needs to be converted into a form that can be called in the deterministic model. Therefore, the vertical load should be converted into the equivalent vertical deflection, and the given amplitudes of the RRoc and RRoc1H should be utilized to reconstruct a random time trace of the radius deviation in one period by using the harmonic superposition method.

In the method of gPC expansion, the dimension of the standard random variable $\boldsymbol{\zeta}$ indicates the number of different random sources in the system. The two random variables considered in this paper with correlation are the RRoc and RRoc1H. Therefore, it is considered that these two random variables have the same random sources in the tire structure, i.e., these two sets of random variables

correspond to the same random variable ζ_i in the standard random space. Once the collocation points are generated in the standard random space, two sets of collocation points in the physical space are created respectively by using the probability density functions of RRoc and RRoc1H. Then, the corresponding curves of radial runouts are generated.

Vertical loads

For a specific tire structure and dimension, the proposed contact model can accurately establish the deflection-force relation in the vertical direction, which was validated by the radial stiffness measurements (in Section 3.4.1). Because there is a unique deflection associated with each value of the vertical contact force, the overall vertical displacement under a specified load can be derived by interpolating the deflection-force curve. It will be used as the input of the coupled rigid-flexible ring model afterward.

Reconstruction of time-domain RRoc curves

Considering the application conditions of the ring model, it is necessary to construct a time-domain curve of the RRoc before performing the stochastic analysis. Since the fluctuations of the radius are continuous, in this section, the harmonic superposition method is adopted to construct the time-domain curve of RRoc. After specifying the maximum peak-to-peak values of the RRoc and RRoc1H, a continuous curve of a fluctuating radius in one period is constructed by superimposing the sinusoidal functions up to the 30^{th} order. The amplitude and phase of each order of the sinusoidal function are chosen randomly. When the error between the peak-to-peak values of the generated curve and the specified value, i.e., RRoc, is less than 1×10^{-4}mm, the reconstructed curve is assumed to fulfill the requirements. A set of recreated time-domain curves of RRoc is given in Fig. 7.4.

Once the vertical displacements and the RRoc curves are obtained, they are adopted as the input of the deterministic model corresponding to the collocation points. In combination with the PCM, the stochastic analysis of the non-uniformities of tires is carried out.

7.4 Numerical Results of stochastic analysis

Harmonic analysis is a very significant part of the testing process for tire uniformity. In this subsection, the distributions of RFV and RFV1H under the influence of the uncertain geometric parameters

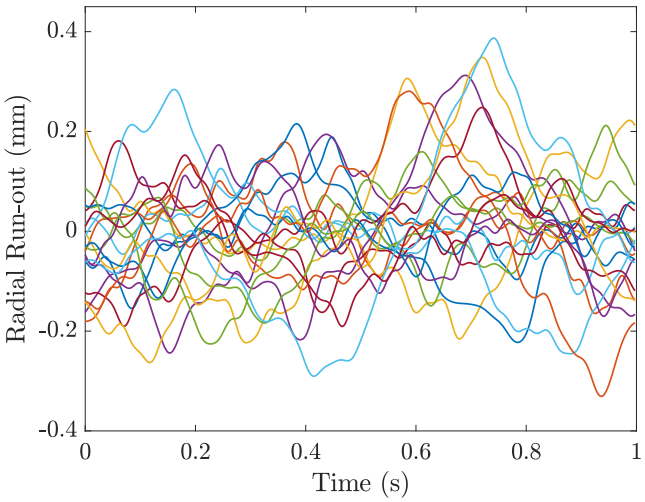

Figure 7.4: A set of reconstructed profile curves of RRoc.

of the tire and the vertical load are analyzed. Firstly, the convergence of different selection methods for the collocation points, i.e., random sampling, LHS, and the linear-independence-based roots method, is presented and compared with the MCS results. Furthermore, the numerical results are compared with the test data obtained on the test rig for 200 tires. The validity of the proposed stochastic analysis method is demonstrated. Then, based on the framework of the stochastic analysis, the effect of each input parameter on the RFV is estimated. Finally, the degree of dispersion of RFV at different variance levels is discussed. For some conclusions obtained from the parametric analysis, the test data of 1130 other tires are used for contrast and verification.

7.4.1 Prediction of RFV and RFV1H

A decisive step for gPC expansion is to solve the coefficients of the stochastic polynomial expansion. When a PCM is adopted, the number of collocation points should be larger than the number of undetermined coefficients. For instance, Isukapalli *et al.*[94] suggested that the number of collocation points should be twice the number of unknown coefficients. Then the least-squares regression can be employed to determine the coefficients. Unfortunately, sometimes even if the number of collocation points is more than four times the number of gPC coefficients, a satisfactory result is still not obtained. A sufficient number of collocation points theoretically ensures the precision of the simulation. However, it results in lower computational efficiency and may even be more computationally intensive than MCS. It is seen that the selection of collocation points significantly affects the computational efficiency and accuracy of the results of gPC expansion.

Therefore, three different sampling methods of the PCM (including the random sampling, the LHS,

and the linear-independence-based roots method) and MCS are applied in this paper to illustrate the impacts of the uncertain parameters on the RFV and its harmonics. The efficiency and accuracy differences due to these different sampling methods are analyzed. First, the random variables are estimated on the basis of the gPC expansion theory. In this case study, a 5^{th}-order gPC expansion is made to approximate the output response, of which the coefficients are derived by the PCMs. The traditional MCS is applied as a reference for computational efficiency and accuracy in stochastic analysis. Fig. 7.5 shows a comparison between the simulation results of the MCS and PCMs and the test data of RFV and RFV1H, which proves the validity of the gPC-based theoretical framework established in the previous section.

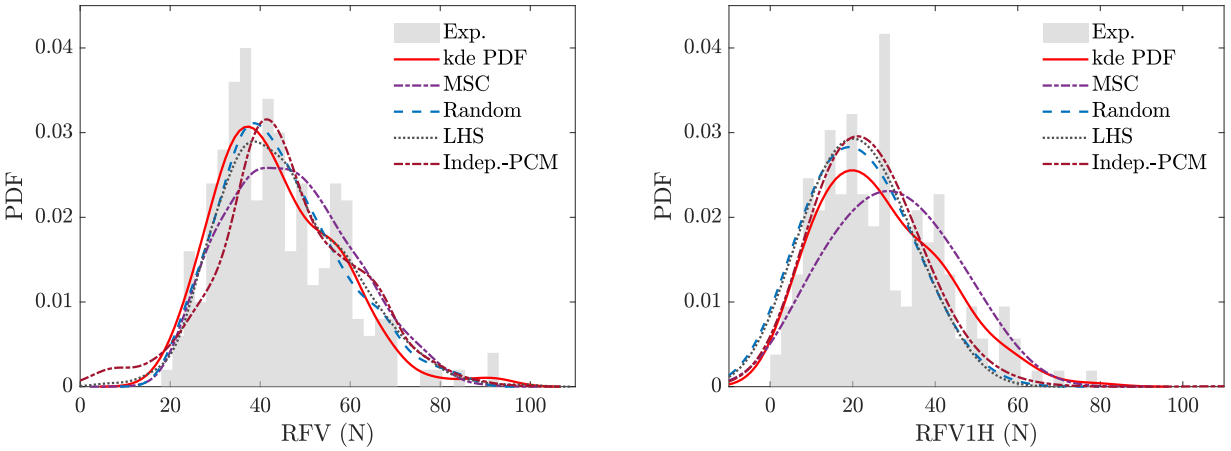

(a) Radial force variation (RFV).

(b) The first harmonic of the radial force variation (RFV1H).

Figure 7.5: Comparison between the simulated results using the MCS and PCMs and the measurement data of RFV and RFV1H.

7.4.2 Discussion of the selection of collocation points

1. Comparison between random sampling and LHS

The effective selection of the collocation points should be discussed before performing an extensive stochastic simulation. In this study, the number of coefficients to be determined N is 21. The computational efficiency of the random sampling, the LHS, and the linear-independence-based roots method are discussed in terms of integer multiples of N. Figs. 7.6(a) and (b) present a comparative plot of the results with the different numbers of collocation points obtained by applying random sampling and LHS. It is observed that to achieve sufficient accuracy, the number of sample points required for random sampling N_R is 126. In comparison, the number required for LHS N_{LHS} is 84.

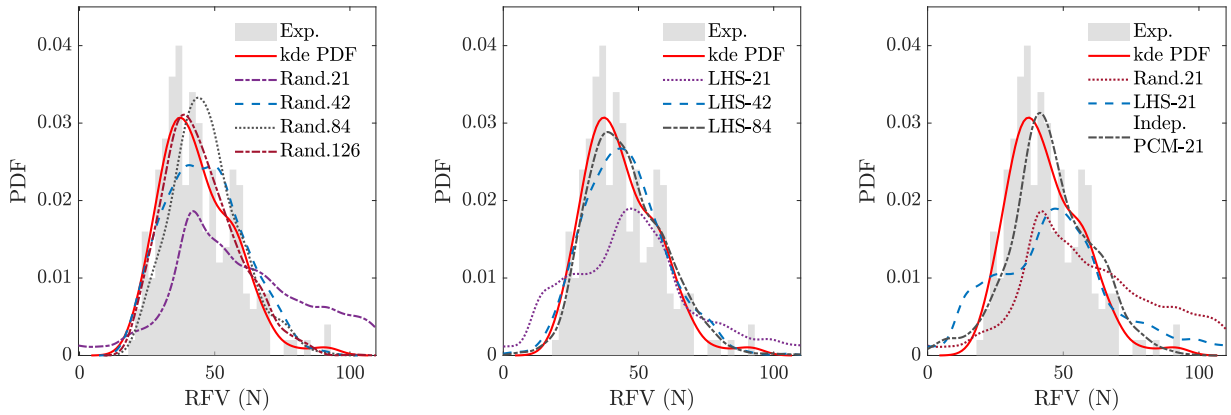

(a) Different numbers of collocation points obtained by applying random sampling.

(b) Different numbers of collocation points obtained by applying LHS.

(c) Different selection methods of collocation points with the same number of unknown coefficients.

Figure 7.6: Comparative plot of the RFV results with the different combinations of collocation points.

From this, it is suggested that the computational efficiency of the LHS technique for generating collocation points for the dynamic response analysis of tires is slightly higher than that of the random sampling method. However, the number of collocation points required for both is still much larger than N.

2. Efficiency of the linear-independence-based roots method

According to the linear-independence-based roots method proposed in the previous section, it can effectively generate a matrix of coefficients with a full row rank, i.e., the rank of the matrix $\mathbf{A}$ (in Eq. (5.138)) is exactly equal to the number of coefficients to be determined N. The prediction results of different selection methods when the number of collocation points is set to 21 are given in Fig. 7.6(c). It is clear that the improved collocation method has a significant advantage in terms of computational efficiency. Especially in the small sample condition, the linear-independence-based roots method shows good performance with higher precision than the traditional algorithms. Furthermore, the assignment of the collocation points depends on the type of random variables, the dimension of the random vector, and the order of the gPC expansion, which does not rely on the deterministic model. Therefore, a linear-independent examination can be carried out before the complete computational process.

The comparison of different collocation methods with 21 collocation points summarizing the simulation results of all the collocation point schemes is presented in Fig. 7.7 by means of box plots. A box plot easily provides a visual representation of summary statistics for a data sample and displays the comparison between the distribution of prediction results of a certain algorithm and

other models. In Fig. 7.7, the red dotted line shows the median of the experimental samples, which provides a reference line for the other prediction methods. Using this figure, it is possible to clearly distinguish the differences in the number of collocation points and their selection methods. As an example of the random sampling technique (all box plots in blue), with an increasing number of collocation points (from 21 to 126), the median of RFV is closer to the experimental value, and the distribution results of the data tend to converge. Similarly, cases with the same number of collocation points can be easily evaluated. When the numbers of collocation points generated by different selection methods are all 21, i.e., the group PCM21 in Fig. 7.7, it is found that the Indep-PCM method (yellow box plot) achieves significantly better prediction results than the random sampling method (blue box plot) and the LHS (orange box plot).

The errors of different PCMs are shown in Table 7.3. The results indicate the effectiveness of the PCM based on the linear-independence principle. The Indep-PCM does not lose much computational accuracy while reducing the amount of computational effort. For example, the error in the mean value of the RFV is only 3.9%, but the number of sample points generated by the linear-independent collocation technique is less than 1/6 of those generated by the random sampling method. It is noticed that even if 84 collocation points are selected by conventional LHS, the prediction accuracy of the mean value has not been significantly improved. The Indep-PCM is more efficient than the conventional PCM, especially compared with the MCS. As a result, the coefficients of the gPC expansion are calculated based on the Indep-PCM in the subsequent part.

A brief illustration of computational efficiency is given here. In fact, during the analysis flow of the PCMs, each set of collocation points is used as an input to the deterministic model. Therefore, the number of collocation points is the same as the number of calls to the deterministic model, i.e., the number of collocation points is proportional to the simulation time of the stochastic analysis. Moreover, the selection of collocation points is accomplished before the whole stochastic analysis. Once the distribution of the uncertain parameters and the order of the gPC expansion are determined, the collocation points are generated independently of the deterministic model. In this paper, the Indep-PCM method shows the highest accuracy with the same number of collocation points.

7.4.3 Impacts of each uncertain parameter

1. Impacts of F_z and RRoc

A specific situation when the uncertainty exists only in one parameter and the other input variables remain deterministic is considered. It is observed in Figs. 7.8(a) and (b) that the uncertainty of RRoc has a significant impact on the RFV and RFV1H of the tire. Obviously, the influence of the

Table 7.3: The mean values and variances of the estimated RFV by using different sampling methods.

	Number of collocation points	Mean value	Error of mean value (%)	Standard deviation	Error of standard deviation (%)
Measurement	-	43.77	-	13.46	-
MCS	2100	46.63	6.534	13.80	2.526
Random sampling	21	59.21	35.27	51.81	284.92
	42	46.44	6.102	14.44	7.286
	84	46.86	7.050	12.65	-5.964
	126	44.87	2.513	13.52	-0.413
LHS	21	57.55	31.48	45.38	237.2
	42	45.21	3.290	15.82	17.53
	84	45.65	4.295	14.76	9.66
PCM-Indep	21	45.49	3.922	15.25	13.30

uncertainty from the RRoc on the dispersion of the RFV is remarkably greater than that from the vertical load F_z. The results show that the separate uncertainty in F_z leads to a spike in the PDF of the RFV, where the response is mainly distributed around the deterministic value. This implies that the deviation of the test equipment does not greatly affect the RFV measurement results when the tire is assumed to be of an ideal structure. The dispersion of the RFV is mainly caused by the tire structure.

Moreover, the impact of the RRoc is still predominant in the analysis of RFV1H. However, compared to the prediction of the RFV, the effect of F_z starts to become more pronounced. There is also a bias from the peak value of the PDF caused by the RRoc. That suggests that both the geometric imperfections and the deviation of the vertical load lead to the dispersion of the harmonics of the RFV. It also indicates that the sources underlying the distribution of the harmonics are complex, and the major factors that affect each order of harmonics are not exactly the same.

Here, the conclusions drawn from the simulation model need to be verified by measurements. However, for the 200 sets of test tires applied for the identification of the uncertain parameters, the

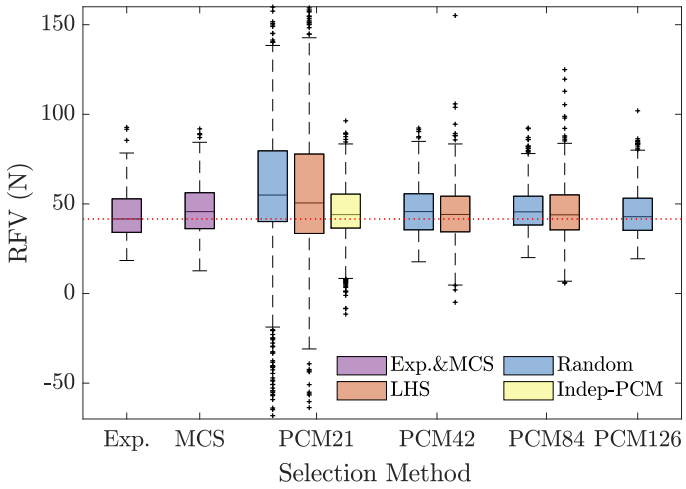

Figure 7.7: Boxplots of different selection methods of the collocation points. The line inside each box is the sample median, and the red dotted line shows the median of the experimental samples. (The number after the word “PCM" indicates the number of the collocation points.)

distributions of the vertical loads and the RRocs are uniquely determined. Thus, the data used for verification of the influence of each individual factor should have a different distribution of vertical loads and the RRocs than the test data of the 200 existing sets of tires. In fact, the results of this paper should be verified by adjusting the production process. This is intuitive. For example, by modifying the accuracy of the production and testing processes, it is possible to obtain a set of test loads and tire uniformity parameters that fit new distributions.

For simplicity, a large amount of tire test data is directly selected to examine the findings presented in this section. The validation is carried out using the test data from 1130 other tires of the same type and size. It is always possible to generate new distributions of uncertain parameters by selecting among these 1130 tires so as to simulate the results of production process control. Based on the results from the simulation, it is expected to screen a sample set from 1130 tires whose distribution of vertical loads is significantly different from that of the 200 tires, while their RRoc distribution is as identical as possible. If the predictions are correct, then the effect of the vertical load will be minor, and the results for the two sets of RFV and RFV1H should be determined by RRoc, i.e., their distributions should be as close as possible.

Therefore, there are 929 sets of samples selected from the 1130 tires by using the acceptance-rejection sampling method so that their distribution is as identical as possible to the beta distribution of the 200 modeling sets. Compared with the 200 modeling data, the distribution of the vertical load F_z of these samples is more concentrated, which can be used to check the impacts of different factors on the RFV. As mentioned before, with the same distribution of the RRoc, this data selection

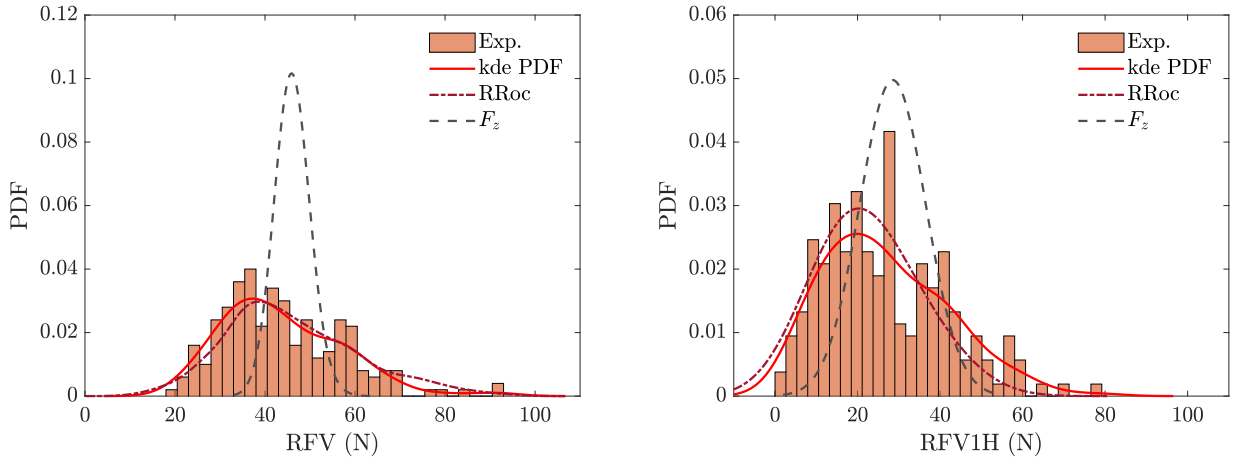

(a) Radial force variation (RFV).

(b) The first harmonic of the radial force variation (RFV1H).

Figure 7.8: Individual impact of each parameter (F_z and RRoc) on the RFV.

can verify whether the responses of the RFV and RFV1H for a large number of tires are consistent with the inferences drawn in this subsection. The distributions of F_z and RRoc for the selected test samples are given in Fig. 7.9. It is observed that the distribution of F_z is more concentrated for the selected data (Fig. 7.9(a)), while RRoc keeps the same beta distribution as much as possible (Fig. 7.9(b)). The corresponding results for the RFV and RFV1H are shown in Fig. 7.9(c) and (d), where it is seen that even though the variances of the distributions of F_z are significantly different, the RFV and RFV1H have not produced a large discrepancy. In contrast, RRoc is the factor that accounts for a more dominant influence. It is in agreement with the conclusions obtained from the simulation.

2. Discussion of RRoc1H

Since it is necessary to provide the input values of the RRoc and RRoc1H when generating the outer profile of the tire, an assumption is taken for a particular condition in this section. When the information about the distribution of the RRoc1H is incomplete, it is supposed that the data is a set with the same distribution as RRoc. The computational results, in this case, are shown in Fig. 7.10. With such an assumption, the prediction of the RFV1H presents a large deviation from the original measurement. It also indirectly points out that RRoc1H is a principal component impacting RFV1H. Hence, it is essential to take into account the distribution of RRoc1H when reconstructing the run-out curves.

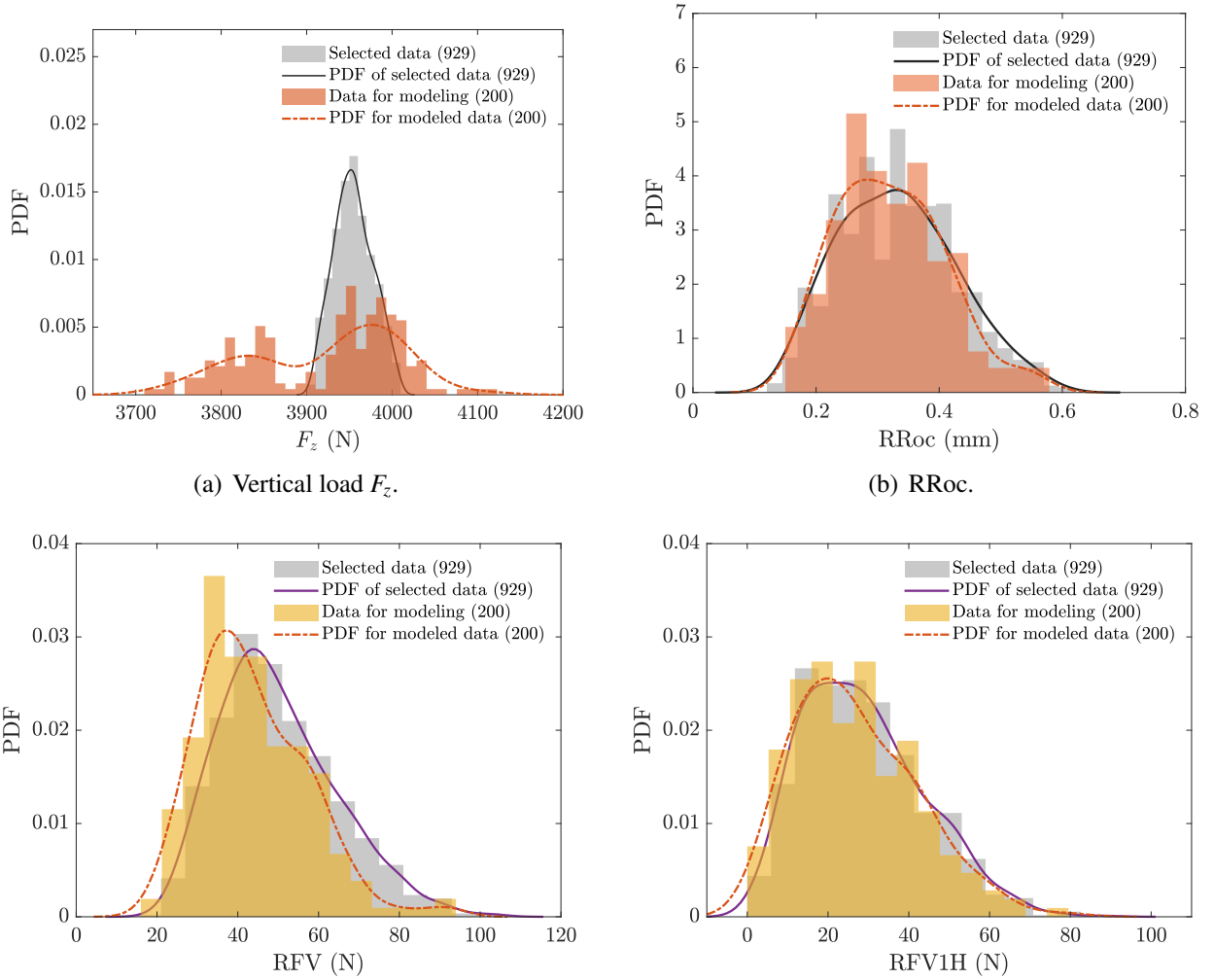

(a) Vertical load F_z.

(b) RRoc.

(c) Radial force variation (RFV).

(d) The first harmonic of the radial force variation (RFV1H).

Figure 7.9: Comparison between the modeling data (orange) and the 929 sets of test samples, which are selected from the 1130 sets of tires (gray).

7.4.4 Impacts of the variance level of uncertainties

In this section, the impacts of the level of uncertainties in the model parameters on the RFV are investigated. The original distribution shape of the uncertain parameters is kept the same, but their range of values is changed from 90% to 60% of the original range. As shown in Fig. 7.11, the corresponding dynamic response is more dispersed as the uncertain level of the geometric defects and the vertical load increase. Observing the response of RFV1H, the dispersion can be obviously improved by keeping the input parameters at 90% of the original distribution interval. However, further concentration of the parameters does not yield a corresponding improvement in the dispersion of the response.

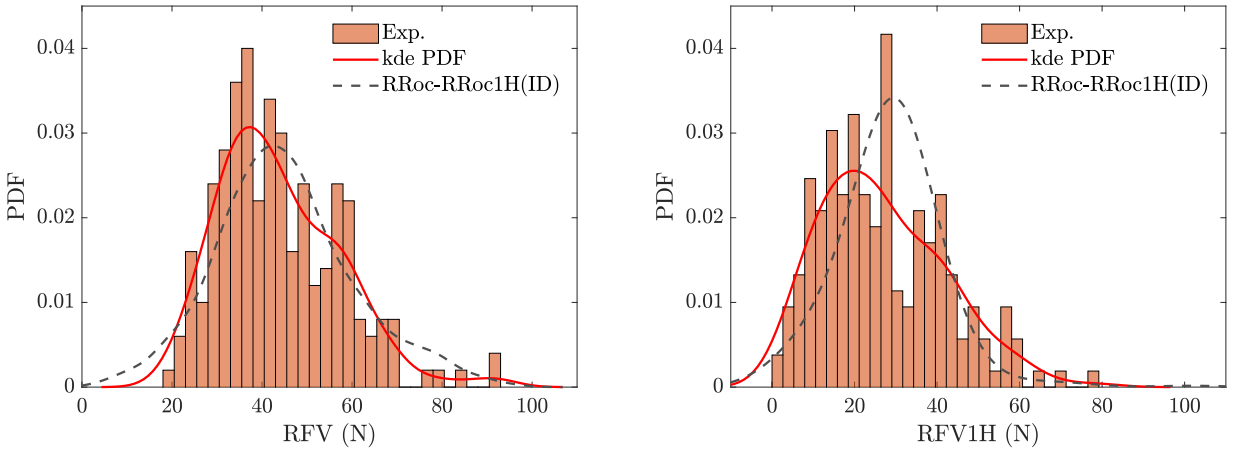

(a) Radial force variation (RFV).

(b) The first harmonic of the radial force variation (RFV1H).

Figure 7.10: Simulated results under the assumption that the RRoc1H has the same distribution as the corresponding RRoc.

The conclusions in this section are also validated by a large amount of test data. For simplicity, this study simulates the results of the production process control by selecting among these 1130 tires. For instance, a smaller interval of the RRoc distribution represents an optimization of the production process, which means that some tires with a larger radial run-out will not be produced. This process is implemented by selecting among 1130 tires, i.e., reserving the samples with smaller RRoc and comparing the test results of their corresponding RFVs with the model predictions. The samples of the RRoc with different distribution intervals are selected from 1130 tires, and the corresponding statistics for RFV and RFV1H are calculated. The results based on a large amount of test data are presented in Fig. 7.12. As an example, the distributions of RFV in the original distribution interval and in 60% of the interval of the original data are shown in Fig. 7.12(a). For other distribution intervals, the results are similar. Therefore, a comparison of the statistics, i.e., the mean value and standard deviation, with the predicted results of the proposed method are directly given in Figs. 7.12(b)-(d).

Apparently, when the mean value of the RRoc is kept constant, the RFV and RFV1H do not vary with the uncertainty level of the input parameters. This is demonstrated in the predicted results and the test data. For the standard deviation that is of greater concern, both RFV and RFV1H yield no significant concentration even when the input distribution interval of RRoc has been reduced to 80% of the original one. Only when the distribution interval of RRoc is further decreased are the distributions of RFV and RFV1H better controlled. Although there have been some deviations in the prediction of the values, the trends of the variations are predicted accurately. These errors probably

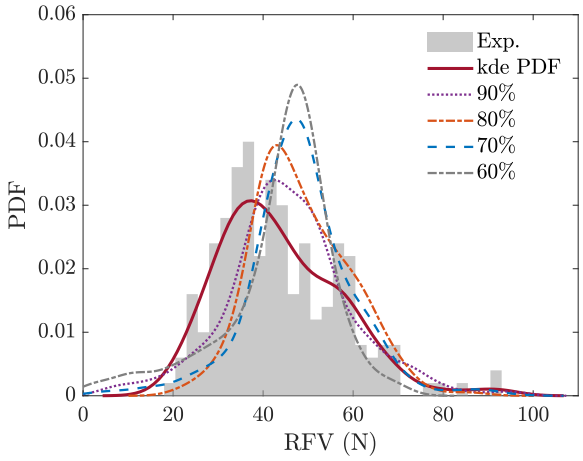

(a) Radial force variation (RFV).

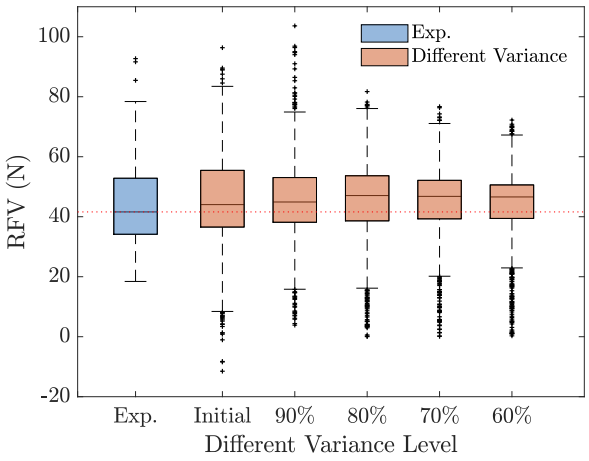

(b) Boxplots of RFV - all variance levels.

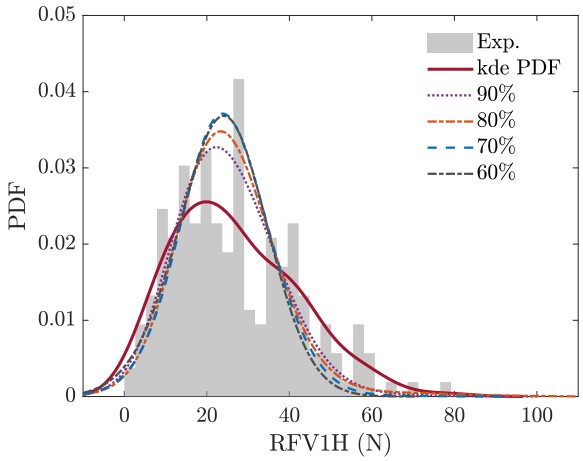

(c) The first harmonic of the radial force variation (RFV1H).

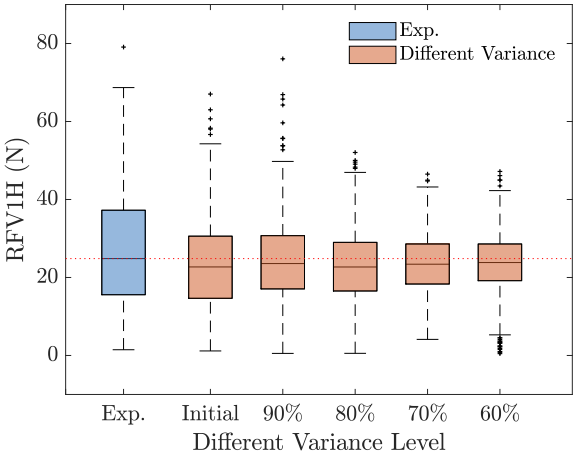

(d) Boxplots of RFV1H - all variance levels.

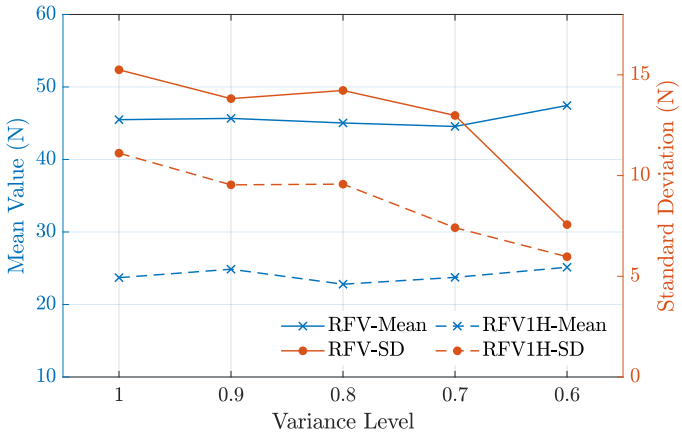

(e) Mean values and standard deviations of the RFVs and the RFV1Hs.

Figure 7.11: Simulation of the impacts under different variance levels of uncertainties in the uncertain parameters on the RFVs and RFV1Hs.

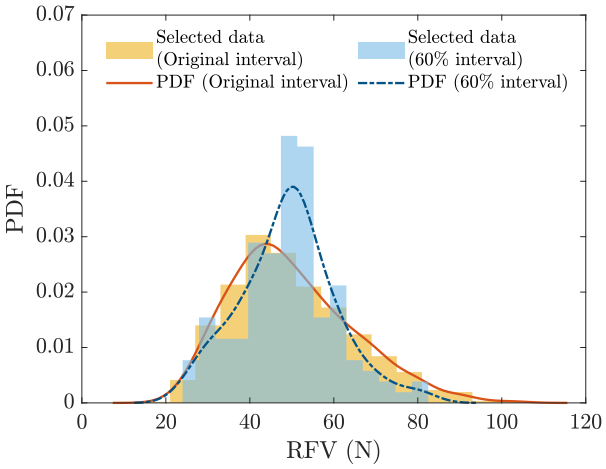

(a) The PDF of the corresponding RFVs for the different distribution intervals of RRoc (original and 60 variances%).

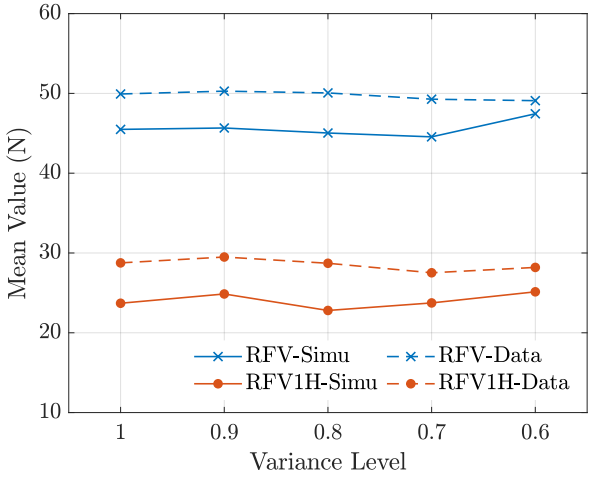

(b) Mean value of the RFV and RFV1H.

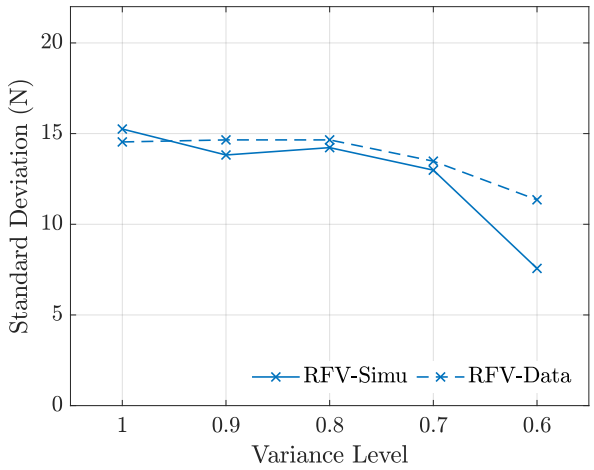

(c) Standard deviation of the RFVs.

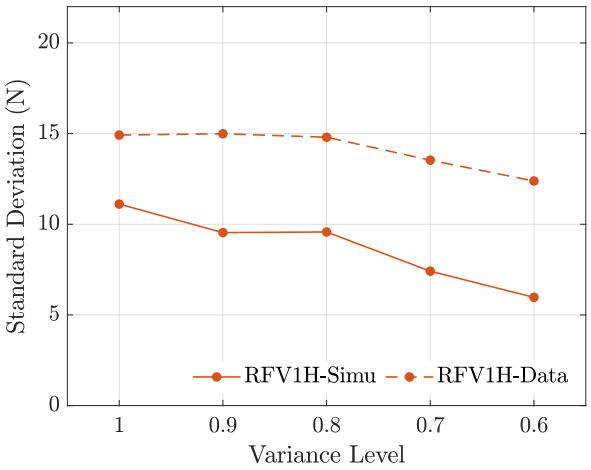

(d) Standard deviation of the RFV1Hs.

Figure 7.12: Comparison between the predicted results of RFV and RFV1H at different variance levels and a large number of test data.

result from the uncertainties of other structural parameters of the tires, which are not considered in the model proposed in this paper, for example, the uneven distribution of tread stiffness, the radial dimensional run-out in the width direction, etc.

7.5 Summary

This chapter discussed the quantification of the uniformity parameters on the dynamic response of the tire. The prediction of the distribution of the RFV is presented by implementing the gPC expansion, and the computational efficiency of the PCM with different sampling methods is investigated. Finally, considering the uncertainty in the vertical load and the geometric imperfection individually, the effects of different parameters and variance levels on the distribution of the responses are estimated and compared with a large number of measurements.

In the stochastic analysis, the influences of the uncertainties in the vertical load and the geometric defects on the radial force variation were estimated by implementing the gPC expansion theory. The distribution types of the vertical load, the radial run-out of the center-point (RRoc), and the first harmonic of the radial run-out of the center-point (RRoc1H) were identified as beta distributions based on the measurement results of 200 tested tires using the Pearson model. Then, the expression of gPC expansion for the corresponding output response was constructed in terms of the tensor product. A non-intrusive probabilistic collocation method was adopted to obtain the unknown coefficients of the gPC expansion of the radial force variation and its first harmonic. Using the concept of linear independence of vectors, the number of selected collocation points was minimized by considering different methods of construction of the collocation points. This yielded an effective simulation in terms of computational cost. To generate collocation points, the reconstruction methods for the vertical load and the profile curves with geometric defects were developed for the deterministic model.

The numerical results of the radial force variation and its first harmonic induced by the uncertain structural parameters were compared with extensive measurement data from 1130 tires and Monte Carlo simulations, which confirm the validity of the proposed stochastic analysis. For the individual impact of each parameter, it was found that the deviation from the testing equipment has a minor effect on the measurements of radial force variations, whereas the dispersion of the force is predominantly caused by geometric defects. Furthermore, with the increase in the uncertainties of the geometric defects and the vertical load, more scattered distributions of the dynamic response are exhibited. Yet a further concentration of the parameters does not produce a corresponding improvement in the dispersion of the radial force variation.

Chapter 8

Conclusion and Outlooks

8.1 Summary

From the motivation, based on the theory of the ring model of tire dynamics, a novel theoretical model is presented to describe the in-plane and out-of-plane vibrations, the steady-state response, and the dynamic response characteristics of tires. Then, it has been extended to evaluate the influence of uncertainties in the structural, material, and geometric parameters on the natural frequencies and tire uniformity.

This study first gives the theoretical derivation of a three-dimensional flexible ring model. It extended the existing ring models to the out-of-plane vibration and the steady-state response analysis. Herein, the Hamilton principle is adopted to derive the governing equations. The accuracy of the model is then evaluated by the deterministic prediction of the natural frequencies and the steady-state response of a tire. A simplified scale, the equivalent radiated sound power, is adopted to describe the overall steady deformation characteristics of the tire. The results are in good agreement with the solution given in the literature [44] and the experimental results in [32].

Considering the practical operating conditions of tires, the proposed tire model should be capable of analyzing the transient response. In this thesis, a new theoretical model is developed to evaluate the characteristics of the dynamic responses of tires, which is also used to analyze the transmission mechanism of the radial force at the spindle due to road unevenness and geometric defects in tires. Based on the theory of the tire ring models, a coupled rigid-flexible ring model is presented. By simplifying the three-dimensional ring model into a two-dimensional model, the in-plane dynamic responses of the tire are analyzed. A contact algorithm based on the flexible ring provides a pressure distribution on the tire-road contact patch and the length of the footprint under different vertical

loads. The dynamic responses are then represented by combining the rigid ring model with the flexible ring model. Further, the identification of model parameters and the optimization approach by utilizing the test data are given. The accuracy of the contact algorithm and the transient responses are validated against experimental radial stiffness and over-cleat tests, respectively. In addition, this model is extended to the analysis of the low-speed uniformity of tires with geometric defects and verified experimentally. It indicates that the novel proposed model offers many application scenarios and extension possibilities.

How to control tire non-uniformities has always been a core issue for tire manufacturers. Considering the uncertain structural and geometric parameters induced by the manufacturing process of tires, the developed deterministic model is combined with the gPC expansion theory to estimate the impacts of parameter uncertainties on the dynamic response. In order to investigate the impacts of structural imperfections, the gPC theory and the probabilistic collocation method are briefly introduced, respectively. Then a practical tire is applied to be modeled. The impacts of the elastic and structural uncertainties on the natural frequencies of the tire are first investigated in this thesis. The uncertain parameters and the desired responses are approximated by using the truncated gPC expansions having a random orthogonal basis. The probabilistic collocation method is employed to obtain the deterministic coefficients in the gPC expansions. Based on the concept of linear independence of vectors, the number of selected collocation points is significantly reduced. This technique is applied to investigate the influences of elastic and structural uncertainties on the natural frequencies of the tire. It yields an efficient simulation for the stochastic dynamic analysis of the ring model. The numerical results are in good agreement with the MCSs. Additionally, this thesis also describes the distributions of the sound power due to the forced vibrations under the uncertainty in the external force terms.

Furthermore, this study implemented a stochastic prediction of low-speed uniformity of tires, which is applied for the optimization of manufacturing processes and quality evaluation before the mass production and the marketing process. the coupled rigid-flexible ring model is extended to the stochastic analysis of the in-plane dynamic response characteristics owing to the geometric non-uniformities of the tire. For the prediction of the production quality for a significant number of tires, the influence of the uncertainty of geometric defects on the RFV and its first harmonic is thoroughly discussed. The computational efficiencies of MCSs, PCMs, and 200 sets of measurement data are compared. Also, the results are illustrated for the individual effects of each parameter. Finally, the distributions of the responses under different variances of the uncertain inputs are given. Through the validation by using extensive experimental data (1130 sets), it is evident that the proposed technique achieves an effective prediction for the low-speed uniformity of the mass of tires so as to

provide guidance for production optimization before the products are shipped.

8.2 Primary contributions of the thesis

This thesis studies the tire modeling problem of the three-dimensional vibration, dynamic responses, and uniformity analysis. The proposed model is applied to the uncertainty quantification of the responses caused by the structural and geometric imperfections of tires. The primary contributions of this thesis mainly include the following two aspects, which are tire modeling and its application in uncertainty quantification.

1. Tire modeling

    a) Three-dimensional flexible ring model

    A novel three-dimensional ring model for the free vibration and steady-state response of a tire (has been proposed. Especially, the out-of-plane deformation had been completely discussed. Additionally, by relaxing the in-extensibility assumption and considering the out-of-plane deformation, the analytical expression of the steady-state response has been given. By comparing the solutions with the results proposed in the literature, it shows that, for a tire with high circumferential stiffness, the equations are simplified by using the assumption of in-extensibility without losing much precision, but some special modes (breathing mode) cannot be obtained due to the limitation of the deformation.

    The concept of equivalent radiated sound power has been introduced to evaluate the overall vibrating velocity of the ring surface, consisting of the in-plane and out-of-plane bending and lateral torsion. From the foregoing analysis, it is found that the rolling speed results in a mode splitting. However, this splitting due to rotation does not apply for the 0^{th}-order natural frequencies.

    b) Coupled rigid-flexible ring model

    In this study, a theoretical model has been developed to evaluate the characteristics of the in-plane dynamic responses of tires and analyze the transient responses at the spindle on the uneven road surface. A contact algorithm based on the 2D flexible ring provides a pressure distribution on the tire-road contact patch and the length of the footprint under different vertical loads. The comparison of the static radial stiffness between the experimental data and the simulated results demonstrates the theoretical basis and rationality of the flexible ring model as an approximation for the steady-state

deformation and tire-road contact. The transient dynamic response is then estimated by combining the rigid ring model with the flexible ring model. The applicability of the model in the simulation of transient response has been validated by the experimental data of over-cleat tests at different speeds and different vertical loads. In this way, the proposed new method has the merits of both high accuracy up to 150Hz and low computing cost.

Further, the identification of model parameters based on the static stiffness measurements and the over-cleat test, and the optimization approach have been given. The nonlinear least-squares method has been adopted to determine the physical parameters of a specific tire in this work, and a set of measured data of the static stiffness and the over-cleat responses has been chosen as the performance index of the identification algorithm.

In addition, this model has been extended to the analysis of low-speed uniformity of tires with geometric defects and has been validated experimentally. For the uniformity analysis of tires, the GA has been adopted to determine the physical parameters of a specific tire, and a set of RFV has been chosen as the performance index of the simulated algorithm. The impacts of the geometric imperfection have been evaluated in the proposed model. It has been found that a small amplitude fluctuation of the RRoc can lead to a large variation of the steady-state vertical contact force. Moreover, the filtering effect of the tire structure on the RRoc has been shown, which includes the influence of the elasticity of the material and the geometric construction. The time-domain analysis shows that the RRoc is the most dominant factor affecting the RFV at low speed. By comparing the simulation result with the experimental data, it can be stated that the developed model adequately evaluates the amplitude and peak positions of the RFV. Furthermore, the one-sided amplitude spectrum and the power spectrum of the RFV simulation results have been accurately predicted. The accuracy and reliability of the extended method based on the coupled rigid-flexible ring model have been validated in the low-speed uniformity analysis for the tires with geometric defects. It indicates that the novel proposed model offers many application scenarios and extension possibilities.

2. Applications in uncertainty quantification

   a) Natural frequencies and steady-state response

   The gPC expansion method has been applied to estimate the influence of uncertainties. The non-intrusive PCM has been employed to obtain the unknown coefficients of the gPC expansion of the natural frequencies and the equivalent radiated sound power.

Considering the concept of linear independence of vectors, the number of selected collocation points has been reduced as much as possible. This approach yields an efficient simulation in terms of computational costs.

The numerical result of the natural frequencies due to uncertain structural parameters has been compared with the MCSs, which confirms the effectiveness of the proposed stochastic analysis. It indicates that the uncertain material and structural parameters affect each natural frequency. The membrane stiffness EA has a significant influence on the breathing mode of a tire. Furthermore, the sound power due to the forced vibrations under random concentrated line forces has been estimated. With the increase of the rolling speed, the uncertainty in excitation makes the dispersion of the equivalent radiated sound power more significant.

b) Low-speed uniformity

In the stochastic analysis, the influences of the uncertainties in the vertical load and the geometric defects on the RFV have been estimated by implementing the gPC expansion theory. The distribution types of the vertical load, the RRoc, and the RRoc1H have been identified by the Pearson model. Then, the expressions of gPC expansion for the corresponding output response have been constructed in terms of the tensor product. A non-intrusive PCM has been adopted to obtain the unknown coefficients of the gPC expansion of the RFV and RFV1H. Employing the concept of linear independence of vectors, the number of selected collocation points has been minimized by considering different methods of construction of the collocation points. It yields an effective simulation in terms of computational cost. To generate collocation points, the reconstruction methods for the vertical load and the profile curves with geometric defects have been developed for the deterministic model.

Numerical results of the RFV and RFV1H induced by the uncertain structural parameters have been compared with extensive measurement data and MCSs, which confirm the validity of the proposed stochastic analysis. For the individual impact of each parameter, it is found that the deviation from the testing equipment has a minor effect on the RFV measurements, whereas the RFV dispersion is predominantly caused by geometric defects. Furthermore, with the increase in the uncertainties of the geometric defects and the vertical load, more scattered distributions of the dynamic response are exhibited. Yet, a further concentration of the parameters does not produce a corresponding improvement in the dispersion of the RFV.

8.3 Shortcomings

Although the proposed models and the algorithms for uncertainty quantification achieved the above contributions, there still exist some shortcomings that should be paid attention to in future work.

First, in Chapter 2, the developed three-dimensional flexible ring model has been only studied by considering the damping effect existing in the sidewall. However, the viscoelastic effect of the rubber is always existed, which has not been introduced in this model. In addition, the composite structure of the belt and tire body, i.e., a rubber-cord structure, has not been considered in this work. In this case, these material and structural properties should be modeled in the description of tire dynamics.

Second, in Chapter 3, a new model has been developed to analyze the dynamic responses of tires. Indeed, it achieves the desired performance in in-plane dynamics and the description of the radial run-outs, but another significant aspect, i.e., the out-of-plane dynamics such as lateral dynamics, steering, camber, etc., has not been modeled and discussed. There is no doubt that an overall simulation for handling stability and riding comfort is complex and challenging.

Third, in Chapter 4, the model proposed in this work can be taken as a theoretical basis for diverse tire analyses. One possible outlook is to continuously improve the impacts of uniformity parameters, such as the high-speed uniformity analysis, in which mass imbalance is a critical factor. The resonance effect of tire rotation can significantly affect the riding comfort of the vehicle, which has not been considered in this thesis.

At last, in Chapters 6 & 7, the applications in the uncertainty quantification of natural frequencies and the low-speed uniformity have been proposed. It is meaningful to investigate the impacts of the structural, material, or geometric uncertainties. However, it is not always suitable to assume that the random variables are independent. The correlation or dependence between these random variables should be evaluated and further introduced into the algorithm.

8.4 Outlooks for further research

1. Involve the nonlinear stiffness of tires in the model

   Structure, geometry, and material distribution should be simultaneously considered in a tire dynamics model. The tire model established in this thesis has simplified the sidewall as a set of linear radial and tangential springs. In practical conditions, the stiffness of the tire sidewall is nonlinear and exhibits viscoelastic properties because of rubber [53, 130, 150].

Compared with the geometry of the tire, the deformation is small so that the sidewall stiffness can be linearized. However, under a heavy vertical load or under an operating condition with a large slip or camber angle, the loads applied on the tire will change the values of the static and dynamic stiffness of the sidewall due to non-linearity, although to some extent the linear model will still be valid in a small deviation range of the deformation. Therefore, in future work, the non-linearity and viscoelastic properties should be involved in the modeling process of tire dynamics. We hope that it will have a more accurate performance in the large deformation problems of tires. Notably, a further-developed model should have an overall promising balance between precision and computational costs.

2. Derive a new tire-road contact model

   Ideally, a tire model should be applicable in different operating conditions. In this thesis, the tire-road contact algorithm only deals with a free-rolling tire on road surfaces. The method proposed in Chapter 3 can be further developed to solve the responses of braking or driving tires. To achieve that objective, two issues need to be discussed in detail. The first one is that the tire-road contact model should have the ability to capture the relationship between the longitudinal force and the slipping ratio in the contact area. While the concept of the relaxation length has been introduced into this model, the assumption that the relaxation length is set as the half contact length is only suitable for the longitudinal slip within the linear region [14, 125]. Secondly, the equations of motion of tires should be combined with those of the rim or motor, so that the torque can be reflected and simulated in the tire-wheel assembly. As mentioned before, it may lead to large tire deformation, which needs the description of the non-linear characteristics of the sidewall stiffness.

3. High-speed uniformity (HSU)

   In the low-speed uniformity analysis, the rolling speed of a passenger tire is one revolution per minute, i.e., approximately 7km/h of test speed. However, in the high-speed uniformity measurement at 70km/h, the frequency of the first harmonic of radial force variation will be approximately 10Hz. Similarly, the second harmonic is 20Hz, etc. The frequency of each order harmonic will increase as the increased of rolling speed of the tire. At some specific speeds, the frequency of a harmonic will be close to the natural frequency of the tire and then excite resonance, where the amplitude of the force variation will dramatically increase.

   Therefore, the harmonics in the high-speed uniformity analysis usually receive greater attention than the overall force variations. To reduce the impacts of the internal tire non-uniformities, a theoretical model for high-speed uniformity analysis should establish the underlying correlation of the tire imperfections with one or more of the harmonics. Especially,

the mass imbalance will become a significant factor in the force variations with an increasing speed, of which the corresponding response is proportional to the square of the speed. It requires that the established model should reflect the higher-order natural frequency of tires, and has the ability to integrate the mass imbalance into the algorithm.

4. Correlation between uncertain variables

   At last, in Chapters 6 & 7, the simplified assumption that the uncertain variables are independent seems counterintuitive to the real tire structure, although it still generates a good agreement with the measurements. The uncertainties in the structural and geometric parameters of tires as well as the material distribution are usually correlated. There are several methods for solving the stochastic analysis with correlated variables, including the implementation of the copula-polynomial chaos expansion (copula-PCE) framework [151–154], decorrelation using Nataf transformations [155–159], application of the maximum entropy method [160, 161], etc. However, with the increasing number of uncertain parameters, it may lead to dimensional catastrophe. Sparse grid [137, 162], arbitrary sparse polynomial chaos expansion(ASPCE) [117, 163, 164], and principal component analysis (PCA) [165–167] can effectively solve this problem.

   In future work, according to the previous work of the deterministic model and the framework of uncertainty quantification, we will try to develop a novel stochastic model considering the correlated uncertain parameters, which can reinforce the description of the internal characteristics of the tire structure. In particular, when the model involves the mechanics of the rubber-cord composite structures of tires, the stiffness coefficients are inevitably coupled. Here, we expect a new algorithm to analyze the uncertainty in the tire dynamics and vibrations, which can go beyond the previous pure assumption of parametric independence in terms of algorithmic accuracy and adaptability.

Bibliography

[1] S. Uhlar, F. Heyder, and T. König, "Assessment of two physical tyre models in relation to their NVH performance up to 300 Hz," *Vehicle System Dynamics*, vol. 59, pp. 331–351, oct 2019.

[2] M. Demic, "The definition of the tires limit of admissible nonuniformity by using the vehicle vibratory model," *Vehicle System Dynamics*, vol. 31, no. 3, pp. 183–211, 1999.

[3] A. N. Gent and J. D. Walter, *Pneumatic Tire*. Mechanical Engineering Faculty Research. 854., 2006.

[4] J. Deng, J. Sun, and A. Li, "Analysis and optimization of vehicle interior noise caused by tire excitation," in *Proceedings of China SAE Congress 2018: Selected Papers* (C. S. o. A. E. (China SAE), ed.), (Singapore), pp. 723–735, Springer Singapore, 2020.

[5] C. Funfschilling and G. Perrin, "Uncertainty quantification in vehicle dynamics," *Vehicle System Dynamics*, vol. 57, no. 7, pp. 1062–1086, 2019.

[6] X. Chen, H. Lei, C. Zhang, and J. Liu, "Probability density evolution method for vehicle dynamics analysis under uncertainty," in *Proceedings of China SAE Congress 2018: Selected Papers* (C. S. o. A. E. (China SAE), ed.), (Singapore), pp. 243–256, Springer Singapore, 2020.

[7] M. Abe, *Vehicle handling dynamics: theory and application*. Butterworth-Heinemann, 2015.

[8] G. Gim, Y. Choi, and S. Kim, "A semiphysical tyre model for vehicle dynamics analysis of handling and braking," *Vehicle System Dynamics*, vol. 43, no. sup1, pp. 267–280, 2005.

[9] E. Denti and D. Fanteria, "Models of wheel contact dynamics: An analytical study on the in-plane transient responses of a brush model," *Vehicle System Dynamics*, vol. 34, no. 3, pp. 199–225, 2000.

[10] J. Deur, J. Asgari, and D. Hrovat, "A 3D brush-type dynamic tire friction model," *Vehicle System Dynamics*, vol. 42, no. 3, pp. 133–173, 2004.

[11] G. Mavros, H. Rahnejat, and P. King, "Transient analysis of tyre friction generation using a brush model with interconnected viscoelastic bristles," *Proceedings of the Institution of Mechanical Engineers, Part K: Journal of Multi-body Dynamics*, vol. 219, no. 3, pp. 275–283, 2005.

[12] H. Pacejka and I. Besselink, "Magic formula tyre model with transient properties," *Vehicle System Dynamics*, vol. 27, no. S1, pp. 234–249, 1997.

[13] H. B. Pacejka, *Tire and Vehicle Dynamics (Third Edition)*. Oxford: Butterworth-Heinemann, third ed., 2012.

[14] P. Zegelaar, *The dynamic response of tyres to brake torque variations and road unevennesses*. PhD thesis, Delft University of Technology, Netherlands, Mar. 1998.

[15] A. Schmeitz and J. Pauwelussen, "An efficient dynamic ride and handling tyre model for arbitrary road unevennesses," in *Reifen, Fahrwerk, Fahrbahn : Tagung Hannover, 18-19 Oktober 2001*, pp. 173–199, VDI-Verlag, 2001.

[16] M. Gipser, "FTire: a physically based application-oriented tyre model for use with detailed MBS and finite-element suspension models," *Vehicle System Dynamics*, vol. 43, no. sup1, pp. 76–91, 2005.

[17] M. Gipser, "Ftire–the tire simulation model for all applications related to vehicle dynamics," *Vehicle System Dynamics*, vol. 45, no. S1, pp. 139–151, 2007.

[18] C. Oertel, "On modeling contact and friction calculation of tyre response on uneven roads," *Vehicle System Dynamics*, vol. 27, no. S1, pp. 289–302, 1997.

[19] C. Oertel, "Eigensystem of tangential contact in tyre models," *Vehicle System Dynamics*, vol. 38, no. 4, pp. 245–260, 2002.

[20] S. K. Clark, "The rolling tire under load," in *SAE Technical Paper 650493*, SAE International, Feb. 1965.

[21] J. T. Tielking, "Plane vibration characteristics of a pneumatic tire model," in *SAE Technical Paper 650492*, SAE International, feb 1965.

[22] F. Böhm, "Mechanik des gürtelreifens," *Ingenieur-Archiv*, vol. 35, no. 2, pp. 82–101, 1966.

[23] L. Kung, W. Soedel, T. Yang, and L. Charek, "Natural frequencies and mode shapes of an automotive tire with interpretation and classification using 3-D computer graphics," *Journal of Sound and Vibration*, vol. 102, no. 3, pp. 329–346, 1985.

[24] L. Kung, W. Soedel, and T. Yang, "Free vibration of a pneumatic tire-wheel unit using a ring on an elastic foundation and a finite element model," *Journal of Sound and Vibration*, vol. 107, no. 2, pp. 181–194, 1986.

[25] G. Potts, C. Bell, L. Charek, and T. Roy, "Tire vibrations," *Tire Science and Technology*, vol. 5, no. 4, pp. 202–225, 1977.

[26] W. Soedel and M. Prasad, "Calculation of natural frequencies and modes of tires in road contact by utilizing eigenvalues of the axisymmetric non-contacting tire," *Journal of Sound and Vibration*, vol. 70, no. 4, pp. 573–584, 1980.

[27] M. Takayama and K. Yamagishi, "Simulation model of tire vibration," *Tire Science and Technology*, vol. 11, no. 1, pp. 38–49, 1983.

[28] S.-C. Huang and C.-K. Su, "In-plane dynamics of tires on the road based on an experimentally verified rolling ring model," *Vehicle System Dynamics*, vol. 21, no. 1, pp. 247–267, 1992.

[29] Y. Wei, L. Nasdala, and H. Rothert, "Analysis of forced transient response for rotating tires using ref models," *Journal of Sound and Vibration*, vol. 320, no. 1, pp. 145–162, 2009.

[30] C. Wang, B. Ayalew, T. Rhyne, S. Cron, and B. Dailliez, "Static analysis of a thick ring on a unilateral elastic foundation," *International Journal of Mechanical Sciences*, vol. 101-102, pp. 429–436, 2015.

[31] X. Yu, H. Huang, and T. Zhang, "A theoretical three-dimensional ring based model for tire high-order bending vibration," *Journal of Sound and Vibration*, vol. 459, p. 114820, 2019.

[32] Z. Liu, F. Zhou, C. Oertel, and Y. Wei, "Three-dimensional vibration of a ring with a noncircular cross-section on an elastic foundation," *Proceedings of the Institution of Mechanical Engineers, Part C: Journal of Mechanical Engineering Science*, vol. 232, no. 13, pp. 2381–2393, 2018.

[33] M. Matsubara, D. Tajiri, T. Ise, and S. Kawamura, "Vibrational response analysis of tires using a three-dimensional flexible ring-based model," *Journal of Sound and Vibration*, vol. 408, pp. 368–382, 2017.

[34] S. S. Rao and V. Sundararajan, "In-Plane Flexural Vibrations of Circular Rings," *Journal of Applied Mechanics*, vol. 36, pp. 620–625, 09 1969.

[35] D. A. Evensen, "Nonlinear Flexural Vibrations of Thin Circular Rings," *Journal of Applied Mechanics*, vol. 33, pp. 553–560, 09 1966.

[36] T. Gardner and C. Bert, "Vibration of shear deformable rings: Theory and experiment," *Journal of Sound and Vibration*, vol. 103, no. 4, pp. 549–565, 1985.

[37] J. Lin and W. Soedel, "On general in-plane vibrations of rotating thick and thin rings," *Journal of Sound and Vibration*, vol. 122, no. 3, pp. 547–570, 1988.

[38] C. Bert and T. Chen, "On vibration of a thick flexible ring rotating at high speed," *Journal of Sound and Vibration*, vol. 61, no. 4, pp. 517–530, 1978.

[39] T. Irie, G. Yamada, and I. Takahashi, "The steady state out-of-plane response of a Timoshenko curved beam with internal damping," *J. Sound Vib.*, vol. 71, no. 1, pp. 145–156, 1980.

[40] T. Irie, G. Yamada, and H. Koizumi, "The steady state out-of-plane response of an internally damped ring supported by springs in some bays," *J. Sound Vib.*, vol. 81, no. 2, pp. 187–197, 1982.

[41] W. Bickford and S. Maganty, "On the out-of-plane vibrations of thick rings," *Journal of Sound and Vibration*, vol. 108, no. 3, pp. 503–507, 1986.

[42] R. ELEY, C. FOX, and S. MCWILLIAM, "Anisotropy effects on the vibration of circular rings made from crystalline silicon," *Journal of Sound and Vibration*, vol. 228, no. 1, pp. 11–35, 1999.

[43] A. Doria, M. Tognazzo, G. Cusimano, V. Bulsink, A. Cooke, and B. Koopman, "Identification of the mechanical properties of bicycle tyres for modelling of bicycle dynamics," *Vehicle System Dynamics*, vol. 51, no. 3, pp. 405–420, 2013.

[44] S. Gong, *Study of in-plane dynamics of tires*. PhD thesis, Delft University of Technology, 1993. ISBN 90-370-0092-4.

[45] D. Allaei, W. Soedel, and T. Yang, "Vibration analysis of non-axisymmetric tires," *Journal of Sound and Vibration*, vol. 122, no. 1, pp. 11–29, 1988.

[46] D. S. Stutts, W. Soedel, and S. K. Jha, "Fore-aft forces in tire-wheel assemblies generated by unbalances and the influence of balancing," *Tire Science and Technology*, vol. 19, pp. 142–162, jul 1991.

[47] D. Stutts, C. Krousgrill, and W. Soedel, "Parametric excitation of tire-wheel assemblies by a stiffness non-uniformity," *Journal of Sound and Vibration*, vol. 179, no. 3, pp. 499–512, 1995.

[48] Y. T. Wei, L. Nasdala, and H. Rothert, "Analysis of Tire Rolling Contact Response by REF Model," *Tire Science and Technology*, vol. 32, pp. 214–235, 10 2004.

[49] A. A. Popov and Z. Geng, "Modelling of vibration damping in pneumatic tyres," *Vehicle System Dynamics*, vol. 43, no. sup1, pp. 145–155, 2005.

[50] I. F. Kozhevnikov, "Vibrations of a rolling tyre," *Journal of Sound and Vibration*, vol. 331, no. 7, pp. 1669–1685, 2012.

[51] W. Graham, "Modelling the vibration of tyre sidewalls," *Journal of Sound and Vibration*, vol. 332, no. 21, pp. 5345–5374, 2013.

[52] J. Lee, S. Wang, B. Pluymers, W. Desmet, and P. Kindt, "A modified complex modal testing technique for a rotating tire with a flexible ring model," *Mechanical Systems and Signal Processing*, vol. 60-61, pp. 604–618, 2015.

[53] T. D. Vu, D. Duhamel, Z. Abbadi, H.-P. Yin, and A. Gaudin, "A nonlinear circular ring model with rotating effects for tire vibrations," *Journal of Sound and Vibration*, vol. 388, pp. 245–271, 2017.

[54] J. Yang, G. Jacobs, A. Kramer, P. Drichel, and C. Liu, "Investigation of the tire in-plane vibration property using an improved ring model," *Journal of Sound and Vibration*, vol. 478, p. 115350, 2020.

[55] Z. Liu and Q. Gao, "Development of a flexible belt on an elastic multi-stiffness foundation tire model for a heavy load radial tire with a large section ratio," *Mechanical Systems and Signal Processing*, vol. 123, pp. 43–67, 2019.

[56] Z. Liu, Y. Liu, and Q. Gao, "In-plane flexible ring modeling and a nonlinear stiffness solution for heavy-load radial tires," *Mechanical Systems and Signal Processing*, vol. 171, p. 108956, 2022.

[57] D. Garcia-Pozuelo, O. A. Olatunbosun, L. Romano, S. Strano, M. Terzo, A. J. Tuononen, and Y. Xiong, "Development and experimental validation of a real-time analytical model for different intelligent tyre concepts," *Vehicle System Dynamics*, vol. 57, no. 12, pp. 1970–1988, 2019.

[58] D. Jeong, S. B. Choi, J. Lee, M. Kim, and H. Lee, "Tire dimensionless numbers for analysis of tire characteristics and intelligent tire signals," *Mechanical Systems and Signal Processing*, vol. 161, p. 107927, 2021.

[59] H. Lee and S. Taheri, "A novel approach to tire parameter identification," *Proceedings of the Institution of Mechanical Engineers, Part D: Journal of Automobile Engineering*, vol. 233, no. 1, pp. 55–72, 2019.

[60] Y. Wang, Z. Liu, M. Kaliske, and Y. Wei, "Tire Rolling Kinematics Model for an Intelligent Tire Based on an Accelerometer," *Tire Science and Technology*, vol. 48, pp. 287–314, 01 2020.

[61] G. D. Shteinhauz, "Tire uniformity prediction using balance and low speed uniformity data," August 19 2003. US Patent 6,609,074.

[62] R. E. Symens and B. R. Stanoszek, "System and method for characterizing tire uniformity machines," June 13 2017. US Patent 9,677,972.

[63] S. L. Williams, S. M. Immel, G. S. Vicini, and G. J. Lipczynski, "Tire uniformity prediction using curve fitting," September 2 2003. US Patent 6,615,144.

[64] J. Walker and N. Reeves, "Uniformity of tires at vehicle operating speeds," *Tire Science and Technology*, vol. 2, no. 3, pp. 163–178, 1974.

[65] D. Schuring, "A statistical model of tire uniformity distributions," *Tire Science and Technology*, vol. 17, no. 1, pp. 2–14, 1989.

[66] T. L. Richards, "The relationship between angular velocity variations and fore and aft non-uniformity forces in tires," *SAE Transactions*, vol. 99, pp. 1086–1093, 1990.

[67] S. K. Song, C. H. Pak, S. C. Hong, J. W. Oh, J. H. Kim, and C. S. Kim, "Vibration analysis of the steering wheel of a passenger car due to the tire nonuniformity," in *SAE Technical Paper Series*, p. 15, SAE International, nov 1993.

[68] R. W. Scavuzzo, T. R. Richards, and L. Charek, "Tire vibration modes and effects on vehicle ride quality," *Tire Science and Technology*, vol. 21, no. 1, pp. 23–39, 1993.

[69] Y. Meijuan, D. Yuankan, R. Gall, and N. Rodriguez, "Effects of variations in geometry and material on the non-uniformity of tires," *Tire science and technology*, vol. 29, no. 1, pp. 56–64, 2001.

[70] K.-W. Kim, J.-B. Park, and S.-J. Lee, "Tire mass imbalance, rolling phase difference, non-uniformity induced force difference, and inflation pressure change effects on steering wheel vibration," in *SAE 2005 Noise and Vibration Conference and Exhibition*, pp. No. 2005–01–2317, SAE International, may 2005.

[71] H. R. Dorfi, "Tire non-uniformities and steering wheel vibrations," *Tire Science and Technology*, vol. 33, pp. 64–102, apr 2005.

[72] H. R. Dorfi, "Tyre non-uniformities: comparison of analytical and numerical tyre models and correlation to experimentally measured data," *Vehicle system dynamics*, vol. 43, no. sup1, pp. 223–240, 2005.

[73] T. D. Gillespie, "Influence of tire/wheel nonuniformities on heavy truck ride quality," techreport UM-HSRI-82-30, University of Michigan,Highway Safety Research Institute, Huron Parkway & Baxter Road, Ann Arbor, Michigan 48109, Sept. 1982.

[74] B. L. Dillinger, N. Jalili, and I. Ul Haque, "Analytical modelling and experimental verification of tyre non-uniformity," *International Journal of Vehicle Design*, vol. 46, no. 1, pp. 1–22, 2008.

[75] S. Dzierżek, "Experiment-based modeling of cylindrical rubber bushings for the simulation of wheel suspension dynamic behavior," *SAE Transactions*, vol. 109, pp. 78–85, 2000.

[76] M. G. Pottinger, "Uniformity: A crucial attribute of tire/wheel assemblies," *Tire Science and Technology*, vol. 38, no. 1, pp. 24–46, 2010.

[77] J. H. Kim, C. S. Kim, S. K. Song, C. H. Pak, S. C. Hong, and J. W. Oh, "Vibration analysis of the steering wheel of a passenger car due to the tire nonuniformity," in *International Pacific Conference On Automotive Engineering*, p. No. 931918, SAE International, nov 1993.

[78] J. C. Helton, "Uncertainty and sensitivity analysis techniques for use in performance assessment for radioactive waste disposal," *Reliability Engineering & System Safety*, vol. 42, pp. 327–367, jan 1993.

[79] M. Hanss, "The transformation method for the simulation and analysis of systems with uncertain parameters," *Fuzzy Sets and Systems*, vol. 130, pp. 277–289, sep 2002.

[80] M. Shinozuka and C.-M. Jan, "Digital simulation of random processes and its applications," *Journal of Sound and Vibration*, vol. 25, no. 1, pp. 111–128, 1972.

[81] M. Shinozuka, "Monte Carlo solution of structural dynamics," *Computers & Structures*, vol. 2, no. 5, pp. 855–874, 1972.

[82] M. Shinozuka and Y.-K. Wen, "Monte Carlo solution of nonlinear vibrations," *AIAA Journal*, vol. 10, no. 1, pp. 37–40, 1972.

[83] M. Kamiński and M. Kleiber, "Perturbation based stochastic finite element method for homogenization of two-phase elastic composites," *Computers & Structures*, vol. 78, no. 6, pp. 811–826, 2000.

[84] M. Kamiński, "Generalized perturbation-based stochastic finite element method in elastostatics," *Computers & Structures*, vol. 85, no. 10, pp. 586–594, 2007. Stochastic Structural Analysis, Optimization and Re-Analysis.

[85] R. G. Ghanem and P. D. Spanos, *Stochastic Finite Elements: A Spectral Approach*. Springer New York, 1 ed., 1991.

[86] R. Y. Rubinstein and D. P. Kroese, *Simulation and the Monte Carlo Method*. John Wiley & Sons, Inc., nov 2016.

[87] M. H. Kalos and P. A. Whitlock, *Monte Carlo Methods*. Wiley, sep 2008.

[88] D. Novák and D. Lehký, "ANN inverse analysis based on stochastic small-sample training set simulation," *Engineering Applications of Artificial Intelligence*, vol. 19, pp. 731–740, oct 2006.

[89] S.-K. Choi, R. V. Grandhi, R. A. Canfield, and C. L. Pettit, "Polynomial chaos expansion with Latin hypercube sampling for estimating response variability," *AIAA Journal*, vol. 42, pp. 1191–1198, jun 2004.

[90] S.-K. Choi, R. A. Canfield, and R. V. Grandhi, "Estimation of structural reliability for Gaussian random fields," *Structure and Infrastructure Engineering*, vol. 2, pp. 161–173, sep 2006.

[91] R.-B. Chen, D.-N. Hsieh, Y. Hung, and W. Wang, "Optimizing Latin hypercube designs by particle swarm," *Statistics and Computing*, vol. 23, pp. 663–676, oct 2012.

[92] N. Wiener, "The homogeneous chaos," *American Journal of Mathematics*, vol. 60, no. 4, pp. 897–936, 1938.

[93] D. Xiu and G. E. Karniadakis, "The Wiener–Askey polynomial chaos for stochastic differential equations," *SIAM Journal on Scientific Computing*, vol. 24, pp. 619–644, jan 2002.

[94] S. S. Isukapalli, *Uncertainty analysis of transport-transformation models*. phdthesis, The State University of New Jersey, New Brunswick, New Jersey, USA, Jan. 1999.

[95] G. Kewlani and K. Iagnemma, "A stochastic response surface approach to statistical prediction of mobile robot mobility," in *2008 IEEE/RSJ International Conference on Intelligent Robots and Systems*, pp. 2234–2239, IEEE, sep 2008.

[96] D. Xiu, *Numerical methods for stochastic computations: a spectral method approach*. Princeton university press, 2010.

[97] K. Sepahvand and S. Marburg, "Non-sampling inverse stochastic numerical–experimental identification of random elastic material parameters in composite plates," *Mechanical Systems and Signal Processing*, vol. 54-55, pp. 172–181, 2015.

[98] H.-P. Wan, W.-X. Ren, and M. D. Todd, "Arbitrary polynomial chaos expansion method for uncertainty quantification and global sensitivity analysis in structural dynamics," *Mechanical Systems and Signal Processing*, vol. 142, p. 106732, 2020.

[99] J. Cui, Z.-H. Zhao, J.-W. Liu, P.-X. Hu, R.-N. Zhou, and G.-X. Ren, "Uncertainty analysis of mechanical dynamics by combining response surface method with signal decomposition technique," *Mechanical Systems and Signal Processing*, vol. 158, p. 107570, 2021.

[100] J.-J. Sinou and E. Jacquelin, "Influence of polynomial chaos expansion order on an uncertain asymmetric rotor system response," *Mechanical Systems and Signal Processing*, vol. 50-51, pp. 718–731, 2015.

[101] J. Wu, Z. Luo, N. Zhang, Y. Zhang, and P. D. Walker, "Uncertain dynamic analysis for rigid-flexible mechanisms with random geometry and material properties," *Mechanical Systems and Signal Processing*, vol. 85, pp. 487–511, 2017.

[102] L. Li and C. Sandu, "On the impact of cargo weight, vehicle parameters, and terrain characteristics on the prediction of traction for off-road vehicles," *Journal of Terramechanics*, vol. 44, pp. 221–238, jul 2007.

[103] A. Sandu, C. Sandu, and M. Ahmadian, "Modeling multibody systems with uncertainties. Part I: theoretical and computational aspects," *Multibody System Dynamics*, vol. 15, pp. 369–391, may 2006.

[104] C. Sandu, A. Sandu, and M. Ahmadian, "Modeling multibody systems with uncertainties. Part II: numerical applications," *Multibody System Dynamics*, vol. 15, pp. 241–262, apr 2006.

[105] G. Kewlani, J. Crawford, and K. Iagnemma, "A polynomial chaos approach to the analysis of vehicle dynamics under uncertainty," *Vehicle System Dynamics*, vol. 50, pp. 749–774, may 2012.

[106] J. Wu, Z. Luo, N. Zhang, and Y. Zhang, "A new uncertain analysis method and its application in vehicle dynamics," *Mechanical Systems and Signal Processing*, vol. 50-51, pp. 659–675, 2015.

[107] K. Kwon, N. Ryu, M. Seo, S. Kim, T. H. Lee, and S. Min, "Efficient uncertainty quantification for integrated performance of complex vehicle system," *Mechanical Systems and Signal Processing*, vol. 139, p. 106601, 2020.

[108] K. Sepahvand, "Spectral stochastic finite element vibration analysis of fiber-reinforced composites with random fiber orientation," *Composite Structures*, vol. 145, pp. 119–128, 2016.

[109] K. Sepahvand, "Stochastic finite element method for random harmonic analysis of composite plates with uncertain modal damping parameters," *Journal of Sound and Vibration*, vol. 400, pp. 1–12, 2017.

[110] P. Ni, Y. Xia, J. Li, and H. Hao, "Using polynomial chaos expansion for uncertainty and sensitivity analysis of bridge structures," *Mechanical Systems and Signal Processing*, vol. 119, pp. 293–311, 2019.

[111] J. Yuan, A. Fantetti, E. Denimal, S. Bhatnagar, L. Pesaresi, C. Schwingshackl, and L. Salles, "Propagation of friction parameter uncertainties in the nonlinear dynamic response of turbine blades with underplatform dampers," *Mechanical Systems and Signal Processing*, vol. 156, p. 107673, 2021.

[112] S. Wang, L. Hua, X. Han, and Z. Su, "Reliability-based design optimization for vertical vibrations of a modified electric vehicle using fourth-moment polynomial standard transformation method," *Proceedings of the Institution of Mechanical Engineers, Part D: Journal of Automobile Engineering*, vol. 234, no. 10-11, pp. 2649–2664, 2020.

[113] Z. Ma, J. Yang, M. Jiang, and Y. Zhang, "Recursive estimation of vehicle inertial parameters using polynomial chaos theory via vehicle handling model," in *SAE Technical Paper Series*, SAE International, apr 2015.

[114] S. K. I. Shimp, "Vehicle sprung mass parameter estimation using an adaptive polynomial-chaos method," Master's thesis, Virginia Polytechnic Institute and State University, Apr. 2008.

[115] D. B. Price, "Estimation of uncertain vehicle center of gravity using polynomial chaos expansions," Master's thesis, Virginia Polytechnic Institute and State University, 2008.

[116] K. Sepahvand, M. Scheffler, and S. Marburg, "Uncertainty quantification in natural frequencies and radiated acoustic power of composite plates: Analytical and experimental investigation," *Applied Acoustics*, vol. 87, pp. 23–29, 2015.

[117] S. Yin, D. Yu, Z. Ma, and B. Xia, "A unified model approach for probability response analysis of structure-acoustic system with random and epistemic uncertainties," *Mechanical Systems and Signal Processing*, vol. 111, pp. 509–528, 2018.

[118] T. Kuhn, J. Dürrwächter, F. Meyer, A. Beck, C. Rohde, and C.-D. Munz, "Uncertainty quantification for direct aeroacoustic simulations of cavity flows," *Journal of Theoretical and Computational Acoustics*, vol. 27, no. 01, p. 1850044, 2019.

[119] D. Fritze, S. Marburg, and H.-J. Hardtke, "Estimation of radiated sound power: A case study on common approximation methods," *Acta Acustica united with Acustica*, vol. 95, pp. 833–842, sep 2009.

[120] S.-J. Kim and A. R. Savkoor, "The contact problem of in-plane rolling of tires on a flat road," *Vehicle System Dynamics*, vol. 27, no. S1, pp. 189–206, 1997.

[121] S. T. Jansen, L. Verhoeff, R. Cremers, A. J. Schmeitz, and I. J. Besselink, "MF-Swift simulation study using benchmark data," *Vehicle System Dynamics*, vol. 43, no. sup1, pp. 92–101, 2005.

[122] J. De Cuyper, M. Furmann, D. Kading, and M. Gubitosa, "Vehicle dynamics with LMS Virtual.Lab Motion," *Vehicle System Dynamics*, vol. 45, no. S1, pp. 199–206, 2007.

[123] Z. Liu, W. Zhao, K. K. Sepahvand, Y. Wei, and S. Marburg, "A three-dimensional ring model for uncertainty quantification in natural frequencies and sound radiation characteristics of

tires," *Journal of Theoretical and Computational Acoustics*, vol. 28, no. 02, p. 2050016, 2020.

[124] P. Zegelaar, S. Gong, and H. Pacejka, "Tyre models for the study of in-plane dynamics," *Vehicle System Dynamics*, vol. 23, pp. 578–590, jan 1994.

[125] P. Zegelaar and H. Pacejka, "The in-plane dynamics of tyres on uneven roads," *Vehicle System Dynamics*, vol. 25, pp. 714–730, jan 1996.

[126] S. Kim, P. E. Nikravesh, and G. Gim, "A two-dimensional tire model on uneven roads for vehicle dynamic simulation," *Vehicle System Dynamics*, vol. 46, no. 10, pp. 913–930, 2008.

[127] H. R. Dorfi, R. L. Wheeler, and B. B. Keum, "Vibration modes of radial tires: Application to non-rolling and rolling events," in *SAE Technical Paper Series*, p. 10, SAE International, may 2005.

[128] R. L. Haupt and S. E. Haupt, *Practical genetic algorithms*. John Wiley & Sons, Ltd, May 2003.

[129] H. Lee, M. T. Kim, and S. Taheri, "Estimation of tire–road contact features using strain-based intelligent tire," *Tire Science and Technology*, vol. 46, pp. 276–293, sep 2018.

[130] S. K. Clark, *Mechanics of pneumatic tires*. Washington, D.C.: National Bureau of Standards, 1971.

[131] M. Gipser, "FTire, a new fast tire model for ride comfort simulations," in *International ADAMS User's Conference*, (Berlin, Germany), pp. 1–11, 1999.

[132] C. Wei, O. A. Olatunbosun, and X. Yang, "A finite-element-based approach to characterising FTire model for extended range of operation conditions," *Vehicle System Dynamics*, vol. 55, no. 3, pp. 295–312, 2017.

[133] T. H. Koornwinder, *Orthogonal Polynomials*, pp. 145–170. Vienna: Springer Vienna, 2013.

[134] T. S. Chihara, *An introduction to orthogonal polynomials*. Gordon and Breach, Science Publishers, Inc., 1978.

[135] W. Gautschi, *Orthogonal Polynomials: Computation and Approximation*. Oxford University Press, 04 2004.

[136] G. FREUD, *Orthogonal Polynomials*. Elsevier, 1971.

[137] D. Xiu, *Numerical Methods for Stochastic Computations*. Princeton: Princeton University Press, 2010.

[138] N. Wiener, "The homogeneous chaos," *American Journal of Mathematics*, vol. 60, no. 4, pp. 897–936, 1938.

[139] D. Xiu, *Generalized (Wiener-Askey) Polynomial Chaos*. PhD thesis, Brown University, May 2004.

[140] R. G. Ghanem and P. D. Spanos, *Stochastic Finite Elements: A Spectral Approach*, ch. Stochastic Finite Element Method: Response Statistics, pp. 101–119. New York, NY: Springer New York, 1991.

[141] R. Ghanem, "Stochastic finite elements with multiple random non-gaussian properties," *Journal of Engineering Mechanics*, vol. 125, no. 1, pp. 26–40, 1999.

[142] E. S. Pearson, "Some problems arising in approximating to probability distributions, using moments," *Biometrika*, vol. 50, p. 95, jun 1963.

[143] N. L. Johnson, E. Nixon, D. E. Amos, and E. S. Pearson, "Table of percentage points of Pearson curves, for given $\sqrt{\beta_1}$ and β_2, expressed in standard measure," *Biometrika*, vol. 50, no. 3/4, pp. 459–498, 1963.

[144] D. Xiu, "Efficient collocational approach for parametric uncertainty analysis," *Communications in Computational Physics*, vol. 2, no. 2, pp. 293–309, 2007.

[145] D. Gottlieb and D. Xiu, "Galerkin method for wave equations with uncertain coefficients," *Communications in Computational Physics*, vol. 3, no. 2, pp. 505–518, 2008.

[146] M. D. Mckay, R. J. Beckman, and W. J. Conover, "A comparison of three methods for selecting values of input variables in the analysis of output from a computer code," *Technometrics*, vol. 42, pp. 55–61, feb 2000.

[147] W. Li, Z. Lu, and D. Zhang, "Stochastic analysis of unsaturated flow with probabilistic collocation method," *Water Resources Research*, vol. 45, no. 8, 2009.

[148] D. Li, S. Jiang, Y. Cheng, and C. Zhou, "A comparative study of three collocation point methods for odd order stochastic response surface method," *Structural Engineering and Mechanics*, vol. 45, no. 5, pp. 595–611, 2013.

[149] M. Ahsanullah, *Characterizations of Univariate Continuous Distributions*. Atlantis Press, 1 ed., 2017.

[150] N. Balaramakrishna and R. K. Kumar, "A study on the effect of different tyre imperfections on steering wheel vibration," *Vehicle system dynamics*, vol. 47, no. 6, pp. 753–770, 2009.

[151] K. Ye, J. Zhao, Y. Zhang, X. Liu, and H. Zhang, "A generalized computationally efficient copula-polynomial chaos framework for probabilistic power flow considering nonlinear correlations of PV injections," *International Journal of Electrical Power & Energy Systems*, vol. 136, p. 107727, 2022.

[152] F. Ni, P. H. Nguyen, and J. F. G. Cobben, "Basis-adaptive sparse polynomial chaos expansion for probabilistic power flow," *IEEE Transactions on Power Systems*, vol. 32, no. 1, pp. 694–704, 2017.

[153] M. Fan, Z. Li, T. Ding, L. Huang, F. Dong, Z. Ren, and C. Liu, "Uncertainty evaluation algorithm in power system dynamic analysis with correlated renewable energy sources," *IEEE Transactions on Power Systems*, vol. 36, no. 6, pp. 5602–5611, 2021.

[154] G. Wang, H. Xin, D. Wu, P. Ju, and X. Jiang, "Data-driven arbitrary polynomial chaos-based probabilistic load flow considering correlated uncertainties," *IEEE Transactions on Power Systems*, vol. 34, no. 4, pp. 3274–3276, 2019.

[155] D. Li, Y. Chen, W. Lu, and C. Zhou, "Stochastic response surface method for reliability analysis of rock slopes involving correlated non-normal variables," *Computers and Geotechnics*, vol. 38, no. 1, pp. 58–68, 2011.

[156] T. A. Mara and W. E. Becker, "Polynomial chaos expansion for sensitivity analysis of model output with dependent inputs," *Reliability Engineering & System Safety*, vol. 214, p. 107795, 2021.

[157] I. Caylak, E. Penner, A. Dridger, and R. Mahnken, "Stochastic hyperelastic modeling considering dependency of material parameters," *Computational Mechanics*, vol. 62, pp. 1273–1285, mar 2018.

[158] X. Wei, Z. Zhu, Q. Xu, Y. Gao, and Z. Yan, "Comparisons of correlated random variables decorrelation methods in probabilistic power flow calculation," in *2022 Power System and Green Energy Conference (PSGEC)*, pp. 868–873, 2022.

[159] J. D. Jakeman, F. Franzelin, A. Narayan, M. Eldred, and D. Plfüger, "Polynomial chaos expansions for dependent random variables," *Computer Methods in Applied Mechanics and Engineering*, vol. 351, pp. 643–666, 2019.

[160] Y. Zhang, J. Xu, and Y. Dong, "Reliability analysis with correlated random variables based on a novel transformation, adaptive dimension-reduction and maximum entropy method," *Computers & Structures*, vol. 274, p. 106919, 2023.

[161] W. He, P. Hao, and G. Li, "A novel approach for reliability analysis with correlated variables based on the concepts of entropy and polynomial chaos expansion," *Mechanical Systems and Signal Processing*, vol. 146, p. 106980, 2021.

[162] F. Zhao, Z. Tian, and Y. Zeng, "A stochastic collocation approach for efficient integrated gear health prognosis," *Mechanical Systems and Signal Processing*, vol. 39, no. 1, pp. 372–387, 2013.

[163] J. Qian and Y. Dong, "Uncertainty and multi-criteria global sensitivity analysis of structural systems using acceleration algorithm and sparse polynomial chaos expansion," *Mechanical Systems and Signal Processing*, vol. 163, p. 108120, 2022.

[164] H.-P. Wan, W.-X. Ren, and M. D. Todd, "Arbitrary polynomial chaos expansion method for uncertainty quantification and global sensitivity analysis in structural dynamics," *Mechanical Systems and Signal Processing*, vol. 142, p. 106732, 2020.

[165] M. Ghaith, Z. Li, and B. W. Baetz, "Uncertainty analysis for hydrological models with interdependent parameters: An improved polynomial chaos expansion approach," *Water Resources Research*, vol. 57, no. 8, p. e2020WR029149, 2021. e2020WR029149 2020WR029149.

[166] J. B. Nagel, J. Rieckermann, and B. Sudret, "Principal component analysis and sparse polynomial chaos expansions for global sensitivity analysis and model calibration: Application to urban drainage simulation," *Reliability Engineering & System Safety*, vol. 195, p. 106737, 2020.

[167] P. Manfredi and S. Grivet-Talocia, "Fast stochastic surrogate modeling via rational polynomial chaos expansions and principal component analysis," *IEEE Access*, vol. 9, pp. 102732–102745, 2021.

Appendix A

Coefficients of Steady-state Responses

Here the coefficients in the expressions of the steady-state response, Eqs. (2.44-2.45) and Eqs. (2.54-2.55), are listed as follows:

1. Coefficients corresponding to the in-plane displacements:

$$\mathbf{A}_{un} = \left\{ \begin{array}{c} A_{un1} \\ A_{un2} \\ A_{un3} \end{array} \right\} = \frac{1}{\pi\sqrt{B_1^2+B_2^2}} \left\{ \begin{array}{c} B_3 + \mathrm{i}B_4 \\ \mathrm{i}A_{12} \\ (-nB_4 + \mathrm{i}nB_3 + \mathrm{i}A_{12})/R \end{array} \right\}, \tag{A.145}$$

$$\mathbf{A}_{vn} = \left\{ \begin{array}{c} A_{vn1} \\ A_{vn2} \\ A_{vn3} \end{array} \right\} = \frac{1}{\pi\sqrt{B_1^2+B_2^2}} \left\{ \begin{array}{c} -\mathrm{i}A_{12} \\ B_5 + \mathrm{i}B_6 \\ (nA_{12} + B_5 + \mathrm{i}B_6)/R \end{array} \right\}, \tag{A.146}$$

in which the coefficients are

$$\begin{aligned} A_{11} &= -\left(n\Omega + \omega_f\right)^2 m_{11} + k_{11} + \mathrm{i}\left(n\Omega + \omega_f\right) c_u, \\ A_{12} &= -\left(n\Omega + \omega_f\right) g_{1n} + k_{12}, \\ A_{22} &= -\left(n\Omega + \omega_f\right)^2 m_{11} + k_{13} + \mathrm{i}\left(n\Omega + \omega_f\right) c_v, \end{aligned} \tag{A.147}$$

$$
\begin{aligned}
B_1 &= B_3B_5 - B_4B_6 - A_{12}^2, & B_2 &= B_4B_5 + B_3B_6,\\
B_3 &= -\left(n\Omega + \omega_f\right)^2 m_{11} + k_{13}, & B_4 &= \left(n\Omega + \omega_f\right) c_v,\\
B_5 &= -\left(n\Omega + \omega_f\right)^2 m_{11} + k_{11}, & B_6 &= \left(n\Omega + \omega_f\right) c_u,
\end{aligned} \tag{A.148}
$$

$$
n\gamma_{n1} = \arctan\left(\frac{B_2}{B_1}\right). \tag{A.149}
$$

2. Coefficients corresponding to the out-of-plane displacements:

$$
\mathbf{A}_{wn} = \left\{ \begin{array}{c} A_{wn1} \\ A_{wn2} \\ A_{wn3} \end{array} \right\} = \frac{1}{\pi\sqrt{D_1^2 + D_2^2}} \left\{ \begin{array}{c} D_3 + \mathrm{i}D_4 \\ -C_{12} \\ (-nD_4 + \mathrm{i}nD_3)/R \end{array} \right\}, \tag{A.150}
$$

$$
\mathbf{A}_{\phi n} = \left\{ \begin{array}{c} A_{\phi n1} \\ A_{\phi n2} \\ A_{\phi n3} \end{array} \right\} = \frac{1}{\pi\sqrt{D_1^2 + D_2^2}} \left\{ \begin{array}{c} -C_{12} \\ D_5 + \mathrm{i}D_6 \\ -\mathrm{i}nC_{12}/R \end{array} \right\}, \tag{A.151}
$$

in which the coefficients are

$$
\begin{aligned}
C_{11} &= -\left(n\Omega + \omega_f\right)^2 m_{21} + k_{21} + \mathrm{i}c_w\left(n\Omega + \omega_f\right),\\
C_{12} &= -\left(n\Omega + \omega_f\right)^2 m_{22} - g_{2n}\left(n\Omega + \omega_f\right) + k_{22},\\
C_{22} &= -\left(n\Omega + \omega_f\right)^2 m_{23} + k_{23} + \mathrm{i}c_u\frac{b_{op}^2}{4}\left(n\Omega + \omega_f\right),
\end{aligned} \tag{A.152}
$$

$$
\begin{aligned}
D_1 &= D_3D_5 - D_4D_6 - C_{12}^2, & D_2 &= D_4D_5 + D_3D_6,\\
D_3 &= -\left(n\Omega + \omega_f\right)^2 m_{23} + k_{23}, & D_4 &= \left(n\Omega + \omega_f\right) c_u\frac{b_{op}^2}{4},\\
D_5 &= -\left(n\Omega + \omega_f\right)^2 m_{21} + k_{21}, & D_6 &= \left(n\Omega + \omega_f\right) c_w,
\end{aligned} \tag{A.153}
$$

$$
n\gamma_{n2} = \arctan\left(\frac{D_2}{D_1}\right). \tag{A.154}
$$

Appendix B

Coefficients in Contact Algorithm

B.1 Steady-state displacements of flexible ring

Here, the coefficients in the expressions of the steady-state response, Eqs. (3.84-3.85) and Eq. (3.87), are listed as follows:

(i) Matrix of the displacements of the flexible ring **U**

The deformation of the flexible ring is not limited to the contact patch. As each node on the flexible ring has 3 DOFs, the displacements of N_r nodes in the contact area can compose a $(3N_r \times 1)$-dimensional vector.

$$\mathbf{U} = \left\{ \begin{array}{ccccccc} u_1 & v_1 & \beta_1 & \ldots. & u_{N_r} & v_{N_r} & \beta_{N_r} \end{array} \right\}^{\mathrm{T}}. \tag{B.155}$$

If only the displacements of the N_c contacted nodes need to be evaluated, the vector **U** is reconstructed by the corresponding N_c elements. Accordingly, the dimension of the displacement vector becomes $(3N_c \times 1)$.

(ii) Matrix of the generalized forces **Q**

Similarly, the vector of generalized forces generated in contact area **q** is also a $(3N_c \times 1)$-dimensional vector,

$$\mathbf{q} = \left\{ \begin{array}{ccccccc} q_{u,1} & q_{v,1} & q_{\beta,1} & \ldots. & q_{u,N_c} & q_{v,N_c} & q_{\beta,N_c} \end{array} \right\}^{\mathrm{T}}. \tag{B.156}$$

The amplitude of the generalized force under a set of concentrated forces, $\mathbf{Q}$, is expressed as

$$\mathbf{Q} = \left\{ \begin{array}{cccccc} Q_{u,1} & Q_{v,1} & Q_{\beta,1} & \cdots & Q_{u,N_c} & Q_{v,N_c} & Q_{\beta,N_c} \end{array} \right\}^{\mathrm{T}}. \tag{B.157}$$

(iii) Compliance matrix $\mathbf{T}$

Based on the expressions of the steady-state responses, Eq. (3.84-3.85), the tangential displacement in matrix form is given by

$$v(\phi) = \left\{ \left\{ A_{1v1} A_{2v1} A_{3v1} \right\}, \left\{ A_{1v2} A_{2v2} A_{3v2} \right\}, \ldots, \left\{ A_{1vN_c} A_{2vN_c} A_{3vN_c} \right\} \right\} \mathbf{Q}, \tag{B.158}$$

in which,

$$\begin{aligned} A_{1vk} &= \sum_{n=1}^{N} A_{n2} \sin \alpha_k, \quad A_{2vk} = \sum_{n=1}^{N} A_{n1} \cos \alpha_k, \quad A_{3vk} = \sum_{n=1}^{N} \left(1 - n^2\right) A_{n1} \cos \alpha_k, \\ \alpha_k &= n \left(\phi_{ck} - \phi + \gamma_n\right), \ k = 1, \ldots, N_c. \end{aligned} \tag{B.159}$$

In the Chapter 2, the truncated number of modes N selected is 30. Accordingly, the radial displacement and the rotation angle of the cross-section of the ring are written in a similar form. The following equation represents the steady-state response at the ϕ point under the action of a set of N_c concentrated forces.

$$\begin{aligned} \left\{ \begin{array}{c} u(\phi) \\ v(\phi) \\ \beta(\phi) \end{array} \right\} &= \left[\begin{array}{ccc} A_{1u1} A_{2u1} A_{3u1} & A_{1u2} A_{2u2} A_{3u2}, \ldots, A_{1uN_c} A_{2uN_c} A_{3uN_c} \\ A_{1v1} A_{2v1} A_{3v1} & A_{1v2} A_{2v2} A_{3v2}, \ldots, A_{1vN_c} A_{2vN_c} A_{3vN_c} \\ A_{1\beta1} A_{2\beta1} A_{3\beta1} & A_{1\beta2} A_{2\beta2} A_{3\beta2}, \ldots, A_{1\beta N_c} A_{2\beta N_c} A_{3\beta N_c} \end{array} \right] \mathbf{Q} \\ &= \mathbf{A_j Q}, \quad j = 1, \ldots, N_r. \end{aligned} \tag{B.160}$$

The coefficients in $\mathbf{A_j}$ are listed as follows:

$$\begin{aligned} A_{1uk} &= \sum_{n=1}^{N} n A_{n2} \cos \alpha_k, \quad A_{2uk} = \sum_{n=1}^{N} -n A_{n1} \sin \alpha_k, \quad A_{3uk} = \sum_{n=1}^{N} -n \left(1 - n^2\right) A_{n1} \sin \alpha_k, \\ A_{1\beta k} &= \sum_{n=1}^{N} \left(1 - n^2\right) A_{n2} \sin \alpha_k / R, \quad A_{2\beta k} = \sum_{n=1}^{N} \left(1 - n^2\right) A_{n1} \cos \alpha_k / R, \end{aligned}$$

$$A_{3\beta k} = \sum_{n=1}^{N} \left(1-n^2\right)^2 A_{n1} \cos\alpha_k / R, \quad \alpha_k = n\left(\phi_{ck} - \phi + \gamma_n\right), \ k = 1,\ldots,N_c. \tag{B.161}$$

So far, the compliance matrix $\mathbf{T}$ is written as

$$\mathbf{T} = \left[\begin{array}{ccccccc} \mathbf{A_1} & \mathbf{A_2} & \cdots & \mathbf{A_j} & \cdots & \mathbf{A_{Nr}} \end{array}\right]^{\mathrm{T}}_{3N_r \times 3N_c}. \tag{B.162}$$

B.2 Linearized boundary equations for the treadband

B.2.1 Generalized force matrix of the tread rubber F

$\mathbf{F}$ denotes the generalized force matrix associated with the deformation of the tread rubber, the parameters of which are independent of the displacement vector $\mathbf{U}$. The dimension of $\mathbf{F}$ is $(1\times 3N_c)$, and its expression is given as

$$\mathbf{F} = \{\mathbf{F_1},\ \mathbf{F_2},\ ...,\ \mathbf{F_i},\ ...,\ \mathbf{F_{N_c}}\}^{\mathrm{T}}, \tag{B.163}$$

where

$$\mathbf{F_i} = \left\{F_{i,1} \quad F_{i,2} \quad F_{i,3}\right\}^{\mathrm{T}}, \quad i = 1,\ldots,N_c. \tag{B.164}$$

The coefficients of $\mathbf{F_i}$ are listed as

$$\begin{aligned} F_{i,1} = {} & [\left(R_l - z_w - h_0 + R_e\phi_i^2\right)\cos\phi_i + \left(R_l - z_w - h_0\right)\phi_i \sin\phi_i - R\phi_i \sin 2\phi_i - R\cos^2\phi_i]k_{Es} \\ & - [\left(R_l - z_w - R_e\right)\phi_i \sin\phi_i - R\phi_i \sin 2\phi_i + R_e\phi_i^2 \cos\phi_i + R\sin^2\phi_i]k_{Gs}, \end{aligned} \tag{B.165}$$

$$\begin{aligned} F_{i,2} = {} & [\left(-R_l + z_w + h_0 - R_e\phi_i^2\right)\sin\phi_i + \left(R_l - z_w - h_0\right)\phi_i \cos\phi_i + R\phi_i \sin^2\phi_i \\ & - R\phi_i \cos^2\phi_i + R/2\sin 2\phi_i]k_{Es} - [\left(-R_l + z_w + R_e\right)\phi_i \cos\phi_i - R/2\sin 2\phi_i \\ & + R\phi_i \cos^2\phi_i + R_e\phi_i^2 \sin\phi_i - R\phi_i \sin^2\phi_i]k_{Gs}, \end{aligned} \tag{B.166}$$

$$F_{i,3} = [-\left(R_l - z_w\right)\phi_i + R_e\phi_i - R\sin\phi_i + R\phi_i\cos\phi_i]\, h_0 k_{Gs}. \tag{B.167}$$

B.2.2 Coupling terms H

$\mathbf{H}$ is the coefficient matrix associated with the displacements of the ring, which contains the coupling terms of the stiffness coefficients of the tread rubber and the displacements of the ring.

The dimension of $\mathbf{H}$ is $(3N_c \times 3N_c)$. The matrix is expressed as

$$\mathbf{H} = \begin{bmatrix} \mathbf{H_1} & & & \\ & \mathbf{H_2} & & \\ & & \ddots & \\ & & & \mathbf{H_{N_c}} \end{bmatrix}, \tag{B.168}$$

where

$$\mathbf{H_i} = \begin{bmatrix} H_{i,11} & H_{i,12} & H_{i,13} \\ H_{i,21} & H_{i,22} & H_{i,23} \\ H_{i,31} & H_{i,32} & H_{i,33} \end{bmatrix}. \tag{B.169}$$

The coefficients of $\mathbf{H_i}$ are given as

$$\begin{aligned}
H_{i,11} &= -\cos^2\phi_i k_{Es} - \sin^2\phi_i k_{Gs}, \\
H_{i,12} &= -\frac{(k_{Es}+k_{Gs})}{2}\sin 2\phi_i, \\
H_{i,13} &= [(R_l - z_w - h_0)\sin\phi_i + R_e\phi_i\cos\phi_i - R\sin 2\phi_i + R\phi_i\sin^2\phi_i]k_{Es} \\
&\quad - (R_e\sin\phi_i - R\sin 2\phi_i + R_e\phi_i\cos\phi_i)\,k_{Gs}, \\
H_{i,21} &= H_{i,12}, \\
H_{i,22} &= -\sin^2\phi_i k_{Es} - \cos^2\phi_i k_{Gs}, \\
H_{i,23} &= \left[(R_l - z_w - h_0)\cos\phi_i - R_e\phi_i\sin\phi_i + R\sin^2\phi_i - R\cos^2\phi_i\right]k_{Es} \\
&\quad + \left(R_e\cos\phi_i + R\cos^2\phi_i + R_e\phi_i\sin\phi_i - R\sin^2\phi_i\right)k_{Gs}, \\
H_{i,31} &= -h_0\sin\phi_i k_{Gs}, \\
H_{i,32} &= -h_0\cos\phi_i k_{Gs}, \\
H_{i,33} &= (R_l - z_w + R\cos\phi_i)\,h_0 k_{Gs}, \\
i &= 1,\ldots,N_c
\end{aligned} \tag{B.170}$$

Appendix C

Some Notes on Stochastic Analysis

C.1 Jacobi polynomial and beta distribution

In the gPC expansion, the optimal orthogonal polynomial corresponding to the beta distribution is the Jacobi polynomial. Let Z be a random variable of beta distribution in $(-1,1)$ with PDF

$$\rho(x) = \frac{\Gamma(\alpha+\beta+2)}{2^{\alpha+\beta+1}\Gamma(\alpha+1)\Gamma(\beta+1)}(1-x)^{\alpha}(1+x)^{\beta}, \quad \alpha,\beta > -1. \tag{C.171}$$

The Jacobi orthogonal polynomials with the parameters α and β are defined as

$$J_n^{(\alpha,\beta)}(x) = \frac{(\alpha+1)_n}{n!}{}_2F_1\left(-n, n+\alpha+\beta+1; \alpha+1; \frac{1-x}{2}\right), \tag{C.172}$$

in which

$${}_rF_s(-n,\cdots,a_r;b_1,\cdots b_s;z) = \sum_{k=0}^{n}\frac{(-n)_k\cdots(a_r)_k}{(b_1)_k\cdots(b_s)_k}\frac{z^k}{k!}. \tag{C.173}$$

The expressions for the first few terms are given as

$$J_0^{(\alpha,\beta)}(x) = 1, \quad J_1^{(\alpha,\beta)}(x) = \frac{1}{2}\left[\alpha-\beta+(\alpha+\beta+2)x\right], \cdots. \tag{C.174}$$

The Legendre polynomial chaos becomes a special case of the Jacobi polynomial chaos with $\alpha = \beta = 0$. The orthogonality is shown as

$$\int_{-1}^{1} J_m^{(\alpha,\beta)}(x) J_n^{(\alpha,\beta)}(x) w(x)\, dx = h_n^2 \delta_{mn}, \quad \alpha,\beta > -1, \tag{C.175}$$

where

$$h_n^2 = \frac{(\alpha+1)_n(\beta+1)_n}{n!\,(2n+\alpha+\beta+1)\,(\alpha+\beta+2)_{n-1}}, \tag{C.176}$$

in which $\delta_{mn} = 0$ if $m \neq n$ and $\delta_{mn} = 1$ if $m = n$, is the Kronecker delta function.

C.2 Pearson family

The Pearson system can be used to construct the PDF of a random variable based on its first four central moments (mean, standard deviation, skewness, and kurtosis). Basically, the differential equation is solved based on the different criteria of the three coefficients b_0, b_1, and b_2 in Eq. (7.142-7.143). The limit for all distributions is line $\beta_2 - \beta_1^2 - 1 = 0$. In Fig. C.1, the Latin numerals refer to the traditional classification of Pearson distributions.

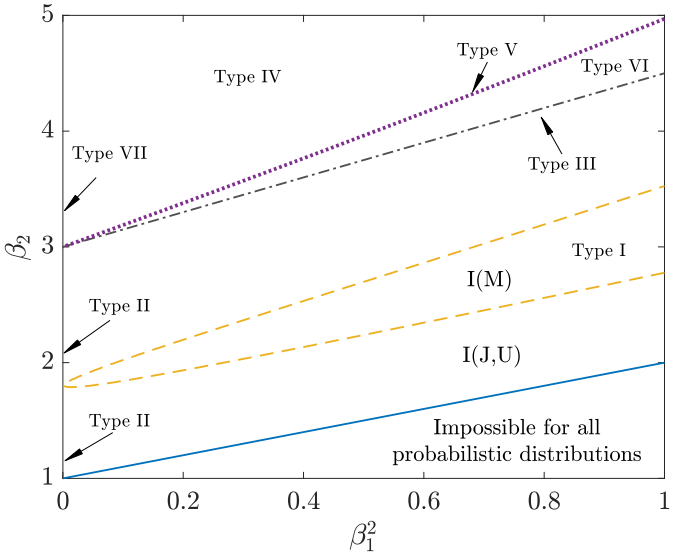

Figure C.1: Diagram showing the areas and bounding curves associated with the different solutions of Pearson's differential equation.

- Types I and II are the four-parameter beta distributions. Notation I(J,U) refers to J- and U- shaped distributions, and I(M) to uni-modal. The boundary of I(J,U) is defined by $4\left(4\beta_2 - 3\beta_1^2\right)\left(5\beta_2 - 6\beta_1^2 - 9\right)^2 = \beta_1^2(\beta_2+3)^2\left(8\beta_2 - 9\beta_1^2 - 12\right)$;

- Type III (gamma distributions) limit is $\beta_2 - {}^3\!/_2\beta_1^2 - 3 = 0$;
- Type IV is obtained when $b_0 + b_1 + b_2x^2 = 0$ has complex roots;
- Type V is defined by $\beta_1^2(\beta_2+3)^2 = 4\left(4\beta_2 - 3\beta_1^2\right)\left(2\beta_2 - 3\beta_1^2 - 6\right) = 0$;
- Type VI denotes the four-parameter beta distributions;
- Type VII includes Student's t-distribution.